Charles University in Prague
Faculty of Mathematics and Physics

DISSERTATION

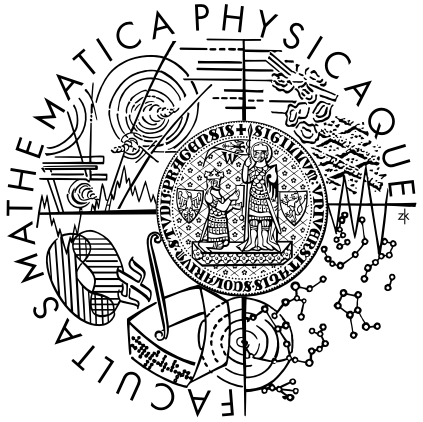

Tests of QCD Hard Factorization in Diffractive Photoproduction of Dijets at HERA

Karel Černý

Institute of Particle and Nuclear Physics

Supervisor: RNDr. Alice Valkárová, DrSc.
Study programme: Subnuclear Physics

Thereby I confirm that this thesis is authentic, it has been written using the sources of information listed in the bibliography. I agree this thesis to be rendered available for the public.

Prohlašuji, že jsem dizertační práci napsal samostatně a výhradně s použitím citovaných pramenů. Souhlasím se zapůjčováním práce.

V Praze dne Karel Černý

Abstract

Two measurements are presented of differential dijet cross sections in diffractive photoproduction ($Q^2 < 0.01$ GeV^2) based on HERA data acquired in the 1999 and 2000 running period with integrated luminosity of 54 pb^{-1}. The event topology is given by $ep \to eXY$, where the system X, containing at least two jets, is separated from a leading low-mass proton dissociative system Y by a large rapidity gap. The measurements are made in two kinematic ranges differing primarily in the transverse energy requirements on the two hardest jets. The dijet cross sections are compared with next-to-leading order QCD predictions based on recent diffractive parton densities obtained by H1. The next-to-leading order calculations predict larger cross sections than the data. The suppression of the data relative to the calculation is found to have no significant dependence on the photon four-momentum fraction entering the hard subprocess. There is a suggestion of a dependence of the suppression factor on the transverse energy of the jets.

Acknowledgments

I would like to express my sincerest gratitude to my supervisor Alice Valkarová. I have benefited from her guidance, great insight a and an excellent choice of the subject of the thesis and I wish to say a heartfelt thank you to her.

I am deeply grateful to the Department of Particle and Nuclear Physics of the Faculty of Mathematics and Physics of the Charles University in Prague. I have been taking a generous support provided by the budget of the department and also by scientific projects of Ministry of Education, Youth and Sports of the Czech Republic (MŠMT) through the following grants; LC527 and 1P05LA259. I have been given a possibility to travel to the DESY laboratory in Hamburg, Germany.

I would also like to express my gratitude to the members of the Prague groups of the H1 experiment for having been given the opportunity to participate in the experiment and to became a regular member of the H1 Collaboration. My cordial thanks and appreciation apply to the members of the H1 Collaboration. I have always been encountering both friendly and inspiring atmosphere there together with a real interest in my work and a willingness to help me with the physical analysis along the way. I am grateful to the HERA machine group whose outstanding efforts have made the experiment possible.

I must not forget to thank to the following people I met during the last few years in H1. In alphabetical order I have in mind Juraj Bracinik, Armen Bunatyan, Laurent Favart, Samvel Ghazaryan, Tomáš Hreus, Xavier Janssen, Hannes Jung, Misha Kapichine, Paul Laycock, Sergey Levonian, Pierre Van Mechelen, Matthias U. Mozer, Pal'o Murín, Paul R. Newman, Mirek Nozička, Ondřej Pejchal, Richard Polifka, Robert Roosen, Emmanuel Sauvan, Sebastian Schätzel, Kamil Sedlák, Tomáš Sýkora, David Šálek, Filip Tomasz, Roger Wolf, E.A. De Wolf and Josef Žáček. I appreciate a lot having the possibility working with them, I immensely value their help and opinions and no less pleasant was the time I have spent in their company.

I am grateful to Prof. Michael Klasen. I appreciate a lot his efforts concerning the NLO QCD calculations which allowed an independent verification of the results.

I would like to thank to my mother Olga. For the support and love she has been always selflessly giving me despite of difficult times she used to experience.

Dedicated to
my wife
Petra.

Contents

Chapter 1

Introduction

In this thesis two measurements are presented of differential dijet cross sections in the photoproduction regime of ep scattering. In photoproduction two basic leading order classes of photon interactions exist - direct and resolved. In the direct processes the photon interacts as a point-like particle. In the resolved processes the photon can develop its structure and acts as a composite particle. In diffractive ep scattering the proton stays intact or dissociates into a low-mass ($M_Y \ll E_{cm}$) state. The hard diffractive processes can be considered as being mediated by exchange of an object with the vacuum quantum numbers - the pomeron. A large gap in the rapidity distribution of the final state hadrons is observed. Owing to the photon structure there is an apparent resemblance between the resolved photoproduction and the hadron-hadron scattering. The factorization of the QCD calculable subprocess from the diffractive parton distribution functions in proton is not expected to hold in the hadron-hadron collisions [1]. The additional photon remnant and proton interactions are believed to fill the large rapidity gap and, therefore, to spoil the experimental signature of the diffractive event. Such a mechanism is expected to explain the difference between the measured structure function extracted from dijet production rates in $p\bar{p}$ collisions at Tevatron and the theoretical predictions based on the diffractive parton densities by H1 [2].

The measurements are based on luminosity of 54 pb^{-1} which is about a factor of three larger than in the previous H1 measurement [3] in a similar kinematic domain.

Chapter 2

Theory

2.1 Parton Model

In the late 1960's the experimental results from *ep* scattering data carried out at SLAC gave rise to an idea of proton as a composite particle, which was explained by existence of so called partons [4]. The partons were considered to be free non-interacting entities confined inside hadrons and they were identified with quarks - at that time already explaining various baryon and meson properties and establishing some hierarchy in the world of hadrons by means of use of a $SU(3)$ flavor symmetry group integrated in the additive quark model [5]. It was found rather soon that the quarks themselves cannot account on the full structure of the proton, that there are other carriers of the proton momenta - later on identified with gluons. There were still some missing pieces in the puzzle of partonic structure of the proton. Especially the non-observation of free partons - the confinement of partons inside hadrons. Moreover indications were available, based on experiments, that the number of partons is actually infinite. This observation, from the point of view of additive quark model an unwelcome one, was explained by a famous emergence of quantum field theory of strong interactions, Quantum Chromodynamics.

2.2 Quantum Chromodynamics

The problem of confinement led theorists to work towards a concept with peculiar properties, to a theory which allows an explanation of rise of the interaction strength at large distances. This was achieved by formulation of the Quantum Chromodynamics (QCD). QCD is a non-abelian gauge SU(3) group invariant theory dealing with six quark-fermion fields carrying a so called color quantum number and with a multiplet of eight gauge fields, identified with gluons. Due to the fact that gluons carry the color charge too, the coupling of the gluons among themselves is possible - which makes the QCD different from the case of Quantum Electrodynamics (QED). The coupling constant α_s is a characteristic

strength of the interaction in QCD. Quantum Chromodynamics is an asymptotic-free theory which means that the coupling strength α_s vanishes at zero distance. A perturbative approach to the QCD will inevitably lead to divergent terms. Therefore regularization methods are employed to get rid of the divergencies. In turn a so called regularization scale μ_r is introduced by virtue of which the calculations depend on μ_r. This dependence is absorbed in a redefined coupling constant $\alpha_s(\mu_r)$, masses and fields. As the physical results must not depend on the choice of μ_r, the $\alpha_s(\mu_r)$ must obey a so called renormalization group equation which is difficult to be solved analytically, but it can be expanded, for example up to order of $\mathcal{O}(\alpha_s^2)$ (for more details see [6]);

$$\alpha_s(\mu_r) = \frac{4\pi}{\beta_0 ln(\mu_r^2/\Lambda^2)} \left[1 - \frac{2\beta_1}{\beta_0^2} \cdot \frac{ln(ln(\mu_r^2/\Lambda^2))}{\mu_r^2/\Lambda^2}\right], \tag{2.1}$$

$$\beta_0 = 11 - \frac{2}{3}n_f, \tag{2.2}$$

$$\beta_1 = 51 - \frac{19}{3}n_f, \tag{2.3}$$

where Λ_0 is called a QCD scale which is to be determined from experiments and is introduced in order to make α_s dimensionless after the finite order expansion. The n_f is number of active quark flavours used. The experimentally measured α_s value is often presented at the mass of Z^0, $\alpha_s(\mu_r = m_{Z^0}) = 0.1187 \pm 0.002$, [6].

The perturbative expansion of α_s stops at a finite order and makes the α_s dependent on μ_r. The perturbative QCD calculations can converge only for low enough α_s, therefore, the renormalization scale μ_r must be high (or "hard") enough. A terminology came to stay that a hard scale must be present in the processes to allow the use of perturbative QCD.

2.3 Deep Inelastic Scattering

Deep inelastic scattering (DIS) is a class of neutral current (NC) or a charged current (CC) reactions of leptons with nucleons of type

$$l(k) + N(P) \rightarrow l'(k') + X(P_X), \tag{2.4}$$

where l can be $e^{\pm}, \mu^{\pm}$ and $\tau^{\pm}$, in general. X denotes a hadronic final state (HFS). In figure 2.1 a diagram is shown for a neutral current process with an electron scattering from a quark in the proton via a virtual photon exchange. Corresponding four-momenta can be deduced from the figure.

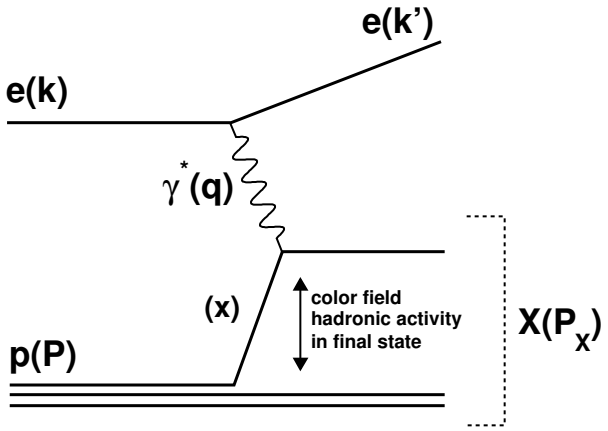

Figure 2.1: Feynman diagram of the deep inelastic scattering of electron from proton. The quark carrying a fraction x of the proton four-momentum is struck by a virtual photon γ^*. A final state, X, is created due to a strong force between the proton remnant and the struck quark.

2.3.1 The kinematics of DIS

The basic kinematics of the DIS can be described in terms of the following invariants

$$s \equiv (k+P)^2, \quad Q^2 \equiv -q^2 = (k-k')^2, \quad y \equiv \frac{q \cdot P}{k \cdot P}, \quad x \equiv \frac{Q^2}{2\, q \cdot P}, \tag{2.5}$$

where the four-vectors are defined according to figure 2.1. These variables are related through $Q^2 \approx s\, x\, y$ (neglecting the proton mass), where s is the square of the total CMS energy of the collision, Q^2 is the photon virtuality, y is the scattered electron inelasticity and x is the four-momentum fraction of the proton transfered to the interaction. Furthermore, the invariant mass of the photon-proton system is given by

$$W \equiv \sqrt{(q+P)^2} \approx \sqrt{ys - Q^2}. \tag{2.6}$$

Throughout this thesis only the case of ep scattering is considered. The deep inelastic regime of the ep scattering is defined by kinematics constrained to values

of Q^2 and $m_p\nu$ (where $\nu = k_0 - k_0'$ in the proton rest frame) which are much larger than m_p^2 while keeping Bjørken x variable fixed and finite.

2.3.2 Cross section of DIS

The inclusive cross section of DIS depends on two variables only. Based on cogitations taking into account conservation laws and the fact that the virtual photon scatters from a free charged fermion via a QED coupling the cross section formula of the DIS takes the form of

$$\frac{d\sigma}{dxdy} = \frac{4\pi\alpha_{em}^2 s}{Q^4}\,\frac{1}{2}\,\left[1+(1-y^2)\right]\cdot F_2(x), \tag{2.7}$$

where in the derivation of the above formula two structure functions of the proton are employed $F_1(x)$ and $F_2(x)$ with a use of so called Callan-Gross relation, $F_2^{D(4)} = 2xF_1^{D(4)}$, for derivation see [11] or [13].

2.3.3 Structure functions in DIS

The cross section formula for scattering of electron from a single quark (carrying a charge e_q) via virtual photon exchange is given by

$$\frac{d\hat{\sigma}}{dy} = \frac{2\pi\alpha_{em}^2 e_q^2}{\hat{s}\,y^2}\left[1+(1-y)^2\right]. \tag{2.8}$$

Such a formula can be easily isolated from equation (2.7). This gives an opportunity to re-write the structure function F_2 in a factorized form of individual parton distribution functions (f_i, PDF) convoluted with functions which are calculable in QCD ($\hat{F}_2$), i.e.

$$F_2(x) = \sum_{i\ charged}\int_x^1 d\xi\ f_i(\xi)\ \hat{F}_2^i\left(\frac{x}{\xi}\right). \tag{2.9}$$

The equation (2.9) acquires more straightforward meaning if it is inserted to (2.7), i.e.

$$\frac{d\sigma}{dxdy} = \sum_{i\ charged}\int_x^1 d\xi\ f_i(\xi)\ \hat{\sigma}_i(\frac{x}{\xi}, y), \tag{2.10}$$

where $\hat{\sigma}_i(x/\xi, y)$ can be interpreted as a bare cross section of reaction of the electron with the quark via virtual photon exchange.

In a zero-th α_s order which is the model of non-interacting partons it can be written: $\hat{F}_2^q(z) = e_q^2(1-z)$. Using this relation in (2.9) the structure function can be expressed as: $F_2(x) = x\sum_q e_q^2\,[f_q(x) + f_{\bar{q}}(x)]$, where the sum runs over the quark flavors.

Actually, the relation (2.9) or better (2.10) means the end of the non-interacting parton model because it is known that within the perturbative QCD the quarks can emit gluons which can split to $q\bar{q}$ pairs and so forth. The bare $\hat{F}_2^i\left(\frac{x}{\xi}\right)$ take

form containing so called splitting functions and terms of $ln\ Q^2$. In figure 2.2(a) is shown the zero-th order α_s diagram for $\gamma^* q$ process. Possible real gluon emissions in t and s channel are shown in figures 2.2 (b) and (c), respectively. These diagrams are already of α_s order and they introduce divergent terms due to soft gluon emissions (infrared IR) or a collinear (to the quark) gluon emissions. Diagrams (b) and (c) are summed with virtual gluon emission diagrams shown in figures 2.2 (d), (e) and (f) because the very soft gluons in (b), (c) are experimentally imperceptible. After a correct summation of these real and virtual gluon emission diagrams (which contribute in a destructive way) the IR singularities vanish and only the collinear divergencies remain. The collinear divergencies are regularized by means of introducing a factorization scale μ_f. Finally, the renormalized parton distributions depend on the μ_f too, $f_i(\xi, \mu_f^2)$. In order to get rid of dependence of the physics on this scale the quark distributions must obey an equation

$$\frac{\partial\ q(x,\mu_f^2)}{\partial\ ln\ \mu_f^2} = \frac{\alpha_s}{2\pi} \int_x^1 \frac{dy}{y}\ P\left(\frac{x}{y}\right)\ q(y,\mu_f^2). \tag{2.11}$$

This equation is known as the Altarelli-Parisi or DGLAP evolution equation [7] for the quark distribution function. The $P(x/y)$ are the splitting functions provided by QCD. The DGLAP evolution equation can be formulated for the gluon distribution as well. By means of use of the evolution equations the parton distribution functions acquire a dependence on the factorization scale, in the inclusive DIS identified with Q^2. The dependence of the parton distribution functions on Q^2 can be naively explained as follows; one reaches a better spatial resolution as Q^2 increases due to the uncertainty principle, one is able to resolve more quarks and gluons which emerge from virtual emissions and splittings.

In figure 2.3 are shown the neutral current cross sections and fits of the parton distribution functions of the proton as a function of Q^2 for various values of x measured by the H1 and ZEUS collaborations using the full statistics of HERA I data from both experiments. A weak dependence on Q^2 can be observed in a wide range of x which is referred to as scaling of the DIS cross section. It reflects the fact that in a particular phase space region the quarks behave almost as non-interacting partons. This observation (SLAC) led to the formulation of the parton model. On the other hand the Q^2 dependence exists in the other parts of the phase space. On this dependence it is accounted very precisely by means of the DGLAP evolution equations.

Last but not least, it is worth to say that the idea of factorization of the parton distribution functions often called parton densities is successfully used. The proton PDFs (measured in the inclusive DIS) are well applicable in pp or $p\bar{p}$ physics too.

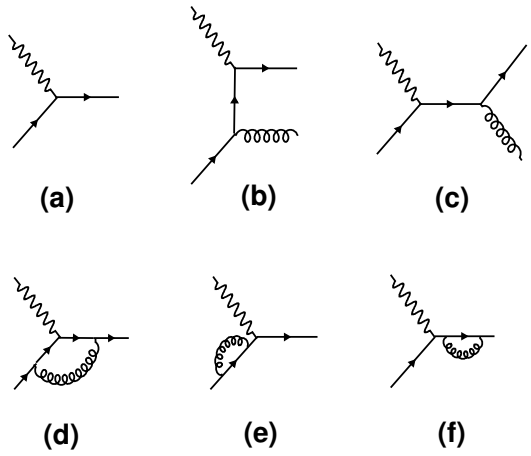

Figure 2.2: Processes contributing to the $\gamma^* q$ processes; (a) the bare photon-quark scattering; in (b) the t channel real gluon emission; in (c) the s channel real gluon emission. In figures $(d) - (f)$ are shown the virtual gluon emissions that cancel the infrared divergencies of the above real gluon emissions.

2.4 Space-time picture of DIS

Perturbative QCD calculations are made under an assumption that the quarks and gluons are as real as any other elementary particle. We already know, that the interaction strength grows between the color non-singlet objects at large distances. Luckily, the separation in time of the two stages into the hard sub-process and the long-distance process is possible, though not trivial. Unfortunately, the long-distance processes do not involve the hard scale and perturbative calculations are not possible, only approximative approaches are used to describe the transition of the partons into observable hadrons, generally referred to as hadronization.

The very first model of hadronization was a so called Independent Fragmentation Model [8] where fragmentation functions are introduced ($D_i^h(z, p_T)$) which describe the probability that a hadron h is produced with the transverse momentum of p_T with respect to the momentum of the original parton i carrying the fractional momentum of z. The fragmentation functions must be extracted from experiments.

There are also other approaches how to cope with the hadronization. Usually it is performed by means of models which are employed by the Monte Carlo generators (section 6.1.1). They provide both the generation of hard process and also the subsequent phase of hadronization.

Models of hadronization implemented in the Monte Carlo programs are widely used in these days. There is an important assumption that the dynamics of hadrons after the hadronization step is well correlated with the dynamics of hard scattered quarks and gluons. Yet it is assumed that the hadronization models

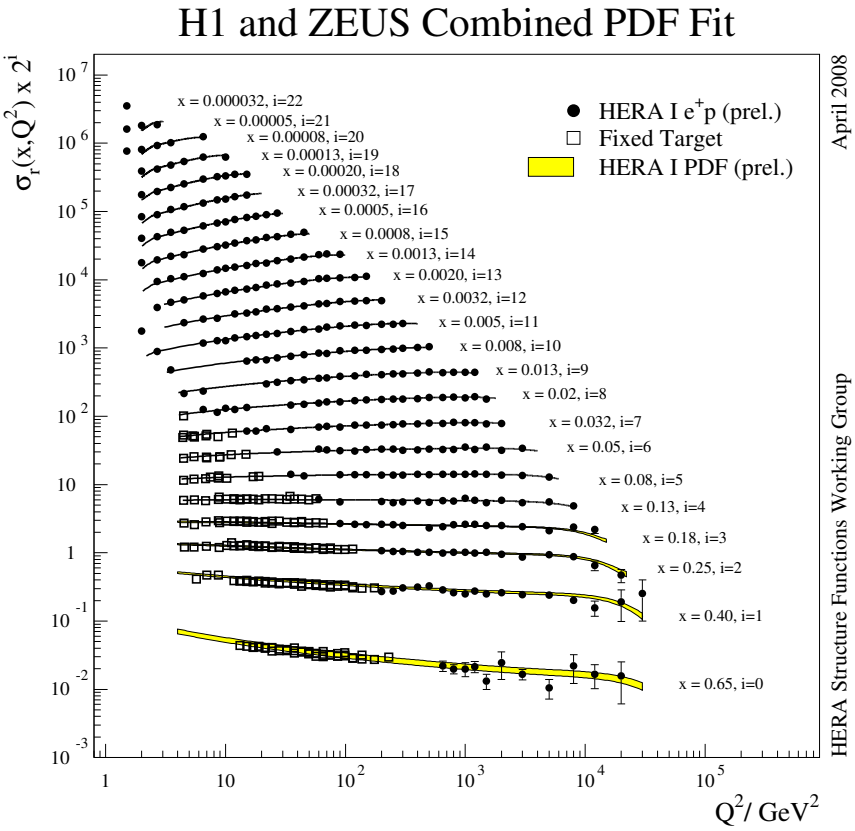

Figure 2.3: Neutral current cross sections and fits of parton distribution functions of the proton. Combined H1 and ZEUS HERA I data (dots). Fixed target data (open squares). Fit of the data (band).

are universal, which means that it is well justified to use them for e^+e^-, ep or $p\bar{p}$ physics.

2.5 Diffraction

A definition of what is called diffraction in the physics of particle collisions is not unique. The situation becomes even more difficult in a case of hard diffraction where QCD can be taken into account. In this thesis no attempt is made to get across all historical developments of the art.

One of possible depiction of diffractive processes is that they feature an exchange of vacuum quantum numbers; parity, charge, G-parity, strangeness and isospin $P = C = G = S = +1$ and $I = 0$, respectively. Another definition of diffractive processes, given by Bjørken, is such that the diffractive processes are reactions characterized by a large, non-exponentially suppressed, gap in the ra-

pidity distribution of the final state particles. The rapidity, y, is merely a useful variable used in the high energy physics since any rapidity difference is invariant under longitudinal Lorentz boosts. It is defined as

$$y = \frac{1}{2}\ ln\frac{E + p_z}{E - p_z}, \tag{2.12}$$

where E and p_z are the energy and longitudinal momentum of the particle, respectively. For massless particles or a highly relativistic case a so called pseudorapidity is derived as

$$\eta = -ln\ tan\ \frac{\theta}{2}, \tag{2.13}$$

with θ being the polar angle of the particle. Therefore, the second definition of diffraction says that the diffractive events are those which are equally probable for varying size of the gap in rapidity, i.e. $dN/d\Delta\eta \sim constant$. The non-diffractive events may create accidental rapidity gaps which are, unlike the diffractive processes, exponentially suppressed, i.e. $dN/d\Delta\eta \sim e^{-\Delta\eta}$.

Diffractive scattering of two particles may result in

- elastic scattering; $a + b \rightarrow a' + b'$,
- single dissociative diffractive scattering; $a + b \rightarrow X_a + b'$,
- double dissociative diffractive scattering; $a + b \rightarrow X_a + X_b$.

In figure 2.4 are sketched the three above situations of elastic, single dissociative and double dissociative diffractive events. In figure 2.5 a sketch of final state particles distribution in pseudorapidity is shown for the single dissociative event with a visualization of the rapidity gap $\Delta\eta$.

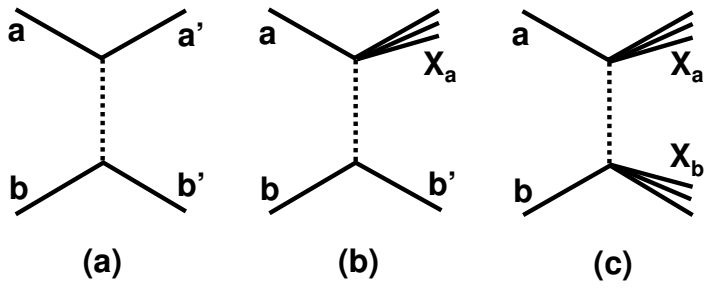

Figure 2.4: (a) elastic scattering. (b) single dissociation. (c) double dissociation. Vacuum quantum number exchange shown as a dashed line.

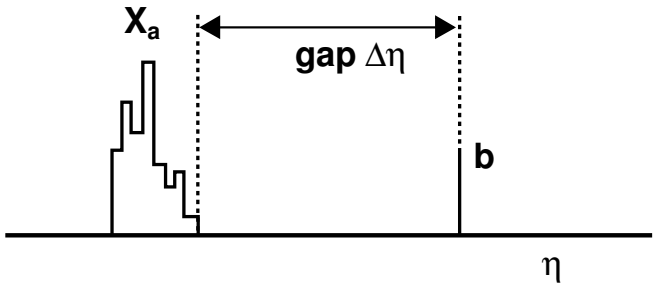

Figure 2.5: Sketch of a large gap in final state particles pseudorapidities for a single dissociative event.

The above paragraphs apply to the description of diffraction, in general. In this thesis diffractive events are studied with a hard scale presence and even with production of jets.

In the regime of soft diffraction, and in hadronic physics in past (before QCD), the Regge theory [9] was used. Trajectories (reggeons) in a complex angular momentum plane are used which enter the calculations of the scattering amplitudes. The reggeons are characterized by quantum numbers of existing mesons. Because of an experimental observation of a growth of the total hadron-hadron cross sections with energy (above $\sim 10-20$GeV) a pomeron ($I\!P$) trajectory with quantum number of vacuum is introduced which helps to describe the cross section energy dependence. No matter the pomeron is not a particle, a term of pomeron is often used in the hard diffractive processes where it can be realized by gluon and quark combinations carrying vacuum quantum numbers. The colorless nature of the pomeron exchange is responsible for creation of the rapidity gap. There is no color field connection between the final dissociative states. It was suggested that the diffractive processes with production of high p_T jets can serve as a probe of a perturbative pomeron structure (Ingelman and Schlein, 1985) [10]. Indeed, the hard diffraction was observed for the first time in $p\bar{p}$ by the UA8 experiment in CERN in 1988. Events with large rapidity gaps with hard scale were also observed by the CDF and D0 Collaborations at Tevatron. In 1993 and 1994 the ZEUS and the H1 experimental results, respectively, came into notice with observations of deep inelastic scattering processes with large rapidity gaps and high p_T jets in the final state. These observations were rather unexpected, at that time, and they resurrected the interest in this field of physics.

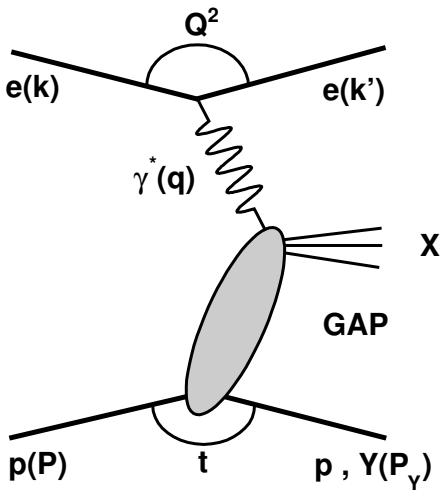

Figure 2.6: Feynman diagram of diffractive DIS process. Any type of colorless exchange is represented by the shaded blob which leads to an intact leading proton in the final state. Due to the colorless exchange the photon dissociative state (X) is separated from the leading proton by a large rapidity gap.

2.5.1 Diffractive Deep Inelastic Scattering

The processes of type $ep \to eXp$ with a high momentum transfer Q^2 (which can be identified with the hard scale) and where the photon dissociated system X is separated from a leading proton by a large rapidity gap is called a diffractive deep inelastic scattering (DDIS). In figure 2.6 a diagram is depicted for a DDIS event. The photon dissociative system is indicated by X. The proton in the final state is intact (p) or it can dissociate into a low-mass (compared to the total center of mass energy of the collision) system Y.

Using the variables defined in the previous sections the cross section of the DDIS can be written in terms of $\gamma^* p$ cross section in an analogy with a standard DIS (see [11]) as

$$\frac{d\sigma^D_{\gamma^* p}}{dx\, dQ^2\, dx_{I\!P}\, dt} = \frac{4\pi\alpha^2_{em}}{xQ^4}\left\{1 - y + \frac{y^2}{2\,[1 + R^{D(4)}(x, Q^2, x_{I\!P}, t)]}\right\} F_2^{D(4)}(x, Q^2, x_{I\!P}, t). \tag{2.14}$$

The above formula is obtained by means of introduction of two structure functions $F_1^{D(4)}$ and $F_2^{D(4)}$. Next are used longitudinal and transverse diffractive structure functions defined by $F_L^{D(4)} = F_2^{D(4)} - 2xF_1^{D(4)}$, $F_T^{D(4)} = 2xF_1^{D(4)}$ and the ratio $R^{D(4)} = F_L^{D(4)}/F_T^{D(4)}$. The Callan-Gross relation yields $F_2^{D(4)} = 2xF_1^{D(4)}$. The superscript D indicates that the processes are studied under a condition of

diffraction. The superscript (4) indicates that the cross section depends on four variables; x, Q^2, $x_{I\!P}$ and t which is the four momentum transfer squared at the proton vertex, i.e.

$$t \equiv (P - P_Y)^2. \tag{2.15}$$

The ratio $R^{D(4)}$ is usually neglected and an integration is performed over t as it is often difficult to be measured experimentally. The cross section formula reduces to

$$\frac{d\sigma^D_{\gamma^* p}}{dx\, dQ^2\, dx_{I\!P}} = \frac{4\pi\alpha^2_{em}}{xQ^4}\left(1 - y + \frac{y^2}{2}\right) F_2^{D(3)}(x, Q^2, x_{I\!P}), \tag{2.16}$$

which is analogous to the DIS cross section formula (2.7) with an addition of requirement of a diffractive origin of the processes.

2.5.2 Photoproduction of Dijets in Diffraction

In this section an introduction of kinematics is given which are specific to diffraction. Also a photoproduction regime of ep scattering is introduced.

A class of the ep scattering events with vanishing Q^2 (in this thesis $Q^2 < 0.01$ GeV^2) is called a photoproduction. Due to a small Q^2 the photon can fluctuate into relatively long-living $q\bar{q}$ pairs which are responsible for a fact that the photon does not interact as a point-like particle - resolved photon interaction, see for example [12]. Still, photon can couple directly via QED vertex to quarks - these processes are called direct photon interactions. In figure 2.7 (a) and (b) examples of a direct and resolved diffractive production of two hard partons in the final state, respectively. The hard scale in this case is not represented by the Q^2, rather, the transverse momenta of the two final state partons play this role. The hard partons can be considered to be a probe instrument of the virtual photon unlike the DIS case where the photon virtuality plays the role of the probe of the proton structure.

Using the notation from figure 2.7 further event variables specific to the diffractive ep scattering can be defined as

$$M_X \equiv P_X^2, \quad M_Y \equiv P_Y^2, \quad x_{I\!P} \equiv \frac{q \cdot (P - P_Y)}{q \cdot P}, \tag{2.17}$$

where M_X and M_Y are the invariant masses of the diffractive final state and the proton dissociative system, respectively. $x_{I\!P}$ is the longitudinal four-momentum fraction of the proton transferred to the system X.

With u and v being the four-momenta of photon and parton (parton and parton) in direct (resolved) processes entering the hard subprocess the invariant dijet mass can be expressed as

$$M_{12} \equiv \sqrt{(u + v)^2}. \tag{2.18}$$

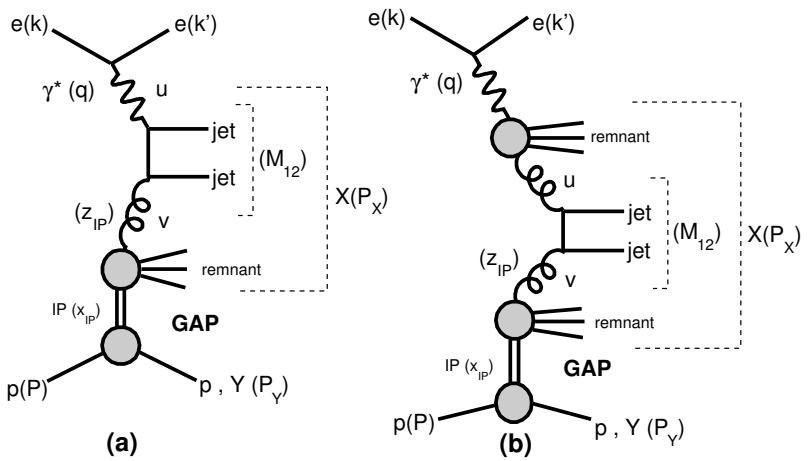

Figure 2.7: An example of leading order diagrams of diffractive dijet photoproduction at HERA. Diagrams (a) and (b) represent the direct and resolved photon interactions, respectively. The diffractive exchange is labeled with $I\!P$.

Finally, the four-momentum fractions of the photon and the diffractive exchange ($I\!P$) transferred to the hard interaction can be defined as

$$x_\gamma \equiv \frac{P \cdot u}{P \cdot q}, \quad z_{I\!P} \equiv \frac{q \cdot v}{q \cdot (P - P_Y)}. \tag{2.19}$$

2.5.3 Diffractive Parton Densities

Factorization of parton densities in DDIS

In diffractive DIS the factorization of diffractive parton densities can be written in analogy with the inclusive (non-diffractive) case. The QCD factorization formula for F_2^D takes a form

$$\frac{dF_2^{D(4)}(x, Q^2, x_{I\!P}, t)}{dx_{I\!P}\, dt} = \sum_i \int_x^{x_{I\!P}} d\xi \; \frac{df_i(\xi, \mu_f^2, x_{I\!P}, t)}{dx_{I\!P}\, dt} \; \hat{F}_2^i(\frac{x}{\xi}, Q^2, \mu_f^2). \tag{2.20}$$

The $df_i(\xi, \mu_f^2, x_{I\!P}, t)/dx_{I\!P}\, dt$ is the probability density of finding the parton i carrying a momentum fraction ξ in a proton under the constraints of diffractive kinematics. It is written an a differential form in $x_{I\!P}$ and t in order to stress that only this part accounts for the diffraction. The $\hat{F}_2^i(\frac{x}{\xi}, Q^2, \mu_f^2)$ are the same perturbatively calculable terms which appear in the DIS case. By means of using additional diagrams employed in the $\hat{F}_2^i$ calculation various QCD processes with hard scale can be plugged to the diffractive parton densities. This is, actually, what is called a hard QCD factorization in the diffractive deep inelastic scattering. The dependence on the factorization scale μ_f must cancel on the r.h.s.

if calculations are performed to all orders. That is why, the diffractive parton densities must obey the same (DGLAP) evolution equations like in DIS. If calculations are performed in a finite order the results depend on μ_f. Often, the factorization scale μ_f is set equal to the renormalization scale μ_r which was introduced in section 2.2. The validity of the assumption of QCD hard factorization was theoretically predicted in [16] and it will be elaborated on this issue a bit more in chapter 3.

There is yet another factorization which can be introduced, rather effective, inspired by Regge theory and supported by a bulk of experimental results from HERA - the proton vertex factorization often called a resolved pomeron model [10]. An assumption is made that proton emits the pomeron carrying a longitudinal fraction $x_{I\!P}$ of the original proton momentum. Thus, the diffractive structure function ($F_2^{D(3)}$, for instance), can be rewritten in a factorized form of

$$F_2^{D(3)}(x_{I\!P}, \beta, Q^2) = f_{I\!P/p} \ \cdot \ F_2^{I\!P}(\beta, Q^2), \tag{2.21}$$

where $\beta = x/x_{I\!P}$, $f_{I\!P/p}$ is a so called pomeron flux and $F_2^{I\!P}$ is the structure function of the pomeron which describes the parton densities in it. The $(t, x_{I\!P})$ dependence is disentangled from the (Q^2, β) one. In the zero-th α_s order the $F_2^{I\!P}$ is given by

$$F_2^{I\!P}(\beta, Q^2) = \sum_i e_i^2 \beta \ f_i^{I\!P}(\beta, Q^2). \tag{2.22}$$

The pomeron flux factor ($f_{I\!P/p}$) parameterization is motivated by Regge theory

$$f_{I\!P/p}(x_{I\!P}, t) = A_{I\!P} \ \cdot \ \frac{e^{B_{I\!P} t}}{x_{I\!P}^{2\alpha_{I\!P}(t)-1}} \ , \tag{2.23}$$

where the pomeron trajectory is assumed $\alpha_{I\!P} = \alpha_{I\!P}(0) + \alpha'_{I\!P}\, t$. The values of some of the parameters in (2.23) have been determined by H1 using proton tagging.

There is also a sub-leading, reggeon ($I\!R$), trajectory contributing mainly at high $x_{I\!P}$ values, therefore, it is added and the formula (2.21) is modified as follows

$$F_2^{D(3)}(x_{I\!P}, \beta, Q^2) = f_{I\!P/p} \ \cdot \ F_2^{I\!P}(\beta, Q^2) + n_{I\!R} \ \cdot \ f_{I\!R/p} \ \cdot \ F_2^{I\!R}(\beta, Q^2), \tag{2.24}$$

where the flux factor $f_{I\!R/p}$ is of the same form like in the case of pomeron, $n_{I\!R}$ is a normalization factor.

For more details on the values of the parameters in (2.23) and (2.24) see [14].

Recently measured diffractive parton densities by H1

In chapter 6 the diffractive parton densities are used as an input to the Monte Carlo simulations as well as to the next-to-leading order QCD calculations. Recently, diffractive parton densities were released by H1, namely in [14, 15].

In [14] the diffractive parton distribution functions are measured in the in-

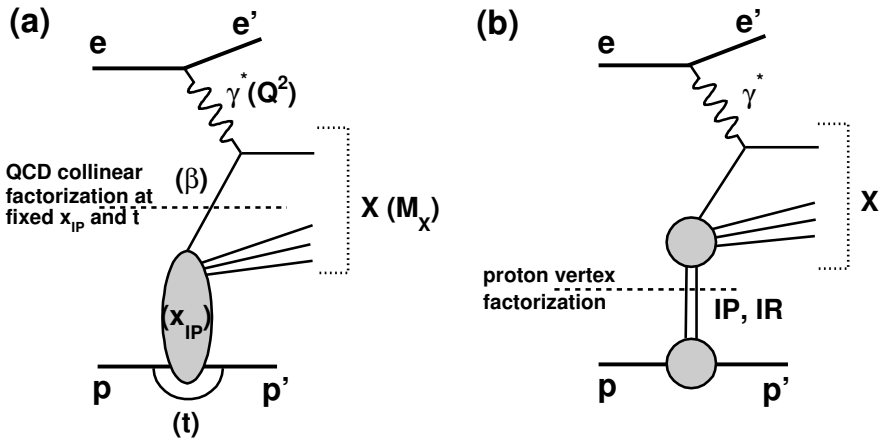

Figure 2.8: Neutral current DDIS process $ep \rightarrow eXp$. The dashed lines in (a) and (b) show where the diagrams are divided under the assumptions of QCD collinear factorization and

clusive neutral current DDIS, i.e in processes of type $ep \rightarrow eXp$, with possible dissociation of the leading proton. The diffractive data are selected by means of a presence of the rapidity gap. In figure 2.8 two factorization schemes (QCD collinear or hard QCD factorization and the proton vertex factorization) used in derivation of the parton densities are sketched.

Two DPDF fits are obtained in [14]; H1 2006 Fit A and Fit B. The fits differ in the parameterization chosen for the gluon density at the starting scale Q_0^2 for the DGLAP QCD evolution. The evolution starts at a given Q_0^2 with an initial form of the parton densities. They are evolved to a different Q^2 and fitted to the data at this Q^2 value. The functional form of the initial parton densities at the starting value, Q_0^2, is (see [14]);

$$z\, f_i(z, Q_0^2) = A_i\, z^{B_i}(1-z)^{C_i}, \tag{2.25}$$

where $i = q$ or g and z is the longitudinal momentum fraction of the parton entering the hard sub-process with respect to the diffractive exchange. The gluon density is parameterized with $B_g = 0$. The Fit B uses $C_g = 0$. Although the fit quality is similar for Fit A and Fit B the behavior of each is quite different at high values of z. In figure 2.9 are shown the fits of the diffractive distribution functions for a quark singlet combination and the gluon as a function of z for several Q^2 values.

The inclusive DDIS measurement in [14] shows that the gluon density dominates the diffractive exchange. The data used in [14] did not allow to determine the gluon density at high z values with sufficient precision. Nevertheless, there exists a process of hard process of boson-gluon fusion (BGF), see figure 2.7 (a), which is directly sensitive to the gluon density. The BGF process creates two

hard partons, consequently, two jets in the final state. In [15] the diffractive parton distributions are measured with the DDIS data with two jets in the final state. The resulting DPDF parameterization is called H1 2007 DPDF Fit Jets. In figure 2.10 is shown the fit of the diffractive distribution functions for a quark singlet combination and the gluon as a function of z for several two values of factorization scale.

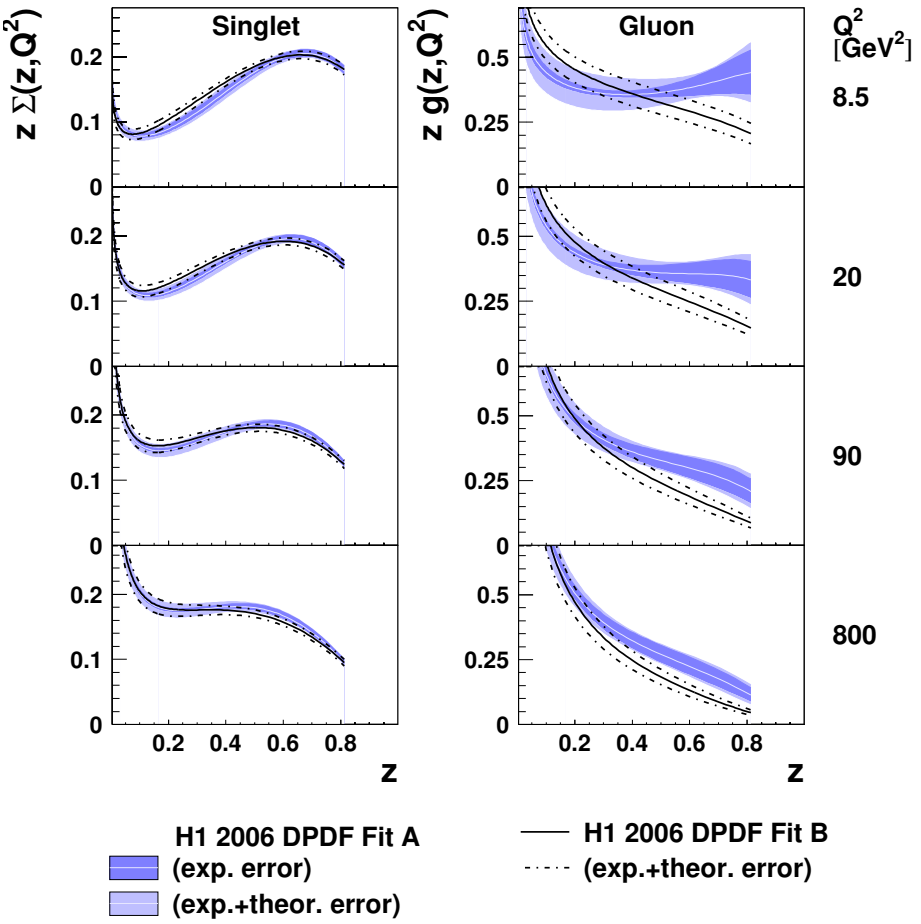

Figure 2.9: Comparison of the quark singlet and gluon diffractive densities for the two fits; H1 2006 Fit A and H1 2006 Fit B. Central values for Fit A are shown as a light colored line inside dark colored error bands. The Fit B shown as a dark full line together with total uncertainty band shown as a dot-dashed line.

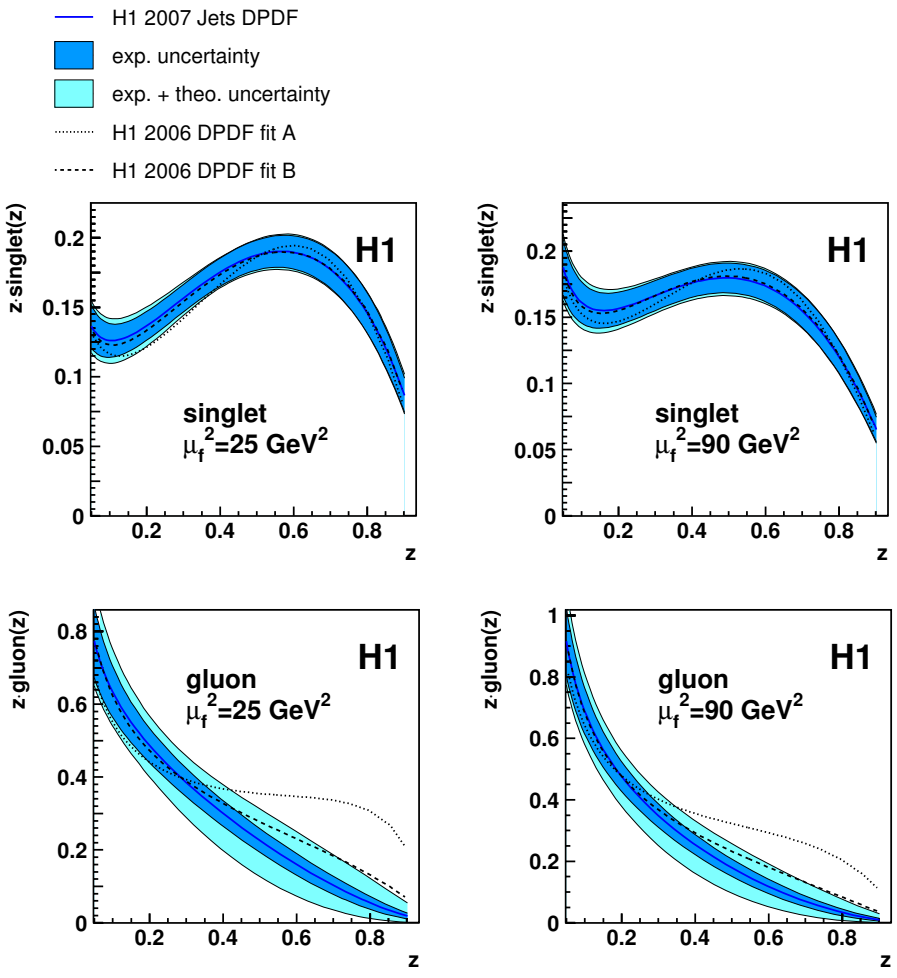

Figure 2.10: The quark singlet and gluon diffractive densities for the H1 2007 Fit Jets DPDF set. Central values for Fit Jets are shown as a full line with experimental and theoretical uncertainties indicated as coloured bands. Also H1 2006 Fit A and B are shown with dotted and dashed lines, respectively.

Chapter 3

Motivation and Recent Results

Various hard diffractive processes are calculable by means of using the diffractive parton distribution functions and the QCD factorization theorem, such as the diffractive jet production in DIS or photoproduction using Q^2 or p_T^{jets} as the hard scale, respectively, or a vector meson production with invariant mass of the meson playing the role of the hard scale.

The concept of QCD hard factorization of the diffractive PDFs has been predicted to hold in diffractive DIS processes [16]. In recent H1 analyses the validity of the hard factorization has been successfully tested for open charm production in photoproduction and DIS with D^* mesons [17] or the diffractive production of dijets in DIS [15]. However, a well known discrepancy exists between predictions based on H1 DPDF fits and a $p\bar{p}$ measurement of diffractive dijets at Tevatron published in [2]. Measurements of diffractive photoproduction of dijets are presented in [3, 18] where indications of factorization breaking are found.

3.1 Diffractive Open Charm Production in DIS and Photoproduction at HERA

In [17] the cross sections are measured of processes $ep \rightarrow eXY$ where the dissociative system X contains at least one charmed hadron and is well separated from the leading proton system Y (elastic or dissociated) by a large rapidity gap. The measurements are performed in DIS and photoproduction. The D^* mesons are explicitely reconstructed via the golden decay into a kaon and two pions of which one due to kinematical constraints is of very low momentum. In both kinematic regimes all differential distributions are well described by the NLO predictions. Both measurements, therefore, confirm that QCD factorization is applicable in DIS and photoproduction. It has to be pointed out, however, that the statistical significance of the photoproduction analysis does not exclude a factorization breaking which would be manifested in an overestimation of the cross section by the NLO QCD predictions. As an example, in figures 3.1 and 3.2 are compared

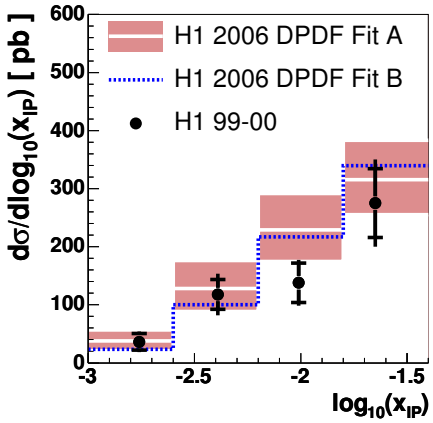

Figure 3.1: $d\sigma/dlog_{10}(x_{I\!P})$ for diffractive D^* production in DIS for data (dots) and NLO QCD calculations based on H1 2006 Fits A and B (histograms).

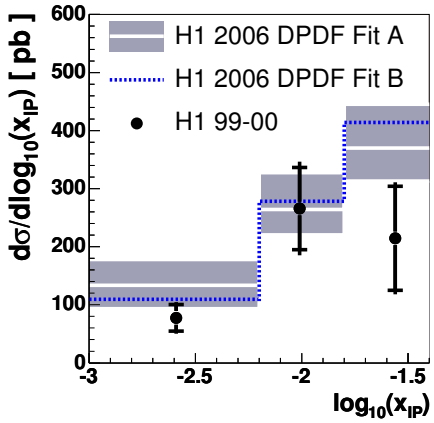

Figure 3.2: $d\sigma/dlog_{10}(x_{I\!P})$ for diffractive D^* photoproduction for data (dots) and NLO QCD calculations based on H1 2006 Fits A and B (histograms).

the measured differential cross sections (in $log_{10}(x_{I\!P})$) with the NLO QCD predictions based on H1 2006 Fit A and Fit B for the DIS and photoproduction analyses, respectively.

3.2 Dijets in Diffractive DIS

In [15] the differential cross sections of processes $ep \rightarrow eXY$ are measured where the photon dissociative system X contains two jets and is separated from the leading proton system Y (elastic or dissociated) by a large rapidity gap. The dijet data are compared with QCD predictions at next-to-leading order based on diffractive parton distribution functions previously extracted from measurements of inclusive diffractive deep-inelastic scattering, [14]. The prediction describes the dijet data well at low and intermediate $z_{I\!P}$ (the fraction of the momentum of the diffractive exchange carried by the parton entering the hard interaction) where the gluon density is well determined from the inclusive diffractive data, supporting QCD factorization. In figure 3.3 the measured differential (in $z_{I\!P}$) cross section is compared with the NLO QCD prediction based on the H1 2006 Fit A and Fit B DPDF. At a first glance, Fit B is able to reproduce the data better than Fit A.

3.3 Dijets in Diffraction at Tevatron

A well known disagreement exists between the diffractive structure function measured by the CDF collaboration with a use of dijet events if compared with

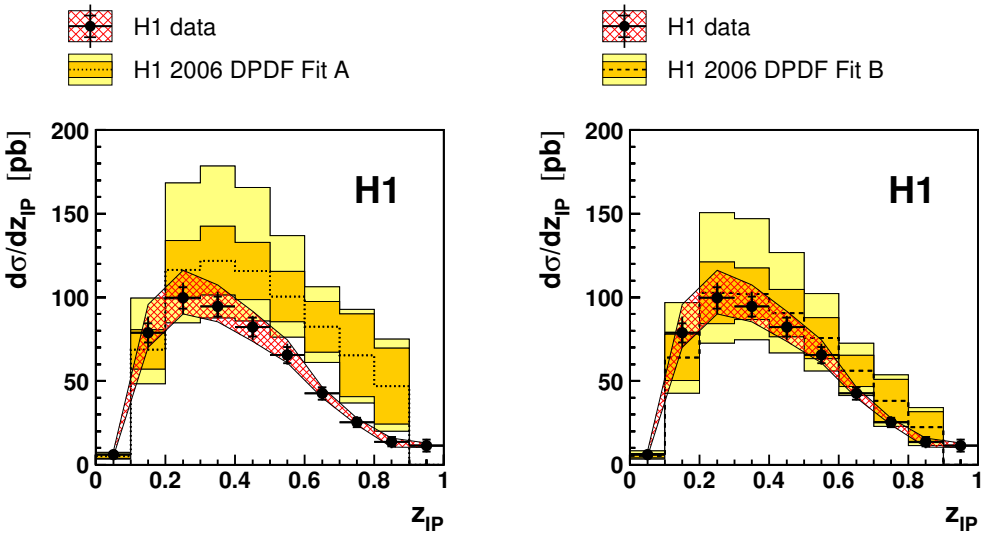

Figure 3.3: $d\sigma/dz_{I\!P}$ for diffractive dijet production in DIS for data (dots) compared with NLO QCD calculations based on H1 2006 DPDF Fit A (histogram in left hand side figure) and Fit B (histogram in right hand side figure).

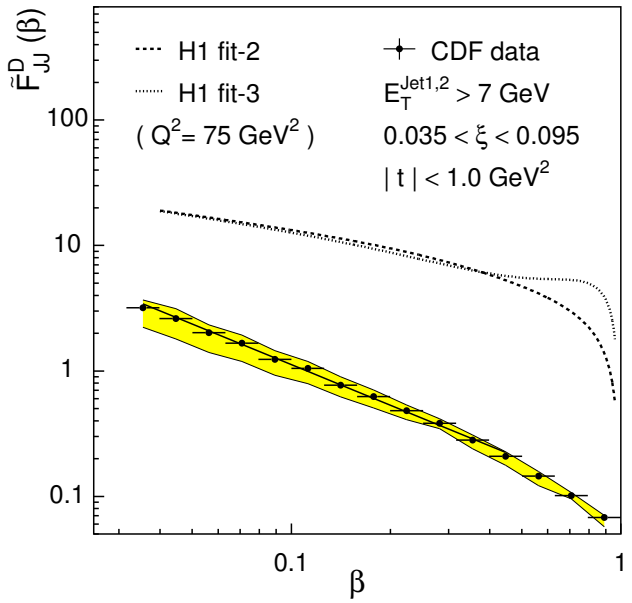

Figure 3.4: Diffractive parton densities of the proton measured by the CDF collaboration (dots) compared with expectations extracted from diffractive deep inelastic scattering by the H1 Collaboration (dashed lines).

predictions based on the diffractive PDFs provided by H1, [2]. In figure 3.4 is shown the measured diffractive proton structure function F_2^D differentially as a function of the parton four-momentum fraction with respect to the diffractive exchange, β. It is compared with expectations based on the DPDF fits obtained from the inclusive DDIS H1 measurement [19]. There are already comparisons available with newer H1 DPDF fits, nevertheless, the conclusions remain similar - the predictions overestimate the CDF data significantly.

Stimulated by this experimental observation theoretical explanations arose, namely, that the QCD hard factorization is not expected to hold in the hadron-hadron collisions [1]. The additional photon remnant and proton interactions are expected to fill the large rapidity gap and, therefore, to spoil the experimental signature of the diffractive event. In [1] a so called survival probability is introduced (S), normalized to unity in processes where no gap destruction occurs. The mechanism of the gap destruction is sketched in figure 3.5 where the possible multi-pomeron exchange diagrams are shown which overlap the Born diagrams for single and double pomeron exchange processes which introduce survival probabilities S_1 or S_2, respectively, where $S_1 \neq S_2$.

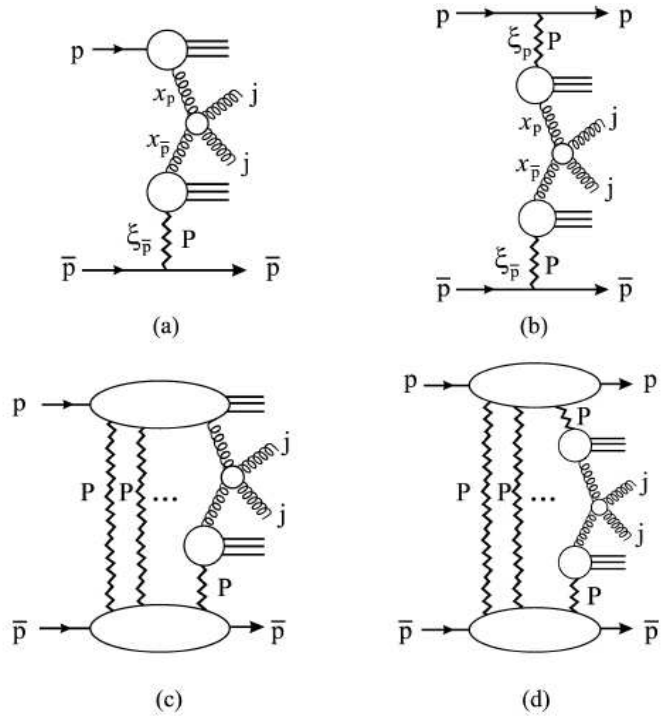

Figure 3.5: In (a, b) the Born diagrams are shown of diffractive dijet production in high energy $p\bar{p}$ collisions with one, two rapidity gaps indicated by pomeron exchange. In (c, d) the multi-pomeron exchange contributions are indicated to the above processes, where the upper and lower blobs encapsulate all possible pomeron permutations.

3.4 Dijets in Diffractive Photoproduction

Owing to the photon structure there is an apparent resemblance between the resolved photoproduction and the hadron-hadron scattering, see figure 2.7 (b). As the QCD hard factorization theorem is not expected to be valid in the hadron-hadron scattering, there is an expectation of a difference between the resolved and direct processes as to factorization validity if data are compared with the theoretical predictions based on the DPDF fits obtained from inclusive DDIS analyses.

Previous results concerning two jet production in diffractive photoproduction presented by the H1 and ZEUS collaborations can be found in [3] and [18], respectively. In [3] an overall suppression factor of 0.5 is applied to the theory prediction in order to reproduce the measured cross section. In [18] a similar analysis is presented with somewhat higher p_T range required on the jets. In [18] the global suppression factor of the theory predictions ranges from about 0.6 to 0.9, within the errors - depending on the DPDFs used.

In [3, 18] lack of dependence of the suppression factors is observed on the photon four-momentum fraction (x_γ) entering the hard subprocess which is in contrast to expectations of factorization breaking to be more important in the resolved (low x_γ) processes.

It was noticed (and presented at the ISMD07 conference, W. Schmidke) that there are indications of harder p_T^{jet1} differential cross section spectra in the data than in the theory prediction in [18]. The same indication is found in [3] which is visible in figure 3.6. There are shown the measured differential cross sections compared with NLO QCD predictions based on H1 2006 Fit B. A harder E_T^{jet1} slope in the data then in the NLO theory prediction can be seen. A global factor of 0.5 is applied to the NLO QCD predictions. Independence of the this suppression factor on x_γ range is discussed in [3] in greater detail.

In figure 3.7 the differential cross section $d\sigma/dx_\gamma$ measured in [18] is compared with the NLO QCD calculations based on several DPDF fits. It can be seen that the predicted cross sections vary with DPDF fits. The lack of dependence on the x_γ variable can be seen in the lower part of the figure where the ratio of the data to theory is plotted.

Another suggestion of a p_T dependence of the factorization breaking

There is yet another independent suggestion of a dependence of the factorization breaking on the p_T range of the jets. In figure 3.8 is shown a double ratio of the suppression factor of the data to the NLO predicted cross section $d\sigma/dp_T^{jet1}$ in photoproduction to DDIS. Since the hard factorization holds in DDIS the double ratio accounts on the suppression in photoproduction and it profits from cancellations of various systematic uncertainties as well as of uncertainties of the DPDF fits. In accordance with observations of different suppression factors and

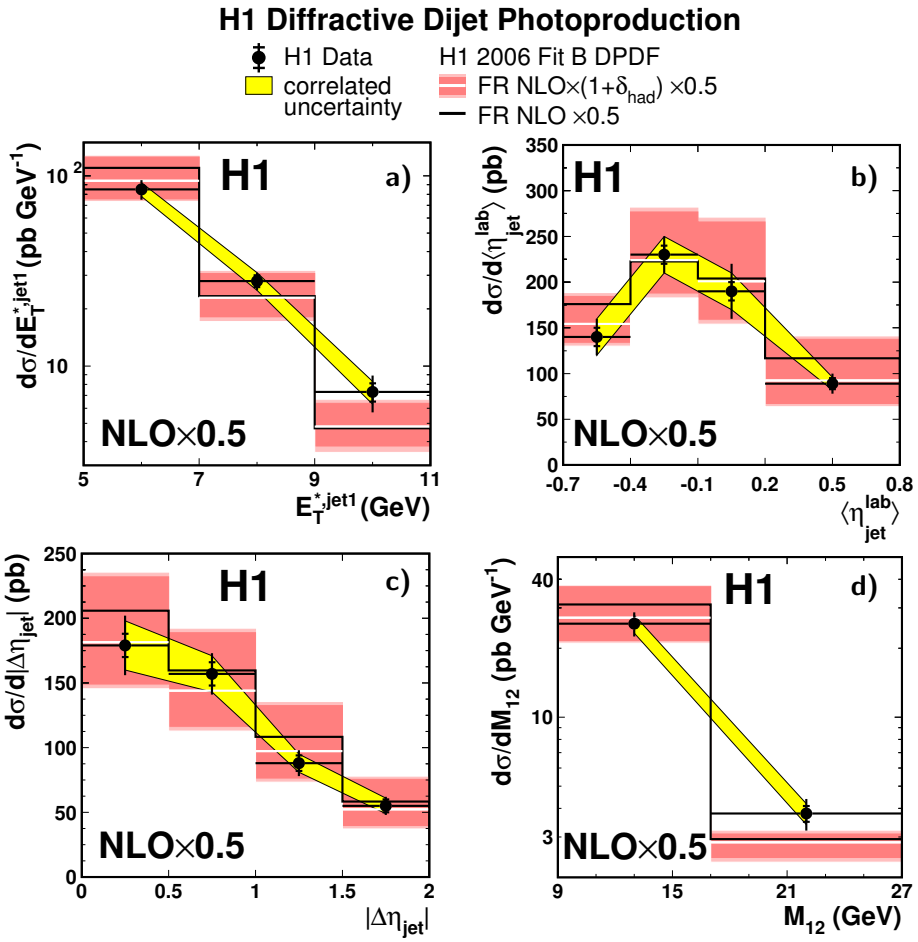

Figure 3.6: Differential cross sections for the diffractive production of two jets in photoproduction measured by H1. Compared are the data (dots), the NLO QCD calculations based on the H1 2006 Fit B corrected by means of use of hadronization corrections (white line histogram) together with renormalization scale uncertainty (red band) and the NLO H1 2006 Fit B predictions without hadronization corrections (black line histogram). The NLO values are always multiplied by a suppression factor of 0.5.

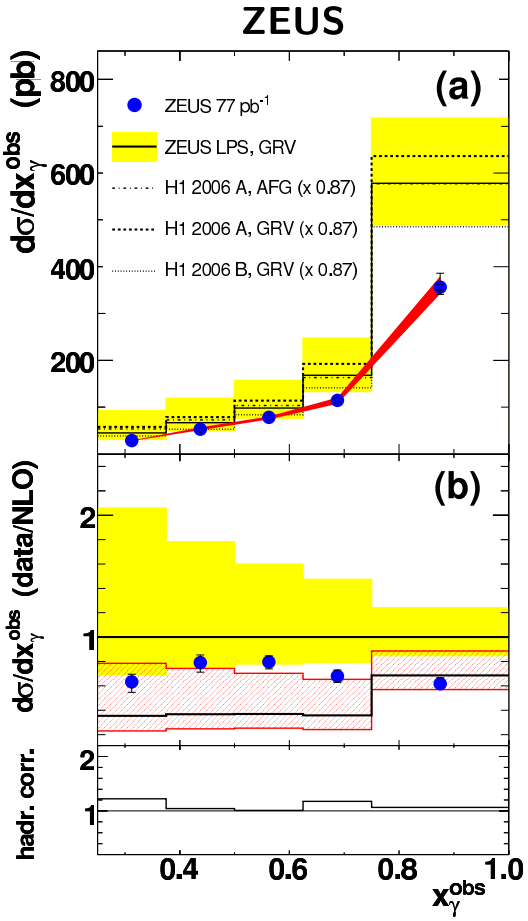

Figure 3.7: Differential cross section ($d\sigma/dx_\gamma$) for the diffractive production of two jets in photoproduction measured by ZEUS. In (a) are shown the data (dots) and the NLO QCD predictions based on several DPDF fits (see the legend), the hadronization corrections are applied to the NLO calculations (shown very below). In (b) a ratio of the data to NLO prediction based on ZEUS LPS DPDF is plotted (dots) together with uncertainties stemming from measurement and from theory. For more details see [18].

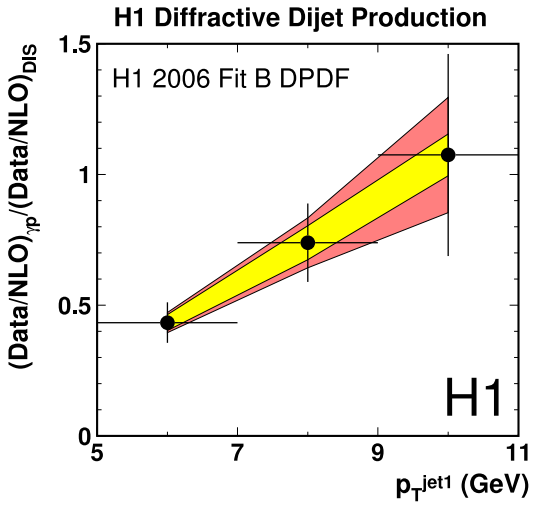

Figure 3.8: Double ratio of $d\sigma/dp_T^{jet1}$ for data to NLO QCD prediction based on H1 2006 Fit B in photoproduction to DDIS. The plot is based on published data from [3]. Thanks to Sebastian Schätzel.

harder p_T^{jet1} slopes in data than in the NLO predictions in [3, 18] the figure 3.8 suggests weaker suppression as p_T^{jet1} increases. The figure itself has not been published, it is, however, based on the published data from [3]. Given the large errors the statistical significance of the dependence in 3.8 is not high but it is interesting and supporting the idea of the p_T dependence of the factorization breaking. It would be, therefore, highly desirable to repeat similar analysis with newer HERA data.

3.5 Survival Probability at HERA, Tevatron and LHC

A suggestion of a factorization breaking can be seen already from comparison of rates of diffractive events at HERA and Tevatron. At HERA about 10% of events are diffractive whilst at Tevatron it is only about 1%. The mechanism of the factorization breaking was outlined in section [1] and in figure 3.5. It was explained by means of multiple $I\!P$ exchange. As it was shown in section 3.3 the survival probability for diffractive dijet production at Tevatron is about 10% if compared with predictions based on H1 DPDF fits.

At the LHC the protons and antiprotons will collide with center of mass energy of about 14 TeV. A substantial attention is given to central exclusive production (CEP) channels which are hoped to be discovery channel for the Higgs boson production in processes of type;

$$pp \rightarrow \ p + H + p \ , \tag{3.1}$$

where large rapidity gaps separate the central final state emerging from H and the leading protons.

The advantage of the CEP channels at LHC is that they provide a clean environment of the central detector. The diffractive CEP is expected to be burdened by rescattering again. The probability of survival of diffractive events at LHC for the diffractive CEP Higgs production has been calculated of $\hat{S}^2 = 0.026$, [20, 21]. Hence, understanding the dynamics of factorization breaking in the diffractive hadron-hadron scattering is of vital importance.

3.6 Phase Space of the Measurement

Under the circumstances, that different conclusions were drawn as to the factorization breaking in [3] and [18], the original H1 analysis [3] is repeated also in an additional scheme of kinematics in order to approach the analysis phase space from [18] as closely as possible. Both measurements are performed at $s = 101200$ GeV^2 which corresponds to center-of-mass energy of ~ 318 GeV. The first measurement is performed in the kinematic range of (3.2)-(3.9) while the latter one differs according to (3.10)-(3.13).

$$Q^2 < 0.01 \text{ GeV}^2, \quad (3.2)$$
$$0.3 < y < 0.65, \quad (3.3)$$
$$p_T^{jet1} > 5 \text{ GeV}, \quad (3.4)$$
$$p_T^{jet2} > 4 \text{ GeV}, \quad (3.5)$$
$$-1 < \eta^{jet1,jet2} < 2, \quad (3.6)$$
$$x_{I\!P} < 0.03, \quad (3.7)$$
$$|t| < 1 \text{ GeV}^2, \quad (3.8)$$
$$M_Y < 1.6 \text{ GeV}, \quad (3.9)$$

$$p_T^{jet1} > 7.5 \text{ GeV}, \quad (3.10)$$
$$p_T^{jet2} > 6.5 \text{ GeV}, \quad (3.11)$$
$$-1.5 < \eta^{jet1,jet2} < 1.5, \quad (3.12)$$
$$x_{I\!P} < 0.025, \quad (3.13)$$

where p_T^{jet1} and η^{jet1} are the transverse energy and pseudorapidity of the leading jet, respectively, both in the laboratory frame. The same notation applies to the sub-leading jet.

The second measurement,therefore, matches the kinematic range of [18] except that it has a more restrictive y and Q^2 ranges and different treatment of proton dissociation contribution than used in [18].

For the sake of simplicity a notation of "*low* p_T^{jets}" or "*high* p_T^{jets}" will be used to refer to the measurements in the phase space region of (3.2) - (3.9) or in a modified one according to (3.10) - (3.13), respectively.

Chapter 4

The H1 Experiment at HERA

The HERA (Hadron-Elektron Ring Anlage) is a particle accelerator located at the DESY (Deutsches Elektronen Synchrotron) laboratory in Hamburg, Germany. It started its first operation phase (HERA I) in 1992. In 2000 the accelerator underwent a major high luminosity upgrade (for HERA II phase) and kept delivering proton and electron (or positron) beams until June, 2007. The H1 experiment is one of four experiments situated at HERA whose physics programme, among others, spans the studies of proton structure; tests of QCD in jet, photon and heavy quark production; tests of electro-weak theory; studies of soft and hard diffraction; searches for new particles and phenomena.

4.1 The HERA Accelerator

The HERA accelerator (figure 4.1) consists of two accelerators located in a common tunnel. The tunnel is of 6.3 km length and it is roughly 20 m under the ground. Beams of accelerated protons and electrons are structured into so called bunches of particles which cross every 96 ns in interaction points. The analysis which is presented is based on the data acquired in the running period 1999 and 2000 with positron beam. Energies of the beams during that period were 27.5 GeV and 920 GeV for positrons and protons, respectively, which corresponds to center of mass energy of about 318 GeV.

4.2 The H1 Detector

A detailed description of the H1 detector can be found in [22]. Here, only a brief account on the detector components is given with emphasis on those relevant to the presented analysis.

The H1 detector layout can be seen in figure 4.2. Owing to the different energies of the beams the design of the H1 detector is asymmetric, biased in the proton beam direction in order to ensure a good acceptance for detection of

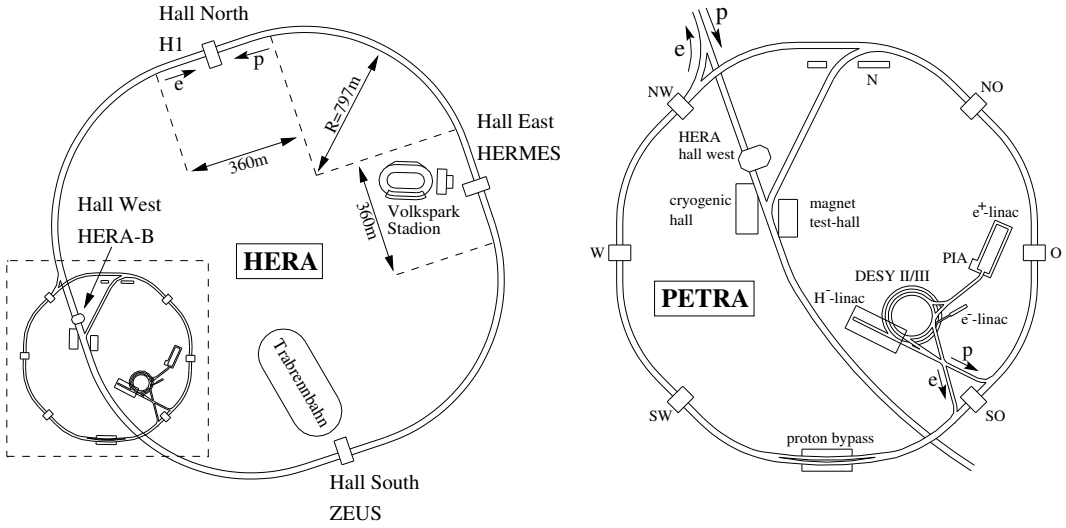

Figure 4.1: The HERA accelerator complex with its injection and pre-accelerator systems.

inelastic proton interactions. The structure of the H1 detector follows an usual shell-like pattern of the sub-detectors known from the collider experiments and will be described in following sections. Also an attention will be given to the detection systems used in analyses of the diffractive processes. The H1 reference frame originates in the designed *ep* interaction point with positive z-axis defined by the proton beam direction, the x-axis points to the center of the accelerator and the y-axis points upwards.

4.2.1 Tracking

For a schematic view of the H1 tracking system see figure 4.3. Measurements of charged particle tracks in H1 is provided by several individual trackers. There are two large concentric cylindrical drift chambers CJC1 and CJC2 with wires strung parallel to the beam axis which allows for an $r-\phi$ resolution of 170 μm and about 22 cm in the z-coordinate. CJC1 and CJC2 form a CJC tracking system with angular coverage of $15^\circ < \theta < 165^\circ$ yielding resolution of momentum measurement of $\sigma(p_T)/p_T = 0.5\% p_T/GeV \oplus 1.5\%$. There are two other (inner and outer) trackers dedicated to a precise z-coordinate measurement (CIZ and COZ) with wires strung perpendicular to the beam axis. Additionally, two layers of proportional chambers CIP and COP are integrated into the central tracker system used mainly for triggering purpose.

In the angular region of $152^\circ < \theta < 157^\circ$ the backward drift chamber (BDC) is installed improving measurement of the scattered electron angle.

Forward drift chambers are installed in the region of $7^\circ < \theta < 25^\circ$. Due to

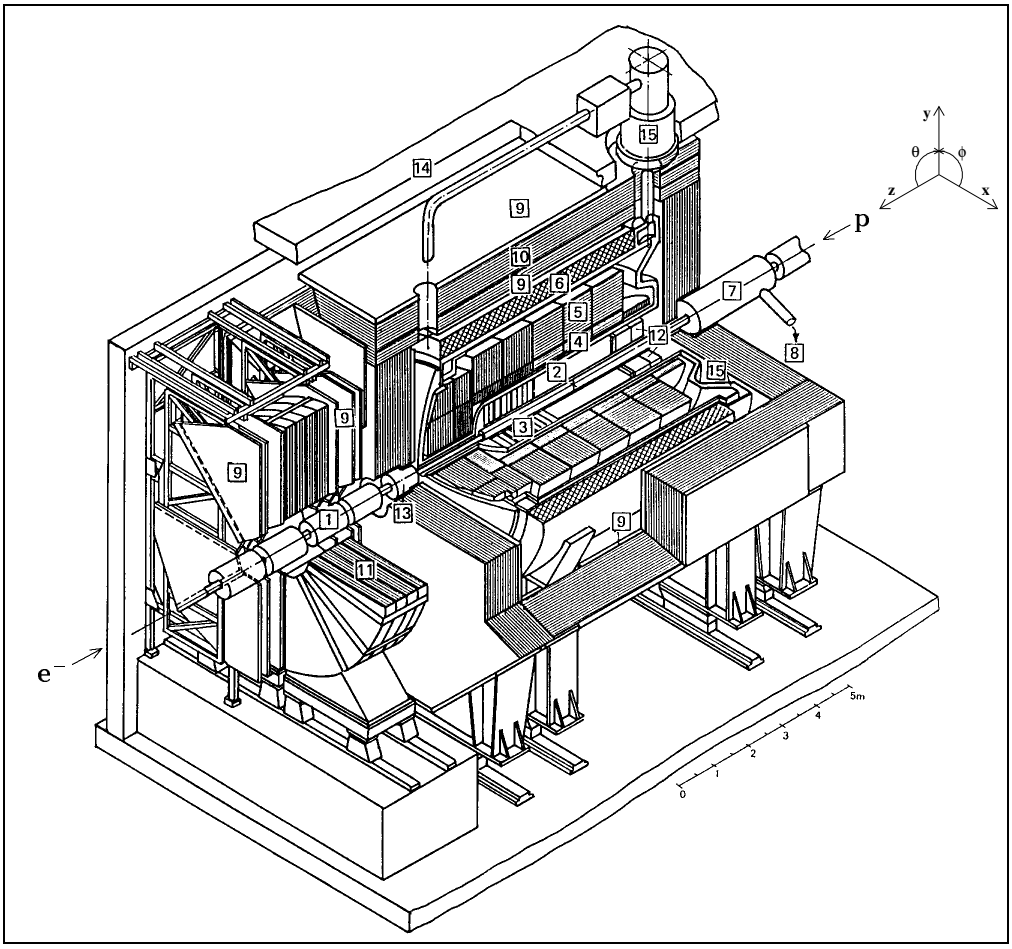

1	Beam pipe and beam magnets	9	Muon chambers
2	Central tracking device	10	Instrumented iron yoke
3	Forward tracking device	11	Forward muon toroid
4	Electromagnetic LAr calorimeter	12	Backw. electromagn. calorimeter (BEMC)
5	Hadronic LAr calorimeter	13	PLUG calorimeter
6	Superconducting coil (1.15 T)	14	Concrete shielding
7	Compensating magnet	15	Liquid argon cryostat
8	Helium supply for 7		

Figure 4.2: The H1 detector.

high multiplicities of secondary particles in the forward tracker [1] the information from it is not used in the current analysis.

Closest to the interaction point there are the central and backward silicon trackers (CST and BST). They are mainly designed for measurements of secondary vertices for identification of heavy quarks.

Last but not least, the whole tracking systems and also the main calorimeter (see section 4.2.2) are housed in a large superconducting coil which produces a magnetic field of about 1.16 T.

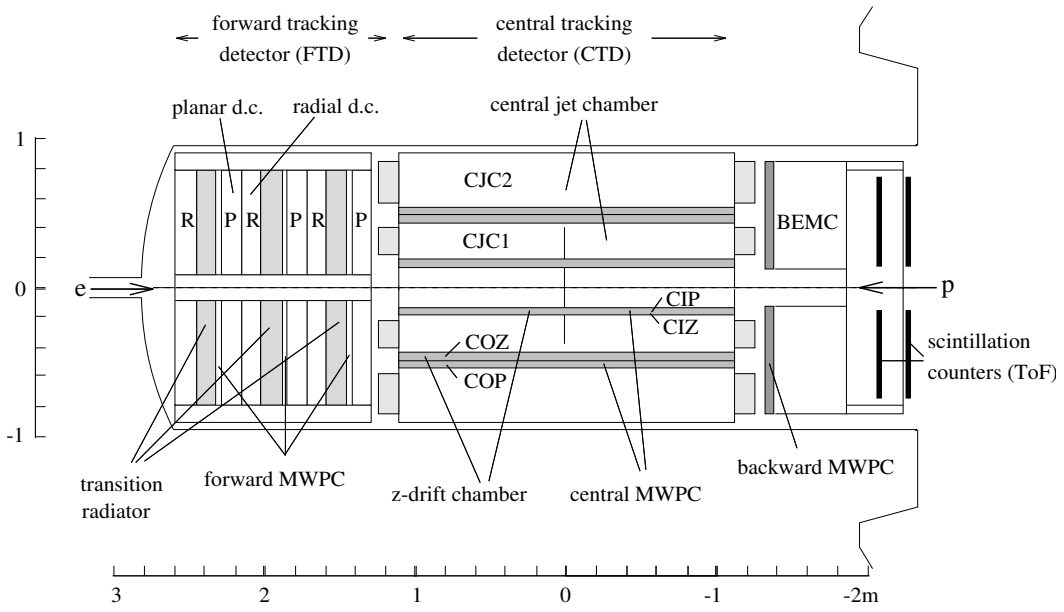

Figure 4.3: Lateral section through the H1 tracking systems.

4.2.2 Calorimetry

Liquid argon calorimeter (LAr)

In figure 4.4 a schematic view of the LAr calorimeter is shown. The LAr calorimeter is a main device for energy measurement in H1. It covers the angular range of $4° < \theta < 154°$. The calorimeter is designed to measure electromagnetic and hadron induced showers. Hence, there are two sections of the calorimeter sharing the liquid argon as an active material, the electromagnetic and the hadronic part differing in the absorber material. The electromagnetic part of LAr consists of lead absorber plates with total depth of 20 to 30 radiation lengths and it provides an energy resolution of $\sigma/E = 11\ \%/\sqrt{E} \oplus 1\%$. The hadronic part of the calorimeter consists of steel absorbers. Together with the electromagnetic part

[1] caused by large amount of dead material in front of the system

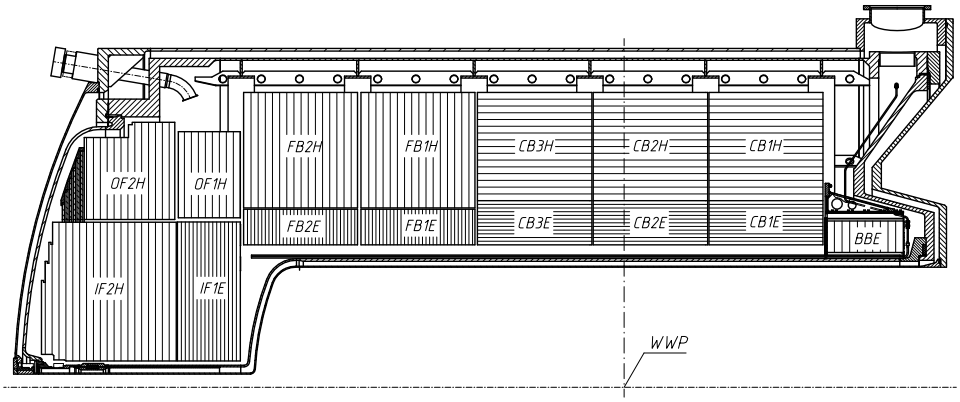

Figure 4.4: Upper half of the lateral section through the LAr calorimeter.

and depending on the polar angle the total depth ranges between 5 and 7 absorption lengths. The hadronic part energy resolution measured in tests beams is $\sigma/E = 50\ \%/\sqrt{E} \oplus 2\%$.

The H1 lead/scintillating-fibre calorimeter (SpaCal)

In the backward region the H1 detector is equipped with so called SpaCal calorimeter covering the angular range of $152° < \theta < 177°$. It is divided into an electromagnetic and a hadronic section. The electromagnetic section consists of scintillating fibres of $\sim$ 0.5 mm diameter embedded in a lead matrix providing measurements with resolution of $\sigma/E = 7.2\%/\sqrt{E} \oplus 1\%$. In the hadronic section fibres of $\sim$ 1 mm diameter are used and the resolution is achieved of $\sigma/E = 13.3.2\%/\sqrt{E} \oplus 3.6\%$ and $\sigma/E = 71\%/\sqrt{E} \oplus 20\%$ for electrons and non-leaking hadron showers, respectively. The SpaCal calorimeter gives a means to cover a wide range of Q^2 and to probe the parton structure of the proton down to very low values of x. Also it augments the acceptance for a hadronic final state produced in the backward region, for instance, the photon remnant. The schematic picture of SpaCal is shown in figure 4.5.

4.2.3 Forward Detectors

Since diffractive processes are studied in this thesis it would be desirable to measure the leading proton in the final state. There are some disadvantages of this approach, however. Mainly it is the low acceptance of the experimental techniques of proton tagging (see section 5.3). Therefore, often used is the large rapidity gap method where one demands the forward systems of the detection instrumentation to be devoid of any activity which is above noise. One can profit from much higher statistics of the diffractive sample obtained by means of the large rapidity gap method. One the other hand, one has to cope with a non-diffractive background

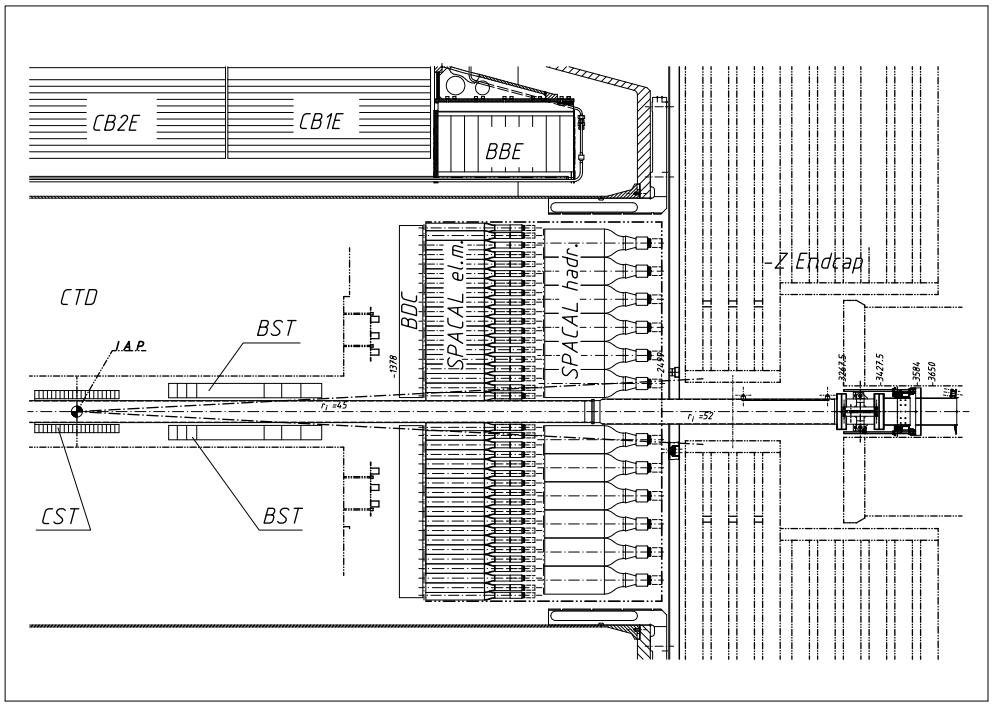

Figure 4.5: The SpaCal calorimeter in a lateral section view.

fraction and also with an inevitable contribution of leading proton dissociative events.

Forward muon detector (FMD)

In the highly active forward region the forward muon detector is installed. The angular coverage of FMD is $3° < \theta < 17°$. The main aim of FMD is a triggering and reconstruction of muons. Nonetheless, it can be also efficiently used for the large rapidity gap selection of the diffractive events especially for suppression of the leading proton dissociative states with higher masses (see figure 9.4 (a)). A schematic view of the FMD can be seen in figure 4.6. The FMD comprises of six double layers of drift chambers which allow θ and ϕ measurement. There are three layers placed in front of and behind the toroidal magnet. For the diffractive selection only the pre-toroidal layers are used.

Proton remnant tagger (PRT)

The contribution of leading proton dissociative events is desired to be suppressed as much as possible. Fragments of the dissociated leading proton with very high rapidities can be detected close to the beam-pipe. That is why the proton remnant tagger is installed at 24 m distance from the nominal interaction point. It consists of seven scintillator panels placed around the proton beam-pipe. Actually, in the

1999 and 2000 running period there were also other tagging stations installed. The whole system, including the PRT, is called forward tagging system (FTS). However, due to low tagging efficiency of the other stations only the one at 24 m (PRT) is used. In figure 4.7 the PRT design is shown schematically.

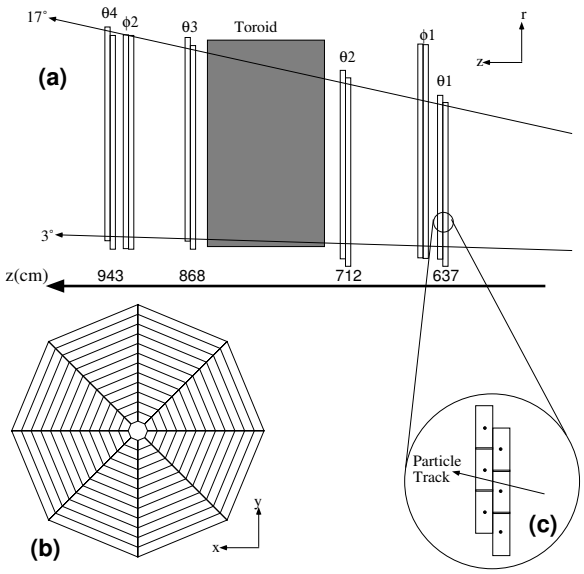

Figure 4.6: The forward muon detector. (a) An $r - z$ projection with pre and post toroid layers. (b) The front view of a theta layer. (c) Detailed view of drift cells that consist of two sub-layers.

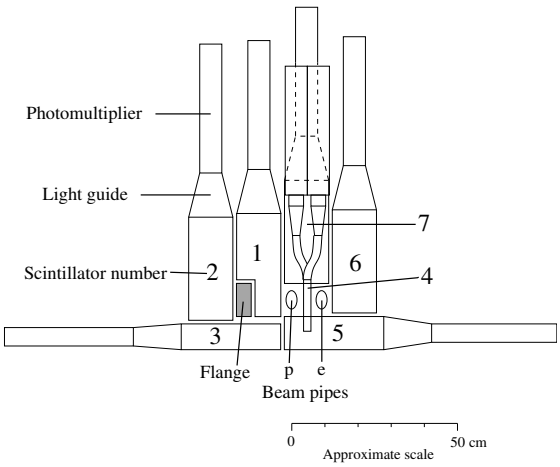

Figure 4.7: A schematic view of the proton remnant tagger. Shown are the scintillator plates and photomultiplier. Also the proton and electron beam-pipes are indicated.

4.2.4 Luminosity System

In order to measure the cross section it is essential to know what the luminosity of the data is. The luminosity over certain time period Δt of data taking is defined as follows

$$N(\Delta t) = \sigma \cdot L(\Delta t), \tag{4.1}$$

where $N(\Delta t)$ is the true number of events to occur during Δt and σ is the cross section of the processes responsible for the observed events. If one is given the cross section it is straightforward to measure the luminosity.

In the case of H1 the luminosity is measured by means of the Bethe-Heitler process ($ep \to e\gamma p$) which is very well known with a great precision calculated in quantum electrodynamics. There are two main components of the luminosity system at H1 (see figure 4.8) using crystal Čerenkov calorimeters with depth of about 22 radiation lengths; the photon detector (at -102.9 m) for measurement of the γ and the electron tagger (at -33.4 m) for measurement of the scattered electron, e. The measurement of the Bethe-Heitler processes is, however, not free of background. Especially, the scattering of the electrons from remaining atoms of the gas in the beam pipe contributes. Dedicated, so called pilot bunches, are present in the electron beam and serve for the estimation of the beam-gas interaction rate. This background is then statistically subtracted from the measured Bethe-Heitler sample.

The precision of the luminosity measurement is about 2.0% in the 1999 and 2000 running period.

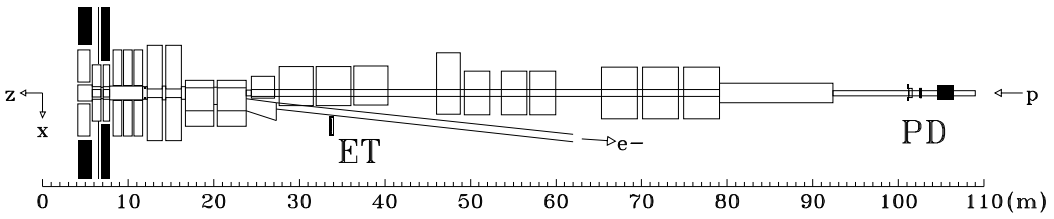

Figure 4.8: The H1 luminosity system; ET - electron tagger at -33.4 m; PD - photon detector at -102.9 m.

4.2.5 Trigger System

At HERA the bunch crossing interval is about 96 ns which corresponds to more than 10 MHz rate. However, not every bunch crossing produces a signal measurable by the H1 detector. Typical rate of physics processes ranges between $20 - 30$ Hz for tagged photoproduction and is much smaller for rare processes with large p_T with timescale of days or weeks. There is a substantial background

rate of $\sim$ 1 kHz which causes signal in the H1 detector and it is clear that not all channels can be read out at such rates. The read out causes a dead time and only a reasonable trigger decisions allow an efficient data taking. A four level trigger setup (L1-L4) is used in H1 with an ultimate rate of 40 Hz to be written to tapes. The main aim of the trigger system is to reject the background while keeping the interesting physics events.

Most of the sub-detectors provide a trigger information, so called trigger elements (TE). The complete set of TE information arrives into the central trigger logic within 22 bunch crossings (2.1 μs). Within other 2 bunch crossings the decision is made. In order not to cause the dead time the information is stored in a pipeline. If the event succeeds to pass the first level trigger (L1) it is retrieved from the pipeline. The L1 level is, therefore, dead time free because the events that fail to pass are thrown away and the position is freed in the pipeline. It is essential to reject as much of background as possible at the first trigger level.

The decisions at L1 are made by means of combinations of the TEs into so called sub-triggers. There are 128 sub-triggers combining usually the TEs designed to background rejection and some TEs for physics signals. If any of the sub-triggers accepts the events the "L1 keep" signal is set. Still, some sub-triggers can have rather high keep-rates and may prevail the other sub-trigger rates dedicated to less probable processes, though not less interesting. That is why so called prescale factors (prescales) need to be applied to some sub-triggers in order not to occupy the bandwidth. Prescale of 2 for a particular sub-trigger means that only half of the events will be set the "L1 keep" signal.

The true dead time starts if "L1 keep" signal is set. The second level trigger logic (L2) uses a topological trigger algorithm (L2TT) and a neural network (L2NN) together with more information from the detector and it also attempts to reconstruct path of particles. Another prescale factors can be introduced. If the event passes the L2 level the "L2 keep" signal is set. The decision is available within 20 μs from L2. If negative the data taking starts again. The third trigger level (L3) was not active during the data taking in the running periods of 1999 and 2000.

The full information about the event is submitted to the fourth trigger level (L4) in case of "L2 keep". Immediately after the detector is read out the data taking starts again. The L4 level processes the event independently with up to 30 events in parallel. It uses an approximate reconstruction algorithms for remaining background or cosmic event rejection. The L4 input rate must not exceed 50 Hz. The total dead time achieved up to the L4 level is during the normal data taking about 10%. After the L4 level the data are written to tapes. About one percent of events is stored no matter the L4 trigger decision in order to monitor the L4. To reduce the data volume, the events can be assigned additional prescales according to event type classes they are categorized by L4. The data are written to tapes with a final rate of $\sim$ 10 Hz.

Finally, a full offline reconstruction and event classification (called level five,

L5) is performed. The data are written to data summary tapes (DST) with typical size of 10 kByte per event.

Chapter 5

Detection of Diffraction at HERA

In this chapter an overview of main experimental methods of selection of the diffractive processes at HERA is given. The large rapidity gap method is briefly described. A so called M_X method used by the ZEUS collaboration at HERA is introduced. The method of direct leading proton tagging is described together with an introduction of Very Forward Proton Spectrometer in H1.

5.1 Large Rapidity Gap Method

Due to the colorless exchange in diffractive processes of $ep \to eXp$, the phase space between the dissociative system X is separated from the leading proton by a large rapidity gap. The selection of the diffractive events at HERA uses a fact that the forward instrumentation of the detectors (H1 or ZEUS) is devoid of activity above noise. Details about the large rapidity gap diffractive selection in H1 are also introduced in section 8.4.3.

The large rapidity gap method can be illustrated in figures 5.1, 5.2 where an event is shown in lateral and radial view of the H1 detector. There are two jets in the central detector. The proton leaks undetected downstream the beampipe. The electron is not visible since it scatters under very low angle and is detected in the e-tagger. There is a low activity in the forward region in this event, therefore, the large rapidity gap spans the space between the leading proton and the dissociative system containing the two jets.

In figure 5.3 is shown the distribution of η_{max} variable which is the pseudo-rapidity of a most forward calorimetric cluster with energy above a noise level. The figure is the first H1 observation [23] of a necessity of taking diffraction into account in the DIS at HERA. There is a lack of description provided by DIS Monte Carlo if compared with the real data. It can be nicely seen from the figure what was meant by Bjørken with exponentially unsuppressed probability of the size of the rapidity gap in diffractive processes. During years the requirement of presence of the large rapidity gap became a standard method for diffractive selection in H1. Note that the prescription of large rapidity gap selection does

not ensure an intact proton in the final state. Thus, a contribution of proton dissociation must be considered too. There are possibilities to suppress the proton dissociative events, see sections 4.2.3 and 8.4.3.

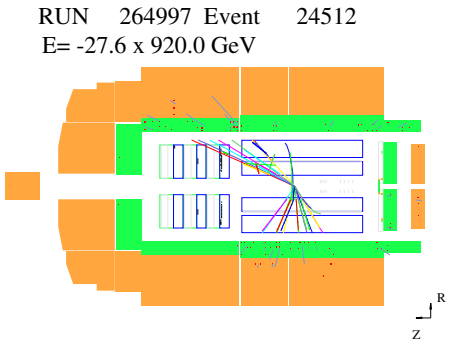

Figure 5.1: Lateral view of a large rapidity gap event in photoproduction in the H1 detector with two jets.

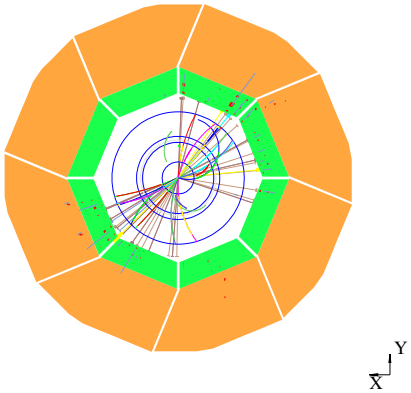

Figure 5.2: Radial view of a large rapidity gap event in photoproduction in the H1 detector with two jets.

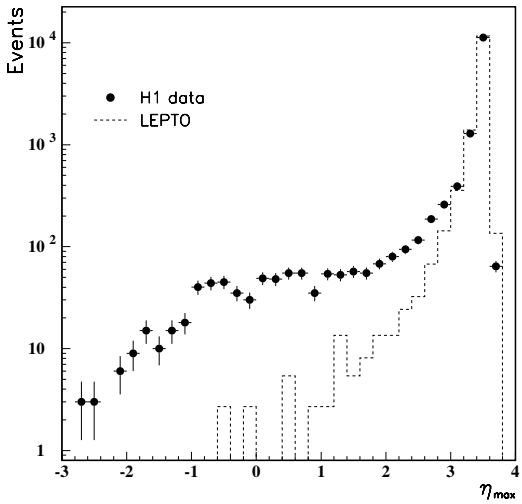

Figure 5.3: The η_{max} distribution in DIS for data (dots) and DIS Monte Carlo model Lepto (histogram). The data contain a diffractive contribution with exponentially unsuppressed probability of size of the gap which is missing in the MC sample.

5.2 M_X Method

Another method of diffractive selection has been developed and used by the ZEUS collaboration. It is called a M_X method. The diffractive and non-diffractive events are distributed differently in $ln\, M_X^2$, where M_X is the mass of the hadronic final state, X, produced in the detector no matter the event is diffractive or non-diffractive. The contribution of diffractive events is obtained statistically owing to the shape of $ln\, M_X^2$ distribution for the non-diffractive processes. The non-diffractive events create a peak in the $ln\, M_X^2$ distribution which falls off exponentially. Eventually, the shape of the full $ln\, M_X^2$ spectrum is parameterized as

$$\frac{dN}{d\, ln\, M_X^2} = D + c\ exp(b\, ln\, M_X^2), \tag{5.1}$$

where D represents the constant diffractive component.

As an illustration detector level distributions of $ln\, M_X^2$ are shown in figure 5.4 for Monte Carlo simulations only. Shown are contributions of the non-diffractive MC (Django) together with a fit of the exponentially suppresses shape and a diffractive MC (Satrap). The sum of both MC samples is fitted by formula (5.1). The figure shows the distributions for several bins of Q^2 and W.

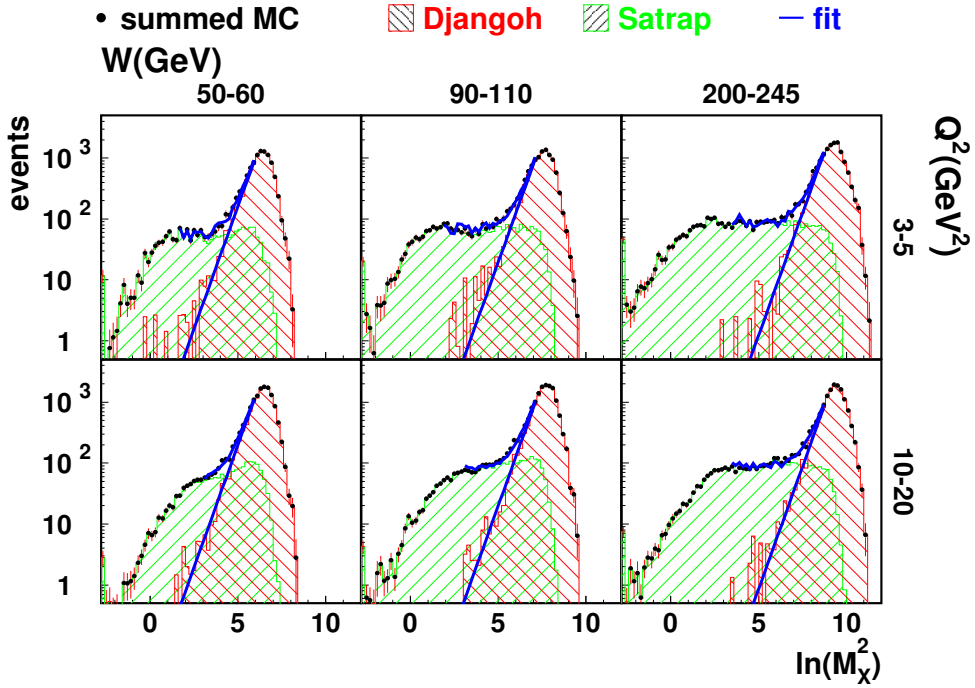

Figure 5.4: The $ln\, M_X^2$ distributions in bins of Q^2 and W for non-diffractive MC (Django) together with an exponential fit (linear in logarithmic scale). Diffractive contribution given by Satrap MC. The sum of both (represented by dots) is fitted with formula $dN/d\, ln\, M_X^2 = D + c\ exp(b\, ln\, M_X^2)$.

5.3 Proton Tagging

The idea of a direct tagging of the leading proton suggests itself naturally. The leading protons deviate from the nominal beam and are subjected to the influence of accelerator optics. It is possible to measure the leading proton by means of a dedicated technique of so called Roman Pots (RP) which allow to insert detectors into the beampipe while preserving vacuum in it. The diffractive kinematics of the proton can be reconstructed from the RP measurements. The inconvenience is that the detectors, embedded in the Roman Pots, cannot approach arbitrarily close to the nominal beam, thus, the acceptance is limited. On the other hand the advantage is that the measurements are free of proton dissociation. In H1 there are two systems dedicated for proton tagging. The first one is called a Forward Proton Spectrometer (FPS) [24]. The second one is called a Very Forward Proton Spectrometer (VFPS) [25].

In following sections a brief description is given of VFPS design and function. Studies of simulation of the VFPS were made in [26] as well as an attempt to perform physics reconstruction from the VFPS simulated measurements. The proton tagging in the VFPS was originally intended to be the method for the diffractive selection in this thesis. Due to some delays caused by hardware problems it was decided to use the large rapidity gap method instead of the proton tagging.

5.3.1 Very Forward Proton Spectrometer in H1

The Very Forward Proton Spectrometer (VFPS) [25] was installed in the H1 experiment during the 2003 shutdown of HERA. Its aim is to trigger on and measure the momentum of diffractively scattered protons originating from the H1 interaction point (IP). Because of the typically low energy losses ($x_{I\!P} \sim 0.01$) and scattering angles ($-1\text{GeV}^2 \lesssim t$), the VFPS detectors were placed at 220 m distance from the main H1 detector so that the strong spectrometer effect of the horizontal HERA dipole magnets can be used to separate diffractively scattered protons from the nominal proton beam.

The hardware setup of the VFPS is very similar to the Forward Proton Spectrometer (FPS) which was previously installed between 60 and 90 m downstream from the H1 detector. The VFPS consist of two Roman Pot stations, approximately 4 m apart and equipped with scintillating fibre detectors which approach the HERA proton beam horizontally from inside the HERA ring. The transverse coordinates of proton hits measured in both detector stations are combined into transverse coordinates and slopes with respect to the nominal proton beam at a location halfway the detector stations.

While the reconstruction code for hit finding, local track (in one station) and global track (combining two stations) reconstruction is common with the FPS, one needs to use a different approach for the determination the proton momentum from the transverse coordinates and slopes. This is partly due to strong non-

linear effects present in the HERA beam optics between the H1 interaction point and the VFPS. More importantly, however, a strong imbalance exists between the horizontal and vertical energy dispersion of the proton beam: while a strong dispersion exists in the horizontal coordinate, the vertical coordinate changes very little within the range of energy deviations relevant for the VFPS. The approach used for the FPS, exploiting both coordinate planes for the reconstruction of $x_{I\!P}$ is therefore less adequate in the case of the VFPS.

VFPS beam optics

The subject of the following sections is the reconstruction of the proton momentum based on the measurement of impact coordinates and slopes in the VFPS. The relation between both is given by the HERA beam optics and can be described in a general way by a matrix equation:

$$\mathbf{X} = \mathbf{T} \cdot (\mathbf{X_0} + \boldsymbol{\alpha}). \tag{5.2}$$

The variables in this equation are defined as follows:

- $\mathbf{X}$ is a 4×1 column vector containing the positions (x,y) and slopes (x',y') of the proton at a location halfway between the two VFPS Roman Pot detectors;
- $\mathbf{T}$ is a 4×5 transport matrix describing the optical functions between the IP and the VFPS;
- $\mathbf{X}_0$ is a 5×1 column vector containing the positions (x_0,y_0), slopes (x'_0,y'_0) and relative energy deviation (ξ_0) at the interaction point (IP) before the diffractive interaction;
- finally, $\boldsymbol{\alpha}$ is a 5×1 column vector describing the diffractive interaction and containing zeroes for the change in positions, the horizontal and vertical scattering angles ($\theta_x = \theta\ cos\phi$ and $\theta_y = \theta\ sin\phi$, where θ and ϕ are the polar and azimuthal angles of the leading proton at the IP, respectively) for the change in slopes and the relative energy gain ($-x_{I\!P}$) for the change in relative energy deviation.

In order to determine the proton momentum, one needs to solve equation (5.2) for $\boldsymbol{\alpha}$.

No attempt is made to include information on $\mathbf{X}_0$ measured by the main H1 detector. Neglecting the beam spread and divergence at the IP and thus assuming $\mathbf{X}_0 = 0$, results in additional smearing of the measured coordinates which has to be included in the uncertainty on $\mathbf{X}$. In this case the equation (5.2) reduces to a (over-determined) system with 4 equations and three unknowns:

$$\mathbf{X} = \tilde{\mathbf{T}} \cdot \tilde{\boldsymbol{\alpha}} \tag{5.3}$$

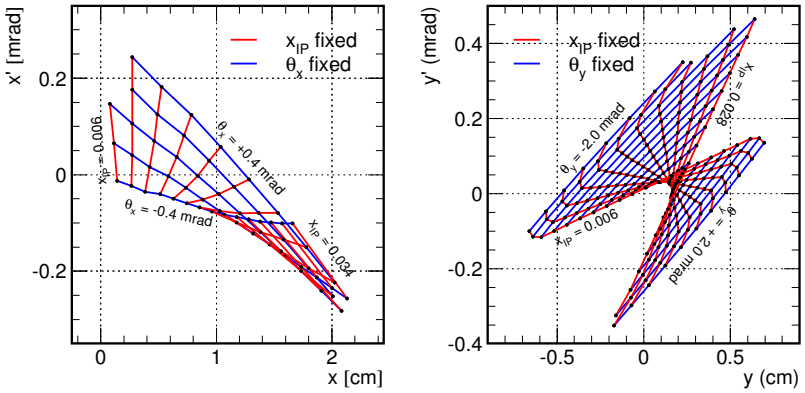

Figure 5.5: Lines of constant relative energy loss ($x_{I\!P}$) and scattering angles (θ_x, θ_y) are drawn in the horizontal and vertical planes of slope versus position of the proton halfway between the VFPS stations. Lines of constant $x_{I\!P}$ are drawn in steps of 0.002 and lines of constant $\theta_x(\theta_y)$ are drawn in steps of 0.2 mrad. Only points inside the VFPS acceptance are displayed.

where $\tilde{\boldsymbol{T}}$ is now a 4×3 matrix derived from $\mathbf{T}$ and $\tilde{\boldsymbol{\alpha}}$ is a 3×1 column containing the scattering angles (θ_x and θ_y) and the relative energy gain ($-x_{I\!P}$).

In many applications the transport matrices $\mathbf{T}$ and $\tilde{\boldsymbol{T}}$ can be taken to be constant such that equation (5.2) is a simple linear system of four equations and three unknowns. Moreover, in the absence of sextupole and higher multipole magnets, the horizontal and vertical coordinates decouple, such that the problem is reduced to two independent systems of two equations, that can be solved for (θ_x, $x_{I\!P}$) and (θ_y, $x_{I\!P}$), respectively, yielding two independent determinations of $x_{I\!P}$.

In the case of the VFPS, however, where differences in the measured coordinates of a few tens of microns are relevant, the linear approximation, which is valid for small energy deviations, positions and slopes, is no longer adequate. Strong non-linear effects, originating from the magnets in the cold section of HERA, need to be taken into account, effectively making the matrix elements of $\mathbf{T}$ dependent on the proton momentum. Moreover the presence of sextupole magnets will introduce a coupling between the vertical and horizontal planes. Figure 5.5 shows the grid with lines of constant energy loss and scattering angles projected onto the horizontal and vertical planes of slope versus position at the VFPS location. As can be seen, the deviations from a rectangular (linear) grid are large. The change in position when keeping the scattering angle fixed is also much smaller in the vertical direction than in the horizontal direction, especially for small scattering angles. This is because the strong energy dispersion only exist in the horizontal plane.

Reconstruction of proton kinematics

A neural net method was proposed and tested for the reconstruction of the proton momentum from the measured impact coordinates and slopes in the VFPS detectors in [26]. Resolutions of the reconstructed kinematic variables were determined. A quality criterion was developed in [26] to assess the probability for a well-reconstructed proton and to derive error estimates on the reconstructed kinematic variables. Here only a brief account on results from [26] is given.

There are sources of impurities which affect the VFPS measurement. Since the VFPS detectors operate in a highly active environment and they approach rather close to the nominal beam it can be expected that a fraction of spurious measurements will resemble the regular signal of leading protons. Likewise the reconstruction algorithm of the local proton tracks in the VFPS keeps more hypotheses of the reconstructed tracks and have to be assessed later on at the analysis level. In figure 5.6 it is illustrated what the spurious measurements look like in the VFPS (the upper row of plots). In the lower row of plots in figure 5.6 the spurious measurements are suppressed by means of using a quality criterion ($Q < 7$) which compares the VFPS measurement with expected measurement obtained from reconstructed kinematics based on that VFPS measurement, see [26] or see figure 5.7 for a sketch of quality estimation method. In figure 5.8 are shown errors of the reconstructed diffractive kinematics obtained by means of the neural network method. The simulated VFPS data are used containing spurious measurements which are suppressed by means of use of the quality criterion ($Q < 7$), see [26].

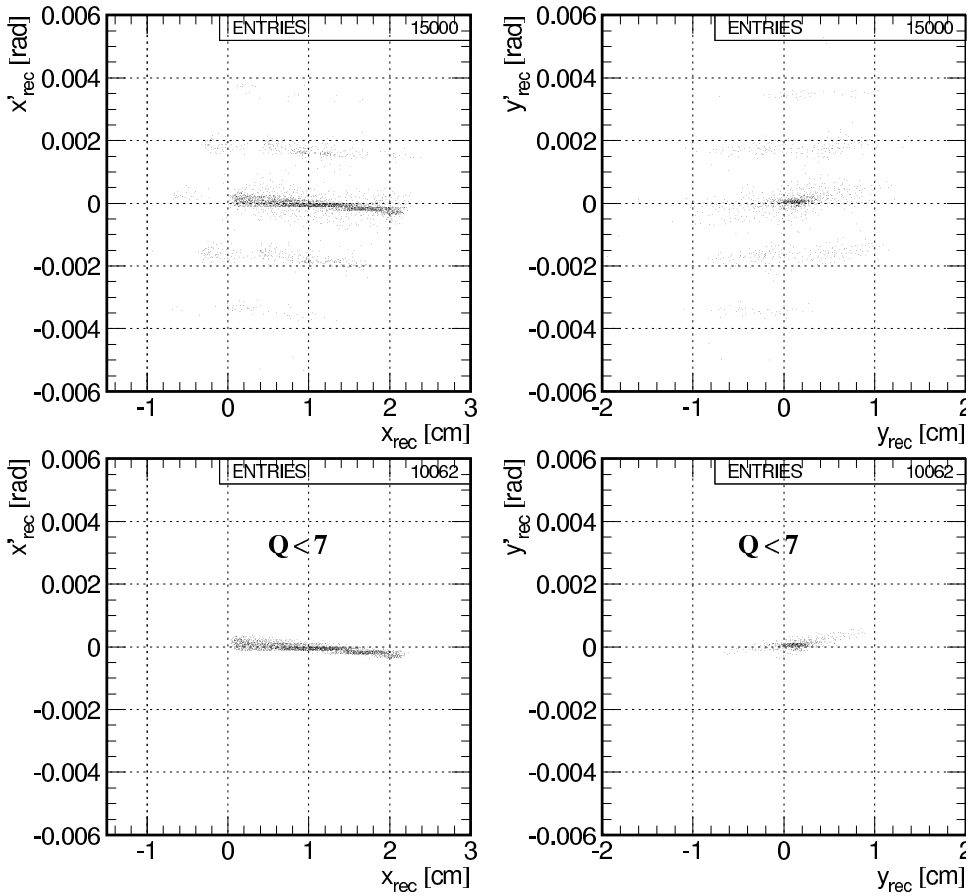

Figure 5.6: Simulation of VFPS measurements of intercepts and slopes; x versus x' and y versus y'. In the upper row are shown the raw simulated data containing the spurious hits. In the lower row the purged data are shown with a quality criterion applied of $Q < 7$.

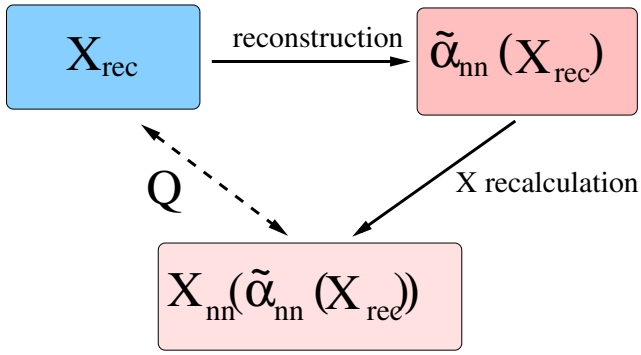

Figure 5.7: A quality estimator of the reconstructed kinematics. The X_{rec} denotes the measured intercepts and slopes in the VFPS. The $\tilde{\alpha}_{nn}(X_{rec})$ is the reconstructed proton kinematics ($x_{I\!P}$, t and ϕ) reconstructed by means of neural network method. Finally, the $X_{nn}(\tilde{\alpha}_{nn}(X_{rec}))$ denotes recalculated impact coordinates in the VFPS obtained from the reconstructed proton kinematics by means of neural network fits of the beam optics. The difference between X_{rec} and X_{nn} values gives the value of Q. Large value of Q indicate a non-reliable reconstruction in the given event (typically spurious hits with random VFPS impact coordinates).

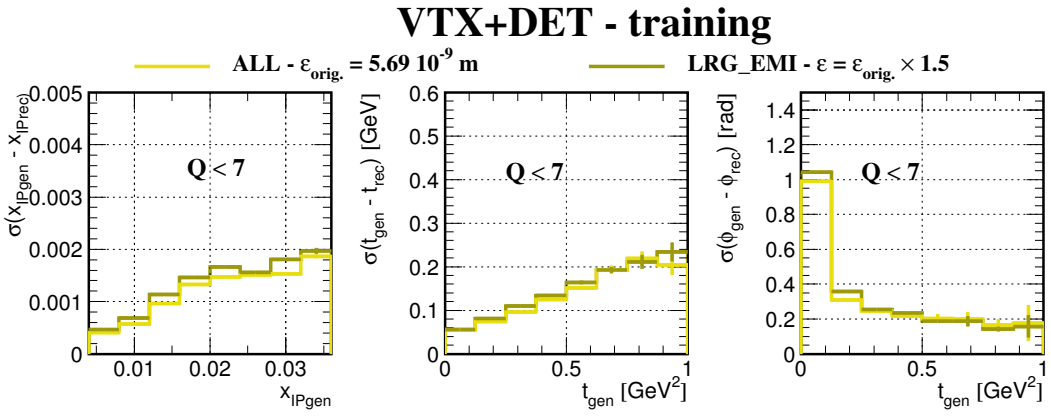

Figure 5.8: The simulation of expected errors of reconstructed diffractive proton kinematics $x_{I\!P}$, t and ϕ plotted as a function of $x_{I\!P}$ and t_{gen}. The reconstruction was obtained by means of using a neural network method on a raw simulated VFPS data. The quality criterion $Q < 7$ helps to purge the data sample. The error dependencies are compared for two beam emittance (ε) values used in the simulation in order to test the stability of the method with respect to the uncertainty on the beam conditions. The title "VTX+DET training" means that the neural network was trained with simulated sample using the smearing of the interaction point position as well as the full VFPS detector response simulation.

Chapter 6

Monte Carlo and NLO QCD Predictions

Monte Carlo (MC) generators became an essential part of any analysis in H1 and in high energy physics in general. MC generators are used to generate physics events by means of use of desired matrix elements, usually at leading order of α_s. Moreover, they employ phenomenological models to perform a fragmentation into observable color singlet hadrons (hadronization). The MC generators can be either used for predictions of cross sections or other observables. Generated MC events can be subjected to a detector simulation. Provided the fidelity of the detector simulation is ensured one can use the MC to correct the measured data (detector level) to the level unaffected by the detector effect - to the level of stable hadrons (hadron level). In this thesis the MC is used for the correction to the hadron level. Also an estimation of a background contribution is obtained by means of MC simulation.

The measured cross sections are compared with next-to-leading order (NLO) QCD calculations. Here yet another use of MC comes into play. The NLO QCD calculations predict cross sections at the level of partons. The prediction at the level of stable hadrons is obtained by means of so called hadronization corrections, $\delta_{hadr.}$. These are calculated by means of MC, as well.

6.1 Monte Carlo Models

In the following sections an overview of the Monte Carlo samples used as a signal or the background will be given. Also MC used for estimation of leading proton dissociation will be introduced.

In figure 6.1 is shown a space-time picture of a DIS process generation with a standard Monte Carlo program. The phases of initial and final state QCD radiation are shown which take place before and after the hard sub-process, respectively. The final state color non-singlet objects undergo a transition into observable hadrons by means of use of a hadronization model.

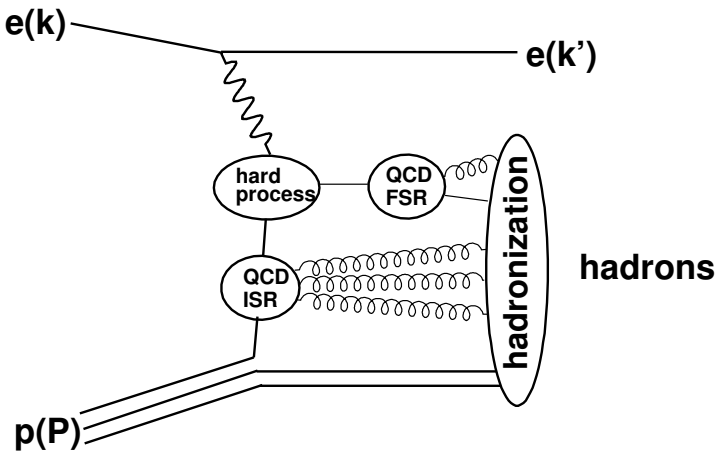

Figure 6.1: A schematic diagram of the space-time generation of a DIS event in MC. QCD ISR denotes the initial radiation of partons (gluons) from a primary parton (quark) which takes part in the hard sub-process. Hard sub-process produces the hard partons (quark) which can radiate partons (gluon) by final state QCD radiation (FSR). All partons hadronise into observable hadrons by means of use of a hadronization model.

6.1.1 Signal Monte Carlo

The signal events are generated with the Rapgap 3.1 Monte Carlo generator [27] using the H1 2006 Fit B DPDF [14] both for the direct and resolved processes and for $I\!P$ and $I\!R$ exchange with an intact (elastic) leading proton. The direct processes are generated with QCD sub-processes; boson-gluon fusion (BGF) with light flavours and charm, the QCD Compton (QCD-C) with light flavours. The resolved processes are generated with light flavours for two-two parton hard sub-processes. The photon structure function GRV-G LO [28] is used. In figure 6.2 are shown example diagrams of the above hard sub-processes. Higher order QCD effects are approximated using the initial and final state QCD radiation. The hadronization is performed by a string fragmentation implemented in Jetset [29]. The signal samples are generated at $\sqrt{s} = 318$ GeV with following kinematical constraints

$$Q^2 < 0.1\ \mathrm{GeV}^2\,, \tag{6.1}$$

$$\hat{p}_T > 2\ \mathrm{GeV}\,, \tag{6.2}$$

$$0.15 < y < 0.8\,, \tag{6.3}$$

$$x_{I\!P} < 0.15\,, \tag{6.4}$$

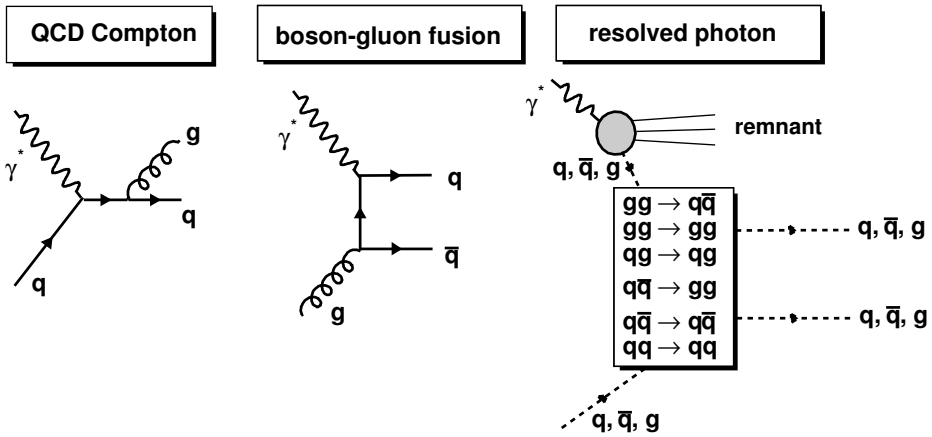

Figure 6.2: Diagrams of signal hard sub-processes generated with the Rapgap Monte Carlo generator.

where $\hat{p}_T$ is the transverse momentum of the hard scattered parton.

In table 6.1 the statistics of the signal samples can be found. Eventually, the samples are submitted to simulation of the detector response.

process	events $I\!P$	events $I\!R$
BGF-uds	1.8 M	190 k
BGF-c	870 k	110 k
QCD-C	330 k	140 k
res-uds	12 M	2.5 M

Table 6.1: Generated statistics of the signal Rapgap samples.

6.1.2 Monte Carlo for non-diffractive background

In order to estimate the non-diffractive background contribution the Pythia MC generator [29] is used in an inclusive photoproduction mode using CTEQ 5L LO proton structure function [30] and GRV-G LO photon structure function. Only the inclusive photoproduction background is considered to contribute to the analysis because of use of the electron tagger. It is unlikely to fake the electron in the tagger - only the Bethe-Heitler electrons could do it. Nevertheless, by means of a cut on energy in the photon detector it is easy to suppress the Bethe-Heitler processes. Hence, there is no background from the inclusive deep inelastic scattering.

6.1.3 Monte Carlo for leading proton dissociation

The fraction of events with leading proton dissociation is studied by means of use of DIFFVM MC generator [31]. Two samples with diffractive production of J/ψ are used; with elastic leading proton and with leading proton dissociation switched on.

6.2 Next to Leading Order QCD Predictions

As the renormalization scale ($\mu_r^2 \sim p_T^2$) is rather low a higher α_s order contribution must be taken into account. Next-to-leading order (NLO) QCD calculations are used to predict the cross sections.

There are two independent NLO QCD programs used in this thesis; the Frixione et al. (FR) program [32] and the Klasen & Kramer (KK) program [33]. The NLO QCD predictions are obtained setting the renormalization and factorization scales to $\mu_r^2 = \mu_f^2 = p_T^{2,\ jet1}$ with fixed number of flavours $N_f = 5$ and $\Lambda_5 = 0.228$. The DPDF fits obtained by H1 are used; H1 2006 Fit A and Fit B DPDF [14] and H1 2007 Fit Jets DPDF, which can be found in [15]. For the resolved photon, the $\gamma-$PDF parameterization GRV HO [28] is used. The non-perturbative transition to the level of stable hadrons is included in the predictions by means of hadronization corrections obtained from the Rapgap Monte Carlo samples generated with the pomeron and reggeon exchange.

6.2.1 Hadronization corrections

The NLO QCD calculations give predictions at the level of partons. It must be accounted on the non-perturbative transition to the hadron level by means of use of so called hadronization corrections. The corrections are obtained from the signal Monte Carlo samples. The signal MC samples are generated with QCD radiations before and after the hard sub-process, therefore, higher α_s order effects are modeled to some extent. Such a list of partons emerging both from the hard subprocess and from the QCD radiations together with the scattered electron is referred to as a parton level in this thesis. The effect of hadronization smears the parton level kinematics and the hadronization corrections describe this kind of smearing.

The hadronization corrections are calculated in each bin of a given observable as a ratio of cross sections at the hadron level to the parton level in the MC sample.

$$(1 + \delta_{hadr.})_i = \left(\frac{\sigma_{dijet}^{hadron}}{\sigma_{dijet}^{parton}} \right)_i , \tag{6.5}$$

where i denotes the measured bin.

With a bit of anticipation (relying on a good correspondence between the parton and hadron level, see section 7.6) in figures 6.3 and 6.4 the hadronization corrections are plotted for the kinematics of *low* p_T^{jets} and *high* p_T^{jets}, respectively, in a final binning (see section 9.2) for the event variables of

$$\begin{array}{ccc} x_\gamma & log_{10}(x_{I\!P})\,, & z_{I\!P}, \\ p_T^{jet1}\,, & \langle \eta^{jets} \rangle\,, & |\Delta\eta^{jets}|, \\ M_{12}\,, & M_X\,, & W. \end{array}$$

The hadronization corrections, $\delta_{hadr.}$, are $\sim -16\%$ on average in both kinematical ranges. In the last but one bin of x_γ hadronization correction plots (6.3 (a), 6.4 (a)) one can see excessive values which are caused by large amounts of migrations of direct ($x_\gamma \sim 1$) events towards lower values of x_γ due to smearing caused by the hadronization.

The hadronization corrections are calculated with one hadronization model (Jetset) only. Thus, there is no estimation of errors of the hadronization corrections made in this thesis.

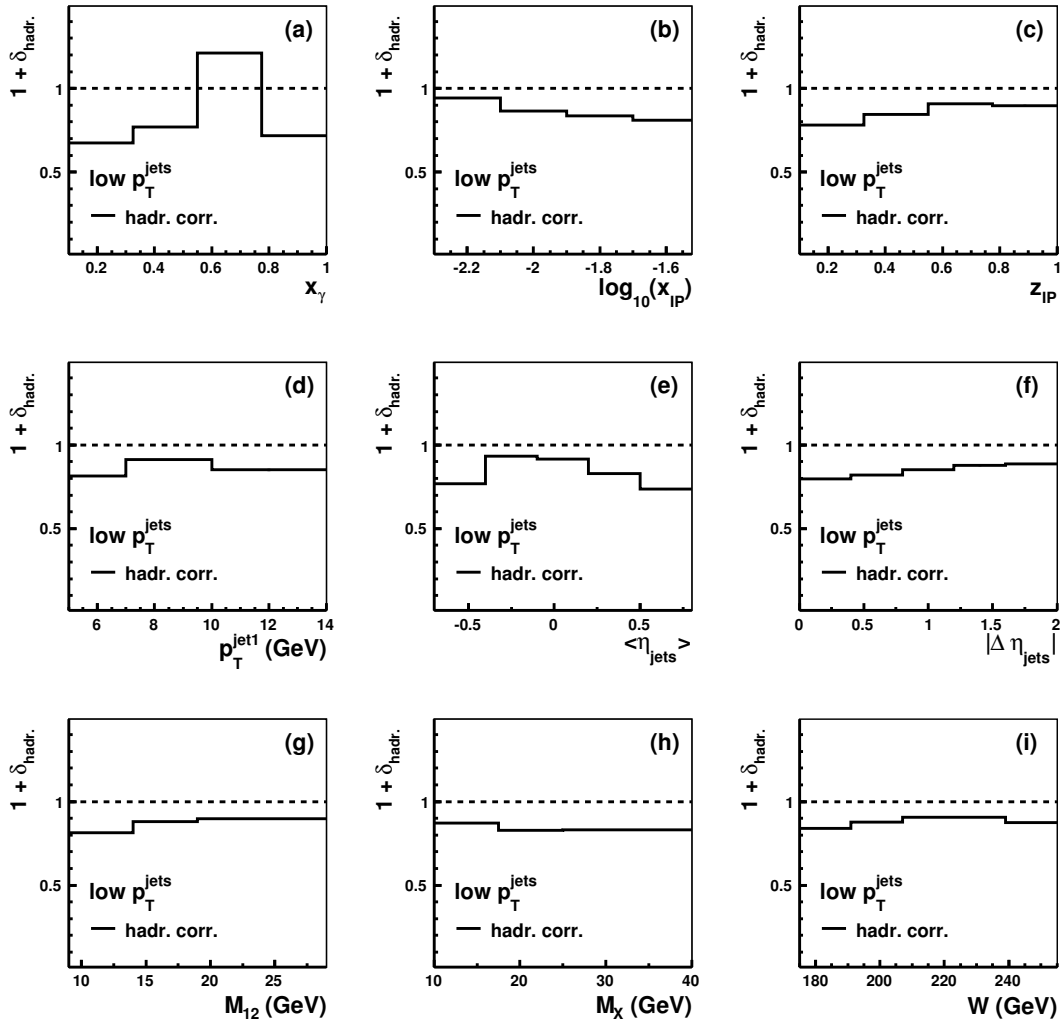

Figure 6.3: Hadronization corrections $1 + \delta_{hadr.}$ (full line histogram) for *low* p_T^{jets} kinematics. Dashed line indicates unity. Corrections plotted for x_γ, $log_{10}(x_{I\!P})$, $z_{I\!P}$, p_T^{jet1}, $\langle \eta^{jets} \rangle$, $|\Delta\eta^{jets}|$, M_{12}, M_X, W in $(a) - (i)$, respectively.

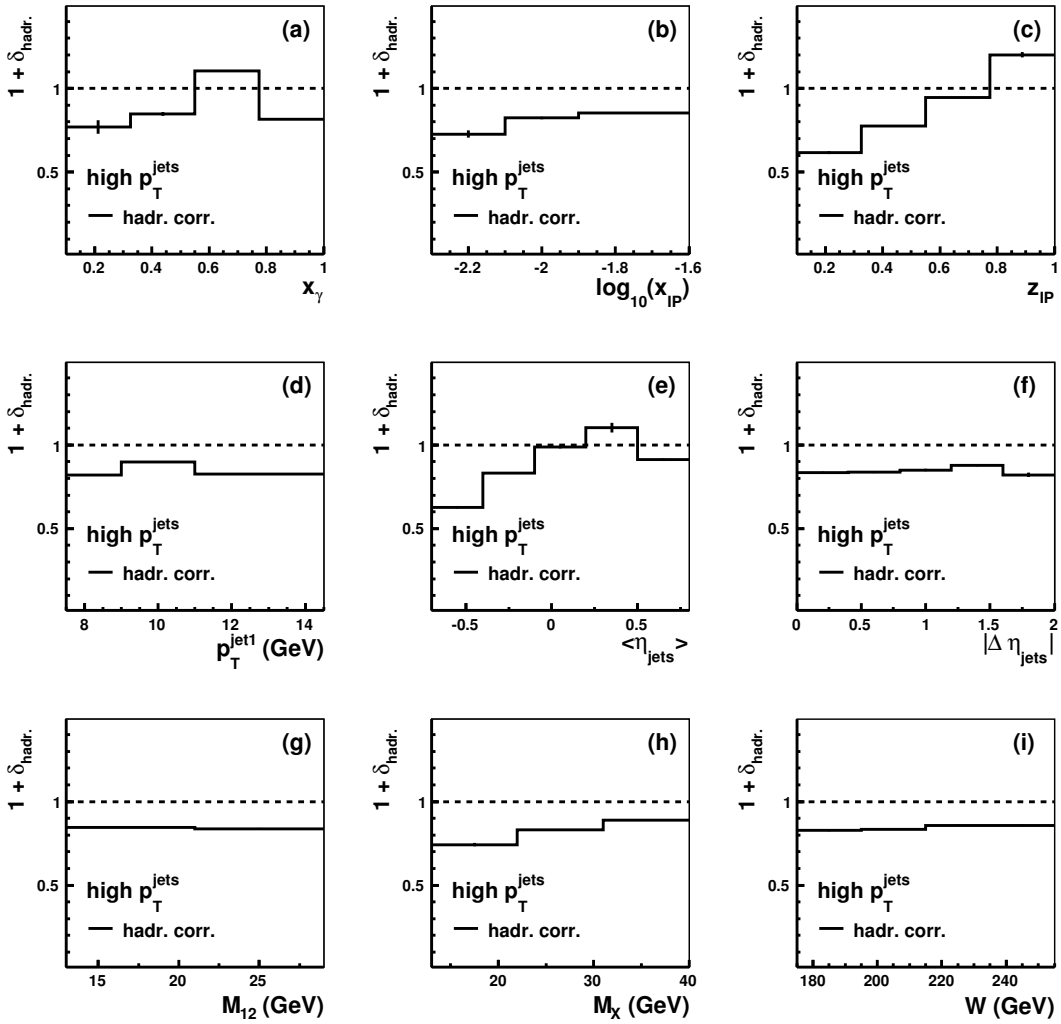

Figure 6.4: Hadronization corrections $1+\delta_{hadr.}$ (full line histogram) for *high* p_T^{jets} kinematics. Dashed line indicates unity. Corrections plotted for x_γ, $log_{10}(x_{I\!P})$, $z_{I\!P}$, p_T^{jet1}, $\langle\eta^{jets}\rangle$, $|\Delta\eta^{jets}|$, M_{12}, M_X, W in $(a)-(i)$, respectively.

Chapter 7

Reconstruction of the Kinematics

In this chapter an overview is given of how the kinematics are reconstructed. Also the criteria for jet finding are introduced. Quality of the reconstruction is judged from correlation and resolution plots.

7.1 Detector Response Simulation

The finite detector resolution and limited acceptance cause smearing of the event observables if the transition from hadron to detector level is made. A reasonable correlation of the hadron level quantities with the detector level ones is essential for reliable procedure of correction of the measured data back to the hadron level. MC samples used in the analysis are subjected to the detector simulation for the detector status of the 1999 and 2000 positron running period.

7.2 Energy Flow Algorithm for Hadronic Reconstruction

An object oriented framework is established in H1 (H1OO) to realize reconstruction issues and to provide interface for physics analyses too. An electron, muon and hadronic final state (HFS) finders are designed to perform the task of reconstruction. The reconstruction algorithms make use of all the knowledge gathered during the HERA I operating phase.

An energy flow algorithm for the HFS reconstruction so called Hadroo2, [34], uses information obtained from the track or calorimetric measurement and creates so called particle candidates. The idea is such that the best measurement is used for the particle candidate creation.

The algorithm proceeds as follows. Each track is assumed to originate from a pion with energy

$$E^2_{track} = p^2_{track} + m^2_\pi = p^2_{T,track}/sin^2\theta + m^2_\pi, \tag{7.1}$$

measured with error

$$\frac{\sigma_{E_{track}}}{E_{track}} = \frac{1}{E_{track}}\sqrt{\frac{P_{T,track}^2}{sin^4\theta}(cos^2\theta)\sigma_\theta^2 + \frac{\sigma_{P_{T,track}}^2}{sin^2\theta}}, \tag{7.2}$$

where the $\sigma_{P_{T,track}}$ and σ_{theta} are the corresponding errors on P_T and θ (transverse momentum and polar angle, respectively) of the track neglecting their correlations, which are small anyway.

Now, for each track an evaluation is made what would be the error if the particle were measured in the calorimeter. This evaluation is purely track based as there can be contributions of neutral particles in the calorimetric clusters. It is calculated what would be the expected error of measurement based on the LAr information, i.e.

$$\left(\frac{\sigma_E}{E}\right)_{LAr\ expect.} = \frac{\sigma_{E_{LAr\ expect.}}}{E_{track}} \simeq \frac{0.5}{\sqrt{E_{track}}}, \tag{7.3}$$

where the value of 0.5 is the energy resolution constant of the hadronic section of LAr calorimeter, see section 4.2.2.

The track measurement is considered to be better than the calorimetric one if

$$\frac{\sigma_{E_{track}}}{E_{track}} < \frac{\sigma_{E_{LAr\ expect.}}}{E_{track}}. \tag{7.4}$$

There are three types of tracks classified according to an azimuthal angle; forward, central and combined corresponding roughly to $6° < \theta < 25°$, $20° < \theta < 160°$ and $0° < \theta < 40°$, respectively. The relative energy resolution comparisons for these tracks compared with LAr resolution expectation can be seen in figure 7.1. Obviously, the track measurement provides a good precision at low energies whereas calorimetric measurement is getting better at higher energies of the particles.

If the track measurement is preferred, clusters "behind" the extrapolated track are suppressed according to an algorithm which is not described in this text. If the calorimetric measurement is expected to give better precision, still, the track measurement can be used if the clusters do no pass certain criteria, otherwise, the calorimetric measurement is used for the particle candidate creation. After having treated all the tracks and their associated clusters the remaining clusters energies are rescaled in such a way that they represent massless particles. They correspond to neutral hadrons or to charged particles with badly measured tracks.

The Hadroo2 energy flow reconstruction algorithm is used to reconstruct the hadronic final state at the detector level both for data and MC in this thesis.

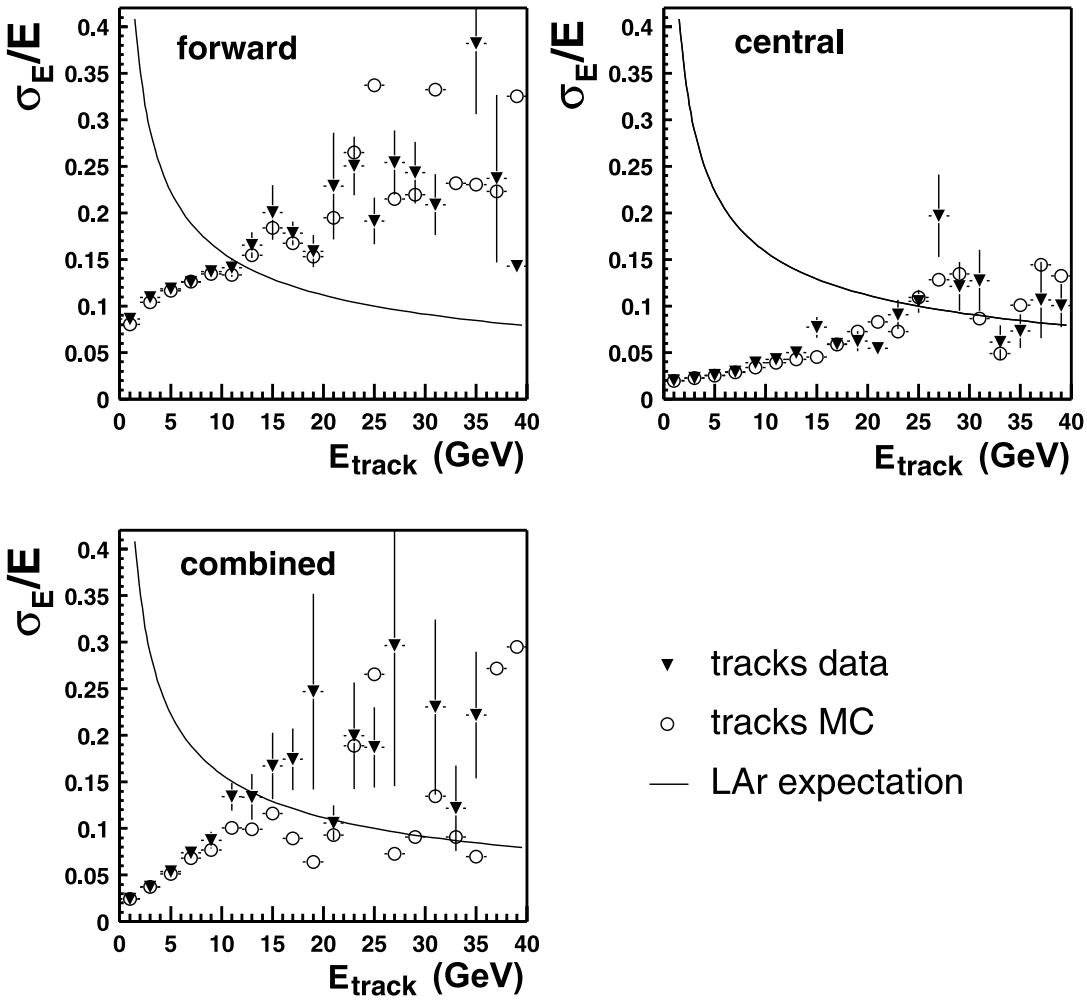

Figure 7.1: Relative resolutions for forward, central and combined tracks compared with the *LAr* expected resolutions, from [34].

7.3 The Inclusive k_T Algorithm

The jets are observed as a consequence of an underlying parton dynamics. Transition from the parton to the hadron level (or hadron to detector level), however, smears the event kinematics. The jet algorithm attempts to describe the jet topology as closely as possible between the levels. The final state objects are usually grouped together according to some defined metric. There are more jet algorithms available but no of them is superior. In this thesis the inclusive k_t jet algorithm is used [35]. It is designed for the DIS processes and originates in Durham jet algorithm [36] which was proposed for e^+e^- processes. It posses all necessary features of; infrared and collinear safety; simple use in theoretical and experimental practice; small sensitivity to hadronization models.

The k_T algorithm is formulated in a Breit frame which is the center of mass frame of the virtual photon and the corresponding parton which moves in a opposite direction after the scattering than the proton remnant. The idea behind the k_t algorithm is to combine particles with particularly close momenta. These particles are regarded to be a part of a particle cascade generated by one of the hard partons from the final state. Experimentally the cascades are observed as local energy flow enhancements originating in energy depositions of particles from the cascade which have small relative distances with respect to each other in η and ϕ. The algorithm starts with a list of the final state objects. These objects can be partonic fourmomenta or hadronic final state fourmomenta or fourmomenta of detector level final state objects (particle candidates). The objects are called protojets and the aim is to merge them into a smaller number of final jets. Each of the protojets is characterized by its transverse momentum ($p_{T,i}$) azimuthal angle (ϕ_i) and pseudorapidity (η_i). The protojets are merged into new objects as follows.

1. For each protojet define a quantity

$$d_i = p_{T,i}^2 \ . \tag{7.5}$$

2. For each protojet pair define a distance

$$d_{ij} = min(p_{T,i}^2 \, , \, p_{T,j}^2) \, [(\eta_i - \eta_j)^2 + (\phi_i - \phi_j)^2]/R^2 \ . \tag{7.6}$$

   The R is a tunable parameter which is usually set to 1.

3. Find the smallest of all d_i and smallest d_{ij} using this d_i. Label the minimal d_{ij} with d_{min}.

4. Merge the ij pair of protojets with d_{min}. Label this new objects as a new protojet k and remove the original pair ij. Properties of the new protojet k are determined by following scheme

$$p_{T,k} = p_{T,i} + p_{T,j} \ , \tag{7.7}$$

$$\eta_k = \frac{p_{T,i} \cdot \eta_i + p_{T,j} \cdot \eta_j}{p_{T,k}} \ , \tag{7.8}$$

$$\phi_k = \frac{p_{T,i} \cdot \phi_i + p_{T,j} \cdot \phi_j}{p_{T,k}} \ . \tag{7.9}$$

5. If there is no d_{kj} smaller than the d_k present then d_{min} is given by the d_k and the corresponding protojet k is removed from list of protojets and is added among the jets.

The whole procedure repeats until no protojets are present. The result is a list of jets with successively increasing p_T^2.

The k_T algorithm is invariant under longitudinal boosts. It does not affect the grouping of the individual protojets. That is why it is used in the laboratory frame in this thesis because in photoproduction a boost into the Breit frame would result merely in a boost along the z axis. The k_T jet algorithm is used at the detector level of data and MC and also at the hadron and parton level of MC.

7.4 Reconstruction Formulae

The kinematics are reconstructed according to the following formulae. The variables in the formulae are always considered at respective levels (detector, hadron, parton).

$$y = y_e = 1 - \frac{E_{e'}}{E_e^{beam}}, \tag{7.10}$$

$$W = \sqrt{s\, y_e}, \tag{7.11}$$

$$x_\gamma = \frac{\Sigma_{jets} E_i - P_{z,i}}{\Sigma_{HFS} E_i - P_{z,i}}, \tag{7.12}$$

$$x_{I\!P} = \frac{\Sigma_{HFS} E_i + P_{z,i}}{2 \cdot E_p^{beam}}, \tag{7.13}$$

$$z_{I\!P} = \frac{\Sigma_{jets} E_i + P_{z,i}}{2 \cdot x_{I\!P} \cdot E_p^{beam}}, \tag{7.14}$$

$$M_{12} = \sqrt{J^{(1),\mu} \cdot J_\mu^{(2)}}, \tag{7.15}$$

$$M_X = \sqrt{s\, y_e\, x_{I\!P}}, \tag{7.16}$$

$$\left|\Delta\eta^{jets}\right| = \left|\eta^{jet1} - \eta^{jet2}\right|, \tag{7.17}$$

$$\left\langle \eta^{jets} \right\rangle = \frac{1}{2}\left(\eta^{jet1} + \eta^{jet2}\right). \tag{7.18}$$

Where, E_e^{beam} and E_p^{beam} are the lepton and proton beam energies, respectively. The $E_{e'}$ is the scattered electron energy. The $J^{(1)\mu}$ and $J_\mu^{(2)}$ are the four vector components of the jets.

At the detector level the formulae for y and W take an advantage of the electron energy measurement in the e-tagger. The reconstruction of the x_γ profits from cancellations of detector effects which influence the $E - p_z$ measurements. The $x_{I\!P}$ reconstruction formula makes use of a good instrumentation of H1 in the forward region. Nevertheless, as it will be shown in next section there can be a leakage of particles in the forward region of the detector which affects measurements of large values of $x_{I\!P}$ as well as large values of M_X. In general, the choice of the formulae may differ between the various analyses depending on the phase space corner of the measurement. Usually, the most suitable reconstruction formula for each variable is chosen according to study of correlations and resolutions, see section 7.5.

7.5 Hadron-Detector Level Correspondence

The quality of reconstruction of the kinematics at the detector level with respect to the hadron level can be judged from scatter plots for each observable ($x_{hadr.}$ versus $x_{det.}$) obtained by means of using a MC sample. A good correlation of the kinematics at both levels is desirable. In a straightforward way resolution plots can be projected from the correlation plots ($x_{hadr.} - x_{det.}$).

The hadron-detector level correlation and resolution plots are shown for combined Rapgap pomeron and reggeon exchange samples for the low p_T^{jets} kinematics in figure 7.2 (x_γ, $x_{I\!P}$, $z_{I\!P}$), figure 7.3 (M_X, M_{12}), figure 7.4 (p_T^{jet1}, η^{jet1}, ϕ^{jet1}). The resolution plots are fitted by a Gaussian function and the results of the fit is shown in the figures. In some cases deviations from Gaussian shapes are observed. The correlations are usually satisfactory, except for p_T^{jet1}, where large migrations are observed in the low p_T^{jet1} region and consequently sort of broad Gaussian fit, $\sigma = 0.6$ GeV. This is caused by a low minimum p_t required on the jets which means that the jets are broad, there are no prominent leading particles in the jet which would be less influenced by the measurement at the detector level. Such an effect spoils the precision of the reconstruction of p_T^{jet1} observable at the detector level with respect to the hadron level. Concerning the η^{jet1} and ϕ^{jet1} they are very well correlated between the hadron and detector levels. It is worth mentioning that the p_T^{jet1} correlation and resolution is obtained by using the hardest p_T jet from both levels. On the other hand, the η^{jet1} and ϕ^{jet1} correlations and resolutions are obtained by means of considering the highest p_T jet at the hadron level and a jet from the detector level which spatially matches better (in η and ϕ space) to this hadron level jet. Further comments concern the variables sensitive to the mass of the diffractive system X, i.e. the $x_{I\!P}$ and M_X. As it was already mentioned, due to losses which occur in the forward region mainly because of leakage of particles downstream the beampipe, there is a somewhat poorer correlation (and consequently offset mean value of the resolution) at high values of $x_{I\!P}$ and M_X. This effect can be compensated by an additional recalibration of the two reconstructed quantities by factors obtained from the MC and applied to MC samples and measured data, as well. Nevertheless, in this thesis no such recalibration is applied neither to $x_{I\!P}$ nor to M_X. Price that would be paid by recalibration of $x_{I\!P}$ is an additional loss of statistics in data that would occur due to an $x_{I\!P}$ cut (3.7). Instead, it is accounted on possible imperfections of description of the data by the MC in the estimation of systematic uncertainties, see section 9.4.4.

In the same way are shown correlation and resolution plots for the high p_T^{jets} kinematics in figure 7.5 (x_γ, $x_{I\!P}$, $z_{I\!P}$), figure 7.6 (M_X, M_{12}), figure 7.7 (p_T^{jet1}, η^{jet1}, ϕ^{jet1}). The correspondence between the hadron and the detector level is satisfactory. Similar sort of comments applies to the correlation and resolution of p_T^{jet1}. A tail can be seen in the resolution plot of p_T^{jet1} in figure 7.7 which results in a rather broad resolution. Such a behaviour can be expected as the

1 GeV difference in p_T of both jets is less significant in the *high* p_T^{jets} kinematics. The point is that events containing jets with well distant transverse momenta are less likely to be misidentified at the hadron and detector levels. Thus, more frequent misidentifications are expected if the transverse momenta of both jets are comparable. Concerning the other correlations and resolutions for the *high* p_T^{jets} kinematics, the same comments apply as in the previous paragraph.

7.6 Parton-Hadron Level Correspondence

Very similar way of reasoning to the previous case of hadron-detector level correlations can be used for parton-hadron level correspondence check. In general, a good correspondence between these two levels is essential for calculation of hadronization corrections (section 6.2.1). As it was already mentioned the parton level is represented by all partons generated by the MC generator using the QCD radiation both before the hard scattering sub-process (initial state QCD radiation, ISR) and after it (final state QCD radiation, FSR) - often called parton showers. The kinematics of the parton level is reconstructed according to formulae defined in section 7.4 with jets obtained by means of using the jet algorithm with the input list in form of four-momenta of the partons.

The correlation and resolution plots for both p_T^{jets} kinematic schemes are shown for the parton-hadron level in a complete analogy to the hadron-detector level ones. In figures 7.8 - 7.13. They are obtained by means of using the Rapgap MC pomeron and reggeon exchange combined sample. From the p_T^{jet1} correlations and resolutions it can be deduced that the process of hadronization smears the event variables. There are again significant smearings observed in the at low values of p_T^{jet1} plots in figures 7.10 and 7.13 with resolution fit widths of $\sim$ 0.6 and 0.5 GeV for the kinematics of *low* p_T^{jets} and *high* p_T^{jets}, respectively. This is caused again by a broadness of the jets because the minimum p_t required on the jets causes that the partons from the hard sub-process are comparable to partons which emerge from the initial and final state QCD radiations. Of course there is no deviation in the $x_{I\!P}$ and M_X plots as there are no losses due to non-detection of the particles.

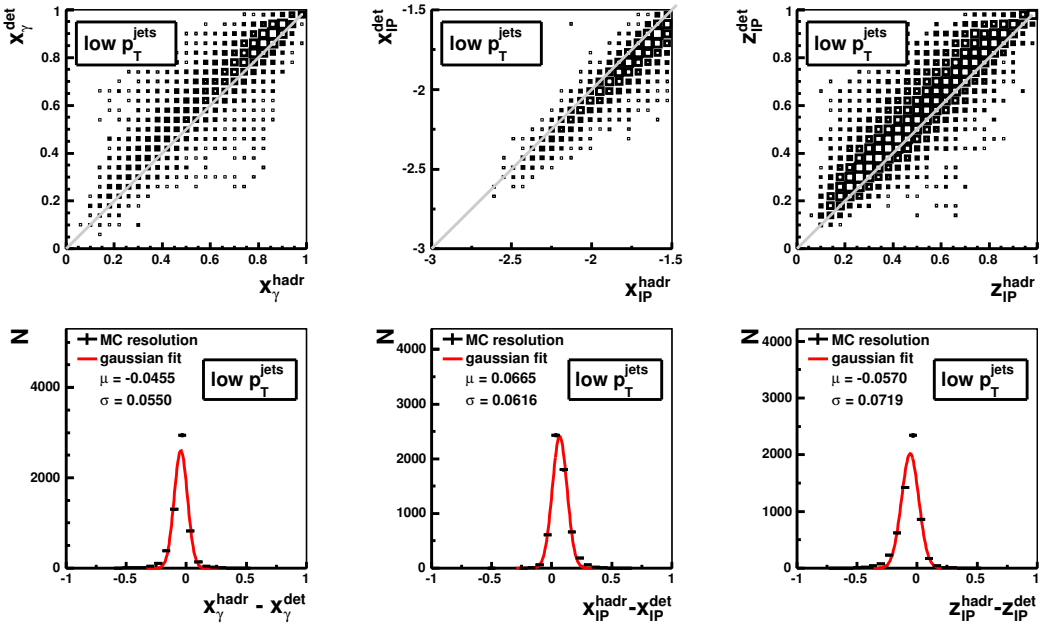

Figure 7.2: Correlation and resolution plots between the **hadron** and **detector** level variables for x_γ and $x_{I\!P}$, $z_{I\!P}$ in sample with $\boldsymbol{low\ p_T^{jets}}$ kinematics.

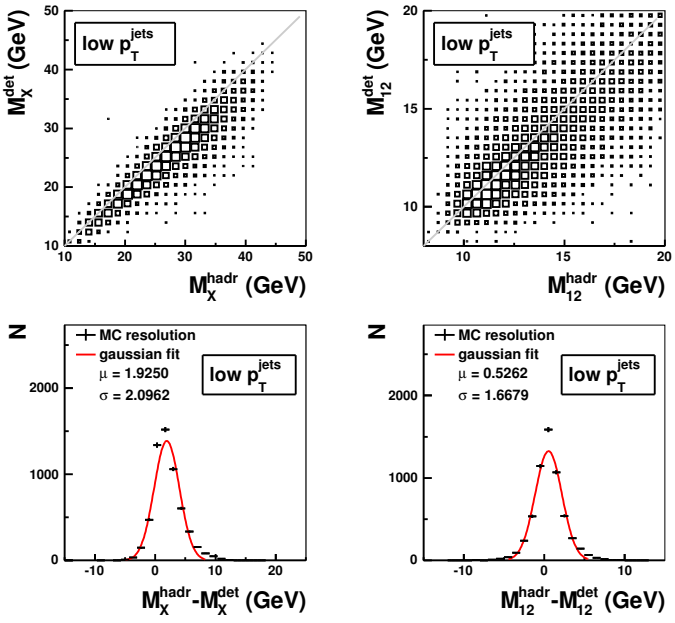

Figure 7.3: Correlation and resolution plots between the **hadron** and **detector** level variables for M_X and M_{12} in sample with $\boldsymbol{low\ p_T^{jets}}$ kinematics.

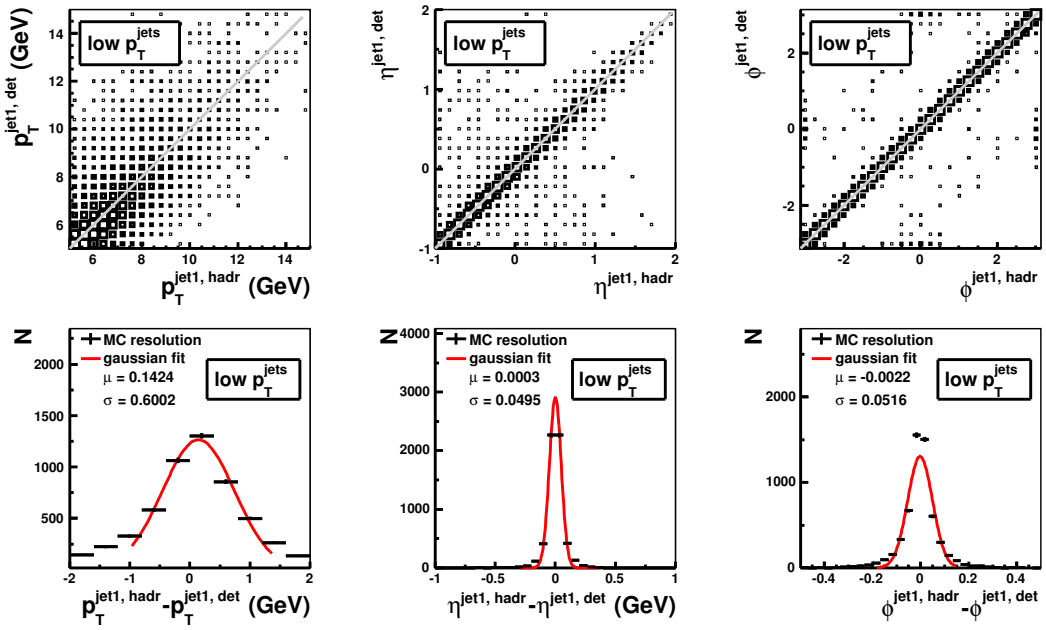

Figure 7.4: Correlation and resolution plots between the **hadron** and **detector** level variables for p_T^{jet1}, η^{jet1} and ϕ^{jet1} in sample with $\boldsymbol{low\ p_T^{jets}}$ kinematics.

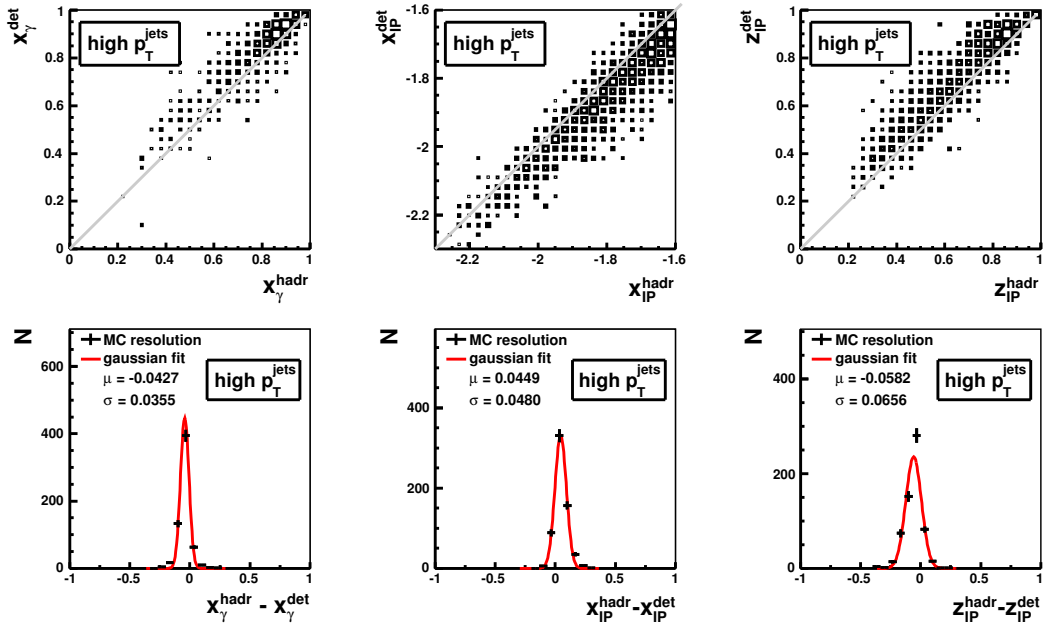

Figure 7.5: Correlation and resolution plots between the **hadron** and **detector** level variables for x_γ and $x_{I\!P}$, $z_{I\!P}$ in sample with $\boldsymbol{high\ p_T^{jets}}$ kinematics.

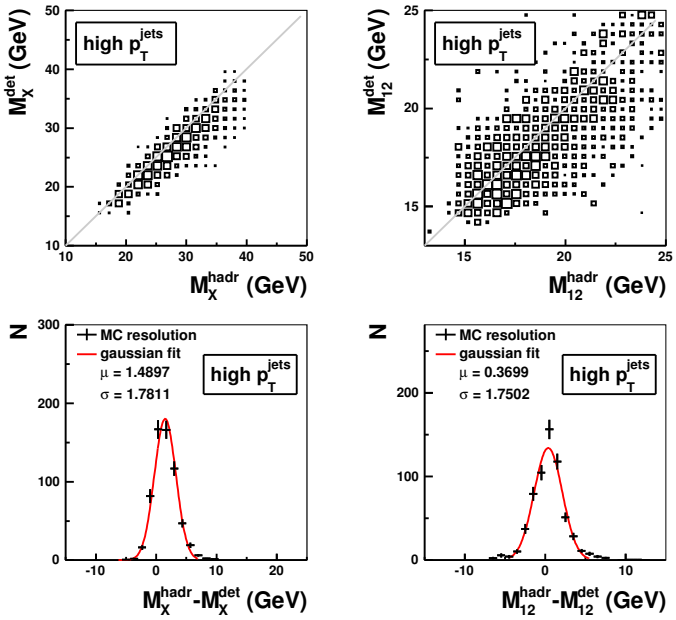

Figure 7.6: Correlation and resolution plots between the **hadron** and **detector** level variables for M_X and M_{12} in sample with $\boldsymbol{high\ p_T^{jets}}$ kinematics.

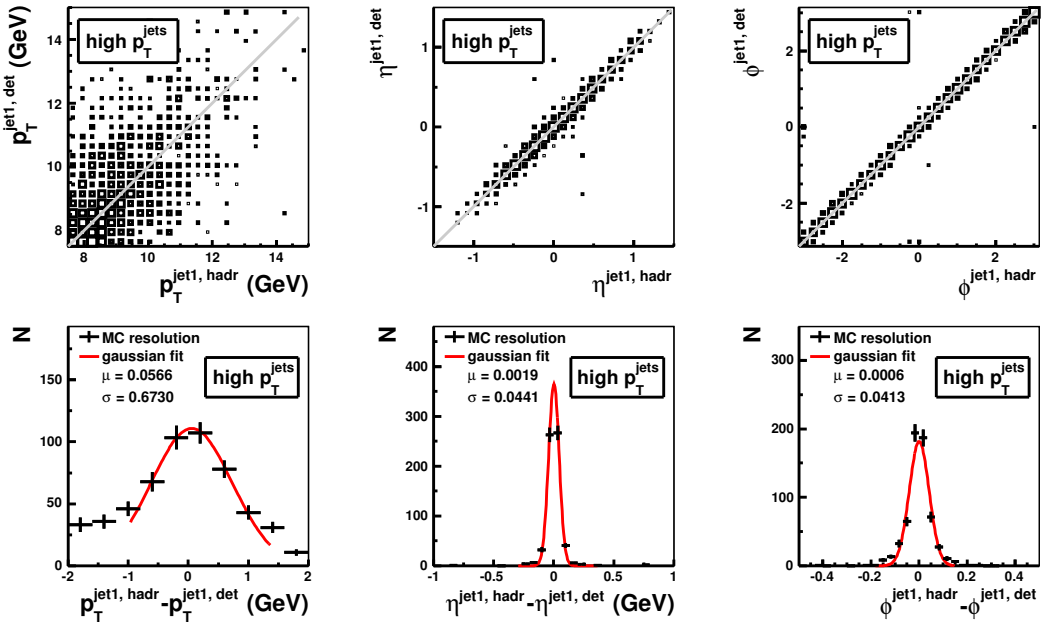

Figure 7.7: Correlation and resolution plots between the **hadron** and **detector** level variables for p_T^{jet1}, η^{jet1} and ϕ^{jet1} in sample with $\boldsymbol{high\ p_T^{jets}}$ kinematics.

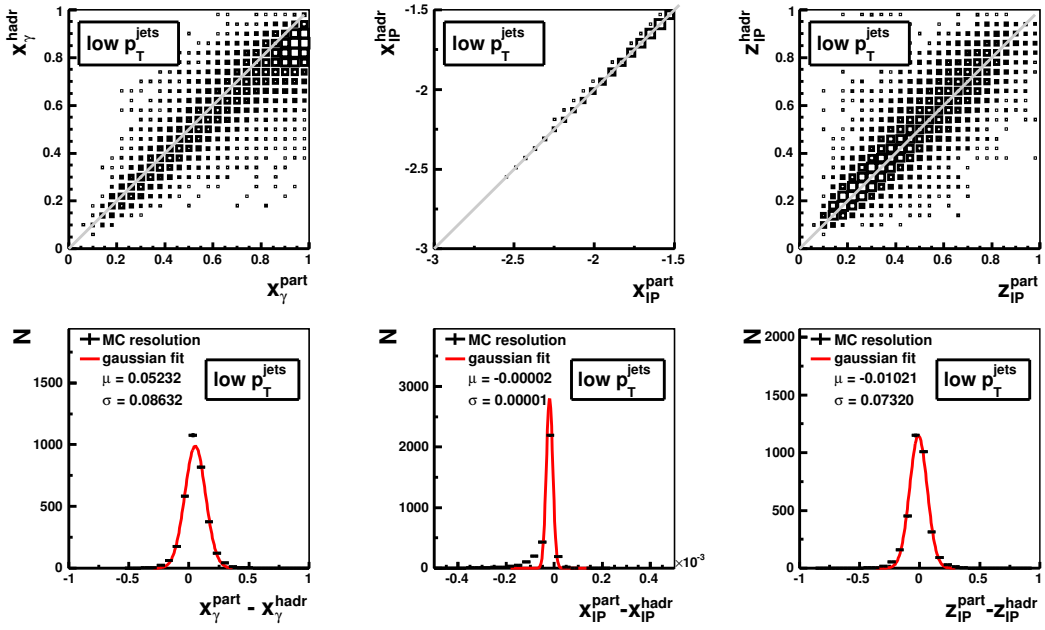

Figure 7.8: Correlation and resolution plots between the **parton** and **hadron** level variables for x_γ and $x_{I\!P}$, $z_{I\!P}$ in sample with $\boldsymbol{low\ p_T^{jets}}$ kinematics.

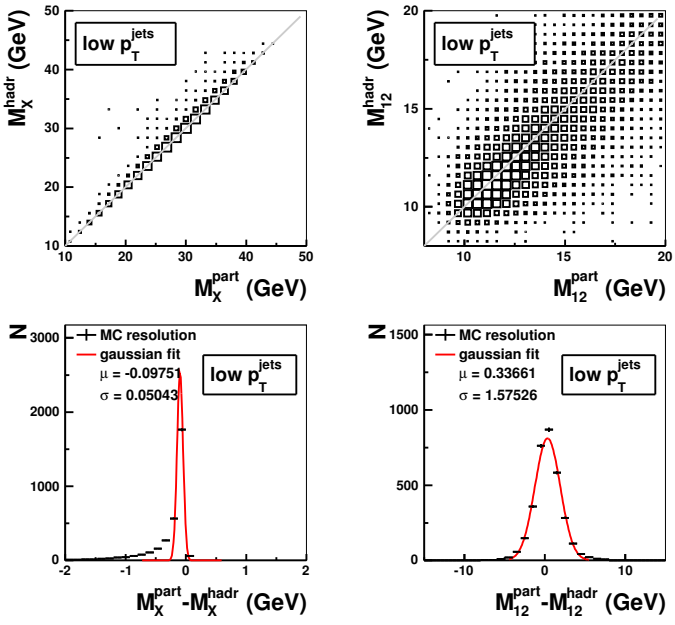

Figure 7.9: Correlation and resolution plots between the **parton** and **hadron** level variables for M_X and M_{12} in sample with $\boldsymbol{low\ p_T^{jets}}$ kinematics.

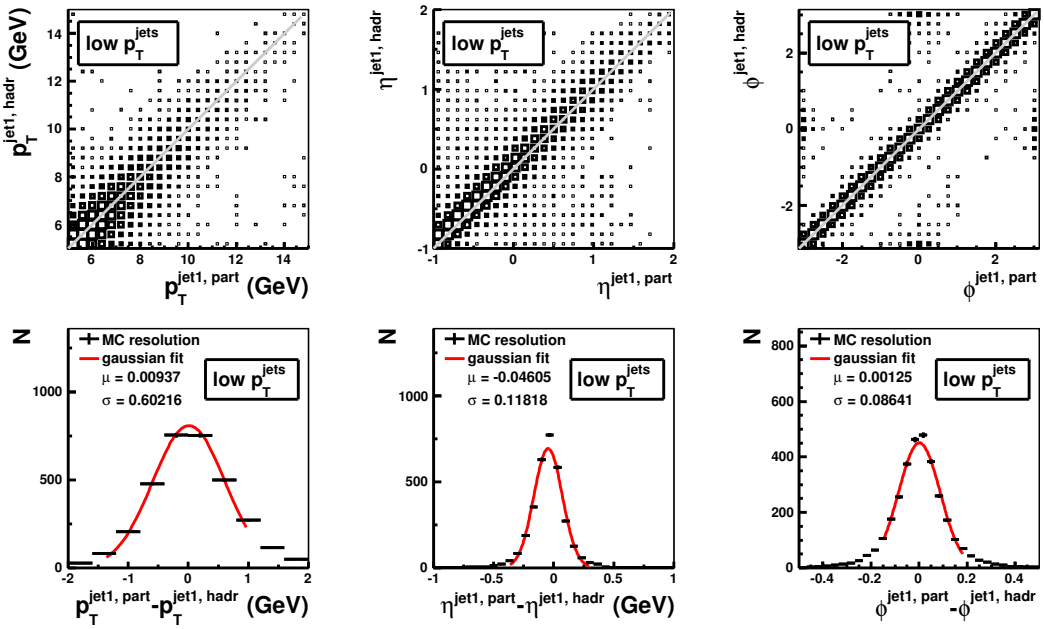

Figure 7.10: Correlation and resolution plots between the **parton** and **hadron** level variables for p_T^{jet1}, η^{jet1} and ϕ^{jet1} in sample with $\boldsymbol{low\ p_T^{jets}}$ kinematics.

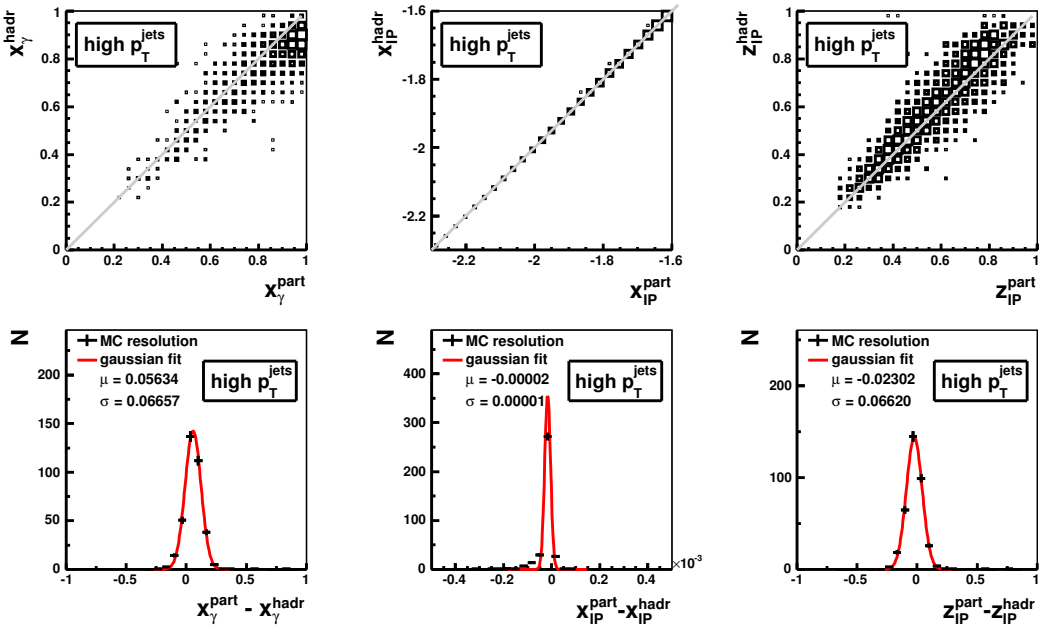

Figure 7.11: Correlation and resolution plots between the **parton** and **hadron** level variables for x_γ and $x_{I\!P}$, $z_{I\!P}$ in sample with $\boldsymbol{high\ p_T^{jets}}$ kinematics.

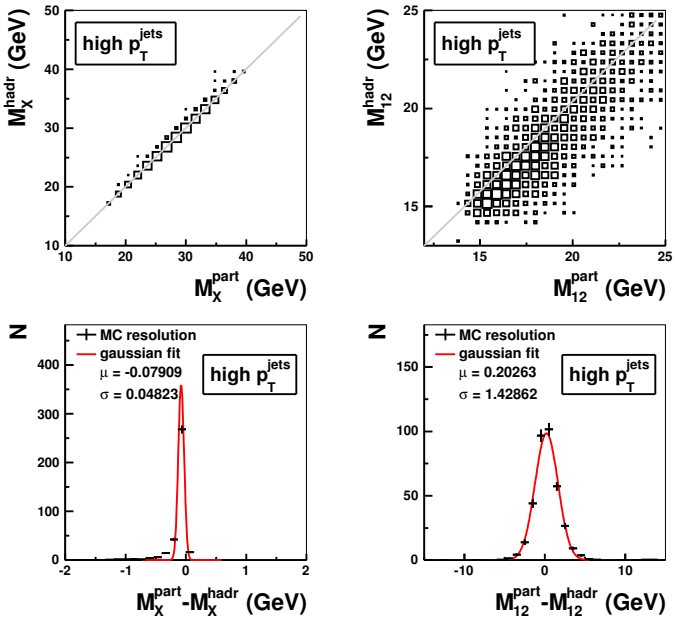

Figure 7.12: Correlation and resolution plots between the **parton** and **hadron** level variables for M_X and M_{12} in sample with ***high*** $\boldsymbol{p_T^{jets}}$ kinematics.

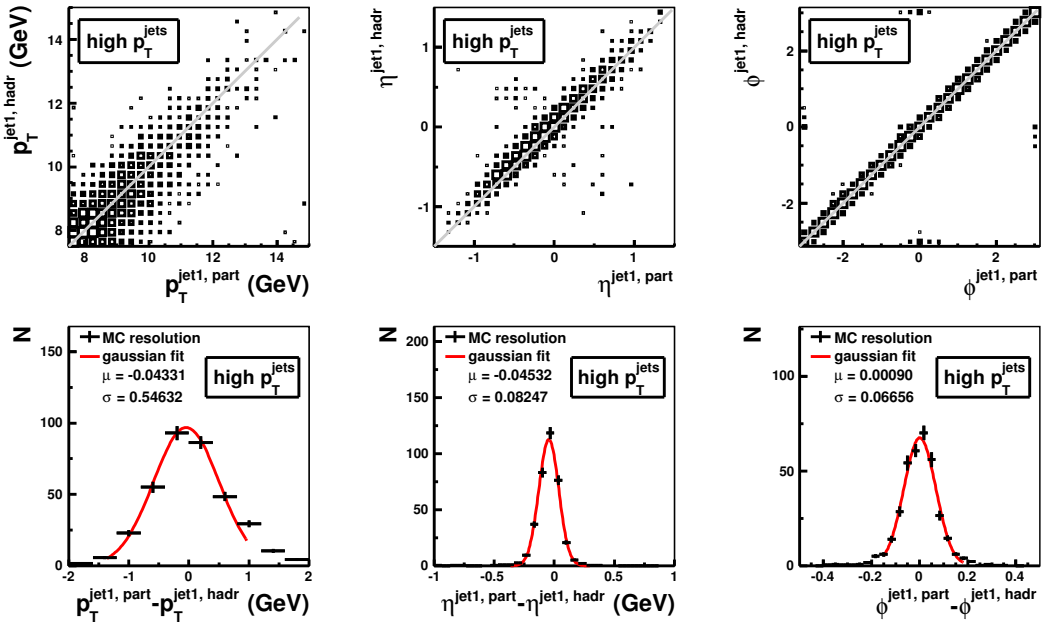

Figure 7.13: Correlation and resolution plots between the **parton** and **hadron** level variables for p_T^{jet1}, η^{jet1} and ϕ^{jet1} in sample with ***high*** $\boldsymbol{p_T^{jets}}$ kinematics.

Chapter 8

Data Selection

In this chapter the selection criteria applied to the the data and MC are described. A non-trivial selection of data taking periods (runs) is introduced. It is elaborated on the electron tagger details. An estimation of the trigger efficiency is made. Detector level distributions of the event variables measured with the data are compared with the Monte Carlo ones. Energy flows and jet profiles at the detector level are presented.

8.1 Run Selection

The H1 HERA data from the 1999 and 2000 positron running period with nominal vertex are analyzed. There are several basic quality ensuring criteria demanded:

- An appropriate high voltage (HV) applied on the sub-detectors mentioned in section 4.2, namely; CJC, CIP, COP, LAr, SpaCal, luminosity system, FMD, PRT, time-of-flight systems.
- The sub-detectors must be properly read out.
- The level of noise must be under control in the detection sub-systems.

The basic run ranges of the data are; $244968 - 261338$ for 1999 $e+$ period and $262144 - 279215$ for the 2000 period. In table 8.1 there is a list shown of runs and run ranges rejected from the basic run selection along with a short explanation of the reason for the rejection, meaning of which will become more clear in the following sections.

The total integrated luminosity of the data sample over the ultimate run selection is ~ 54 pb^{-1}.

8.1.1 Random trigger files

Since the diffractive event selection relies on the large rapidity gap method, it must take regard to the forward detector performance. These may, however,

rejected runs	reason of rejection
246729 – 247590	noise in PRT
247974 – 247978	changed sub-trigger definition
259462 – 262203	min. bias period
262144 – 264200	low eff. of CIP bwd. veto TE
263535 – 263744	noise in PRT
265400 – 265900	noise in PRT
270354 – 270393	small gap in nom. vertex
278691 – 278978	shifted vertex run period
250694, 250696, 250822, 255099 257439, 257441, 270446, 270637 270660, 270661, 270674, 270675 270680, 270682, 270696, 272460 272461, 273170, 273171, 273173 273193, 273330, 273400, 273401 275979	FMD noisy runs

Table 8.1: Summary table of rejected run ranges.

suffer from high noise rates caused either by beam conditions (halo particles, beam-gas interactions) or an electronic noise etc.. Therefore, so called random trigger files are used. The random trigger files contain events which are logged with a constant frequency regardless the trigger decision. The random trigger data share the run numbers with regular data and in this thesis they are studied with use of a selection based on the requirement of no particle candidate with energy above $\sim$ 500 MeV. Such events are mostly free of physics and signals in the sub-detectors are caused by noise or by a non-*ep* background.

8.1.2 PRT noise and run selection

The PRT shows rather high level of noise in some of the run periods which are well identified by H1. These run ranges can be easily identified in figure 8.1 which shows the noise fraction, i.e. number of hits in each of the PRT panel normalized to the number of events in the random trigger run. The last two panels suffer from rather high noise rates most of the time, that is why only the first five layers are used in the analysis. In general, the noise level in PRT is safely below 1%, therefore, it is asked for no activity in the detector for the diffractive events selection, see section 8.4.3.

There is yet another peculiarity concerning the PRT. The hit efficiency in the PRT panels is not adequately simulated, the total PRT tagging efficiency is overestimated by about 40% in simulation - a reweighting is used. Details about the whole procedure can be found in [37]. The reweighting is applied for the simulated MC samples.

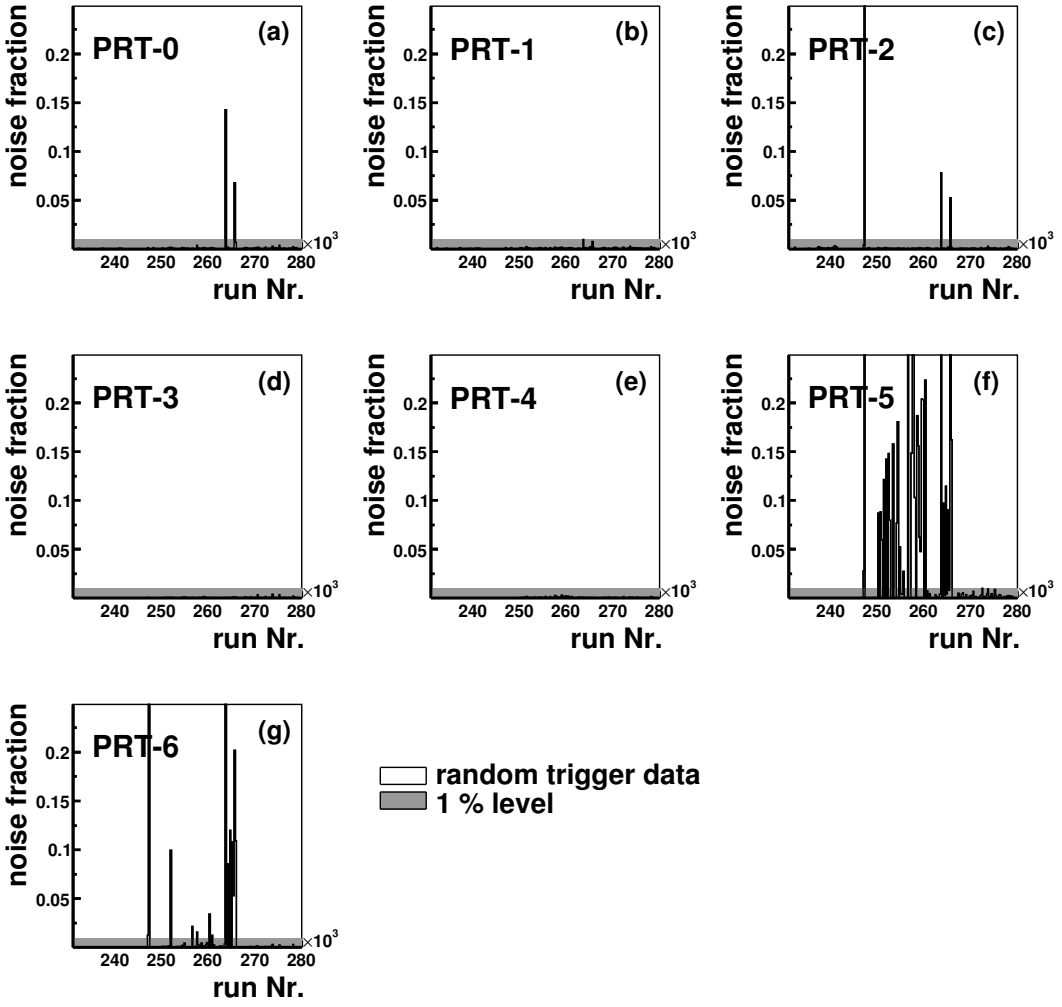

Figure 8.1: Signal in the seven panels of PRT for random trigger events (histogram). Excessively noisy periods are rejected. A one percent level is indicated by a dark band.

8.1.3 FMD noise and run selection

Even after the rejection of runs with the excessive noise fraction in FMD (table 8.1) there is still a residual noise remaining, see figure 8.2. Due to the noise, diffractive events would be rejected by asking for no activity in the FMD, therefore, a non-trivial selection is applied (see section 8.4.3) which allows for the residual noise which is not simulated in MC, but, it is extracted from the random trigger data and added in a layer-wise way to the FMD signal. The third layer of FMD suffers from higher noise which is also taken into account in section 8.4.3.

It may well be that one is not able to identify the noisy run numbers from table 8.1 with noise "spikes" in figure 8.2. This is caused by sort of broader

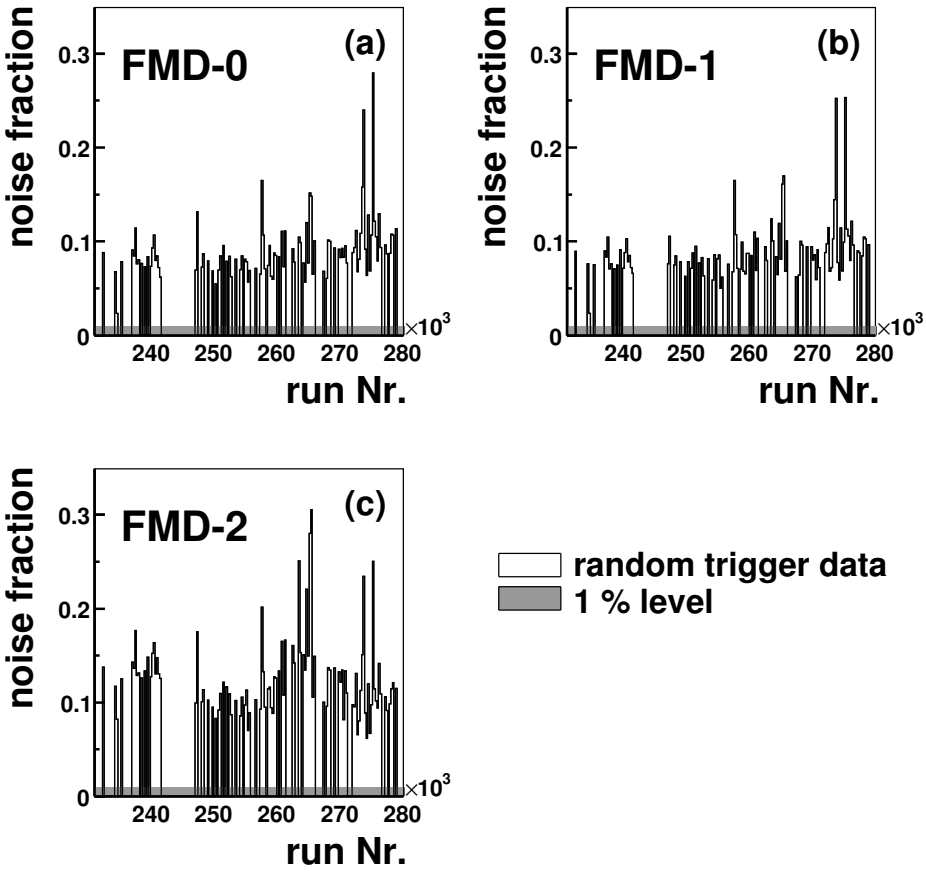

Figure 8.2: Signal in the first three layers of FMD for random trigger events (histogram). Excessively noisy runs are rejected. Residual noise significantly above a one percent level (dark band).

histogram binning in figure 8.2 where the individual noisy runs are averaged over the neighboring runs. The figure 8.2 is rather an illustration supporting the explanation of the residual noise.

8.2 The Electron Tagger Acceptance

The electron tagger (e-tagger) at -33 m from the interaction point is used in this analysis. The following paragraphs describe some specialties about this particular e-tagger which is used for electron tagging in photoproduction events.

The experience shows that the beam parameters may vary significantly from one fill to another. Moreover, even within the same run the currents in some magnet elements around the H1 interaction point may gradually drift, thus, lead to frequent variations of the beam conditions. These variations (influencing the electron trajectories, as well) affect the electron tagger acceptance significantly.

To follow all these changes it would require storing of too much information in a database. Therefore, the electron tagger is not included in the detector simulation. Instead, the acceptance of the e-tagger is calculated separately with dedicated data and MC simulations. The varying conditions are taken into account. Result is a run dependent parameterization of the e-tagger acceptance. As the angle of the scattered electron is limited by design and only the energy is measured, the Q^2 range is restricted to $Q^2 < 0.01$ GeV^2. It is natural to plot the acceptance as a function of scattered electron energy (E'_e or y). For illustration, in figure 8.3 the variations are shown over the year 2000 run ranges of the e-tagger acceptance (A) multiplied by a trigger efficiency ($\varepsilon^{trigg.}$) of the e-tagger and photon detector trigger elements (see section 8.3). The full line is a luminosity weighted average of the acceptance over the run ranges. The acceptance parameterization is determined with precision of 5% in the full y range. Because of the transverse size of 154 × 154 mm of the e-tagger a cut on the x position of the energy cluster from the center of the tagger is applied in this thesis ($|X - X_0| < 6.5$ cm, both for the data explicitly, as well as for MC via the e-tagger acceptance parameterization) in order to avoid a lateral leakage of the electron induced shower. The value of the e-tagger acceptance and trigger efficiency ($A \cdot \varepsilon^{trigg.}$) is applied as an event weight in MC.

Because the simulation of the e-tagger is not provided, the energy in the e-tagger is obtained by means of smearing of the generated scattered electron energy in MC. The energy resolution of the e-tagger is provided as a function of run numbers by means of following formula

$$\frac{\sigma^{etag}}{E_e^{gen}} = \frac{A(run)}{\sqrt{E_e^{gen}}} + 0.01, \tag{8.1}$$

where E_e^{gen} is a true (generated) value of energy of the scattered electron and $A(run)$ is the run dependent parameter with a luminosity averaged value of ~ 0.19 over the selected run range.

Finally, the detector level y is constructed according to formula

$$y \equiv y_e = 1 - \frac{E^{etag}}{E_{elec}^{beam}}, \tag{8.2}$$

where E^{etag} is the energy measured in the e-tagger.

The absolute energy scale uncertainty of the energy measurement is ~ 1.5 %. This uncertainty can be neglected owing to the y range (3.3) and the shape of the acceptance.

There are also other electron taggers (at -8 m and -44 m) which cover different y ranges. They are not used directly in this thesis. Only in the section 8.3.1 the $S82$ sub-trigger is used for monitoring purposes which uses these other electron taggers. Throughout this thesis by writing e-tagger it is referred to the one at -33 m.

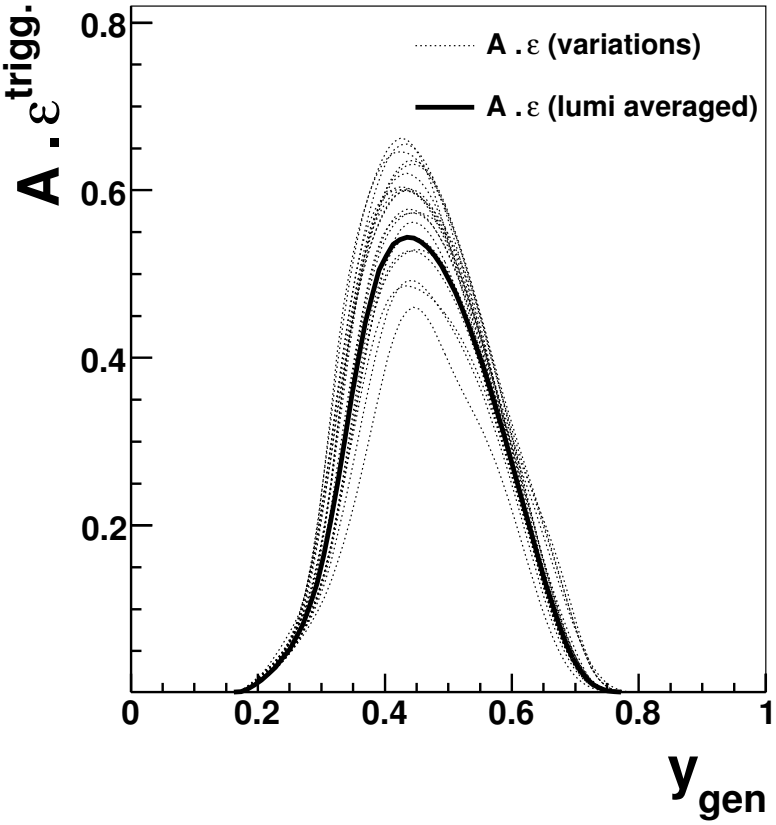

Figure 8.3: Variations of e-tagger acceptance multiplied by trigger efficiency of the tagging system (dotted lines) in the 2000 running period. The luminosity weighted average over the run ranges (full line).

8.3 The S83 Sub-Trigger

The analysis is based on the S83 sub-trigger which combines several trigger elements (TEs). A simplified definition of S83 reads:

```
DCRPh_Tc && (zVtx_sig>1) && (LU_ET && !LU_PD_low) && !CIPB_noSPCLe_T_E1
```

where the explanation of the elements follows:

- `DCRPh_Tc`

  at least three tracks caused by charged particles in the central tracker,

- `zVtx_sig>1`

  a significant peak in z-vertex histogram at L1,

- `LU_ET && !LU_PD_low`

energy above threshold (> 7 GeV) in the e-tagger and low energy in the photon detector (< 6 GeV),

- `!CIPB_noSPCLe_T_E1`

  backward veto TE combining CIP and SpaCal information,

- there are also other trigger elements in the S83 definition dedicated to background rejection.

8.3.1 S83 trigger efficiency

The trigger response is a probabilistic process. A signal event may or may not cause the trigger signal. The data are, therefore, inherently affected by a triggering inefficiency of the sub-trigger. In order to retrieve the correct data rates the efficiency of the sub-trigger must be estimated. This is usually done by means of use of so called monitor sub-triggers (MS) which are independent of the studied sub-trigger. The efficiency $\varepsilon^{trigg.}(S)$ is then measured as fraction of events with positive decision of the studied sub-trigger in the monitor sample, i.e.

$$\varepsilon^{trigg.}(S) = \frac{N(S \,\&\, MS)}{N(MS)}, \tag{8.3}$$

where $N(S \,\&\, MS)$ is the number of events with positive decision of sub-triggers S and MS, $N(MS)$ is the number of events triggered by MS.

There is no independent monitor sub-trigger with sufficient statistics for S83. Therefore, the trigger efficiencies of the individual trigger elements of S83 are studied separately. The procedure of the efficiency estimation follows:

- `LU_ET && !LU_PD_low`

  The efficiency is provided by the e-tagger acceptance parameterization.

- `DCRPh_Tc && zVtx_sig>1`

  These TEs are correlated since they use information about charged particle tracks from the central tracker. Sub-triggers suitable for monitoring of these TEs which would use tagged electrons have, however, small statistics. Instead, inclusive SpaCal electron sub-triggers S0 or S3 are used for monitoring. The efficiency is measured and fitted in a monitor data sample with requirements of two jets at least in the final state of inclusive DIS events. The efficiency is measured by means of formula (8.3) and it is fitted in two dimensions as a function of leading jet transverse momentum (p_T^{jet1}) and a mean pseudorapidity of the jets ($\langle \eta^{jets} \rangle$).

- `!CIPB_noSPCLe_T_E1`

  The backward veto TE is monitored with S82 (LAr and a set of other electron tagger trigger elements). It is sensitive to a backward hadronic activity which can be the case of photon remnant. The efficiency of non-rejection by `CIPB_noSPCLe_T_E1` is measured with use of an event sample which is defined by requirement of two jets at least in the final state in the regime of inclusive tagged photoproduction (the other electron taggers). The efficiency is measured and fitted as a function of x_γ.

- The remaining trigger elements which are not mentioned here (timing and vetoing TEs for background suppression) are supposed to be 100% effective.

The above prescription provides three functions. The `LU_ET && !LU_PD_low` trigger efficiency is given externally and is generally available in H1, it is applied in MC according to section 8.2. The parameterizations of `DCRPh_Tc && zVtx_sig>1` and of `!CIPB_noSPCLe_T_E1` are multiplied in each event according to the event kinematics $p_T^{jet1}, \langle \eta^{jets} \rangle, x_\gamma$. The inverse value of this resulting product is used as an event weight for the data.

For the *low* p_T^{jets} kinematics, in figure 8.4 the `DCRPh_Tc && zVtx_sig>1` trigger efficiency is shown obtained from the monitoring data sample and the parameterization as a function of p_T^{jet1}, $\langle \eta^{jets} \rangle$ and ϕ^{jet1}. Also an error band of 5% uncertainty which covers the deviations of the parameterization from the measured points is indicated. In figure 8.5 the efficiency of the `!CIPB_noSPCLe_T_E1` trigger element is compared for the data and the parameterization as a function of x_γ - no uncertainty band is considered as the parameterization is able to describe the measured efficiency quite well and the 5% uncertainty from the previous case safely covers possible fit imperfections.

For the *high* p_T^{jets} kinematics; in figure 8.6 the `DCRPh_Tc && zVtx_sig>1` trigger efficiency is shown in a similar way to the previous in figure 8.4. On average the efficiency increased as one could have expected from the p_T^{jet1} trigger efficiency dependence in the *low* p_T^{jets} kinematics in figure 8.4. In figure 8.7 is presented the efficiency of the `!CIPB_noSPCLe_T_E1` trigger element. The parameterization is able to describe the measured efficiency rather well except for the first x_γ bin which is of low statistics anyway, caused by the *high* p_T^{jets} kinematical constraints.

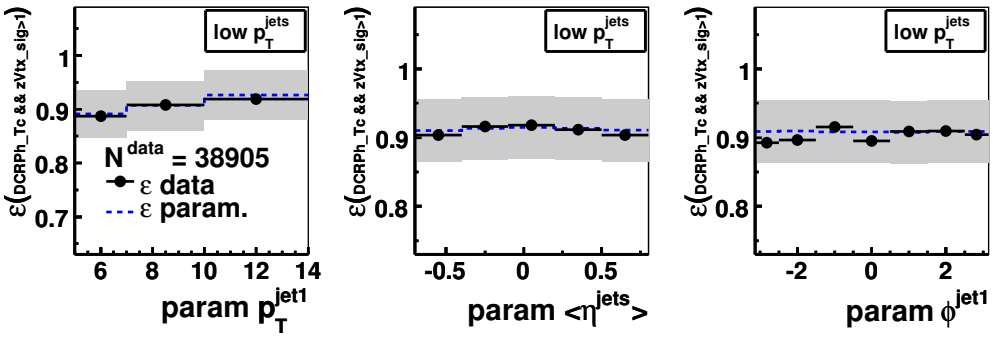

Figure 8.4: *low* p_T^{jets} kinematics; the efficiency of `DCRPh_Tc && zVtx_sig>1` trigger element combination as a function of p_T^{jet1}, $\langle\eta^{jets}\rangle$ and ϕ^{jet1}; measured (dots), parameterization (dashed line), a 5% uncertainty of the fit (band).

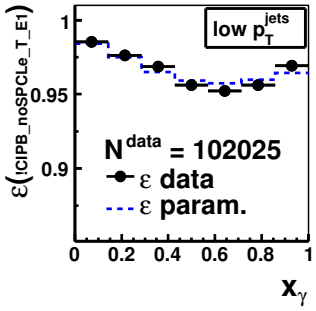

Figure 8.5: *low* p_T^{jets} kinematics; the efficiency of `!CIPB_noSPCLe_T_E1` trigger element as a function of x_γ; measured (dots), parameterization (dashed line).

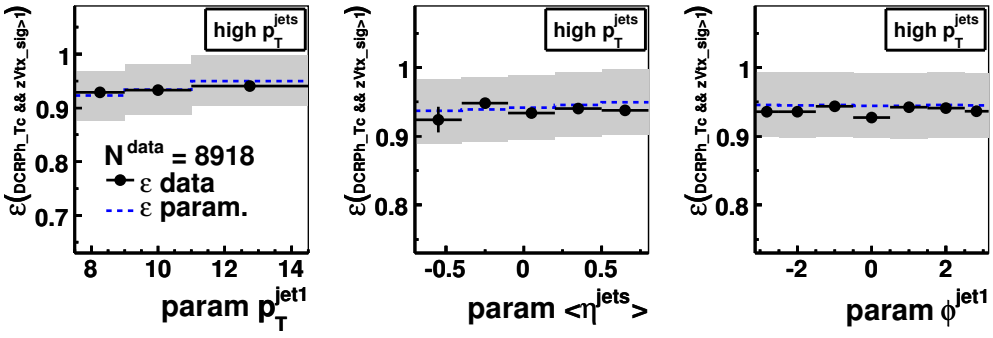

Figure 8.6: *high* p_T^{jets} kinematics; the efficiency of `DCRPh_Tc && zVtx_sig>1` trigger element combination as a function of p_T^{jet1}, $\langle\eta^{jets}\rangle$ and ϕ^{jet1}; measured (dots), parameterization (dashed line), a 5% uncertainty of the fit (band).

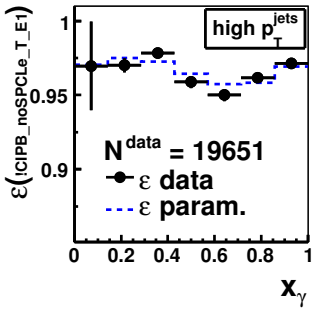

Figure 8.7: *high* p_T^{jets} kinematics; the efficiency of `!CIPB_noSPCLe_T_E1` trigger element as a function of x_γ; measured (dots), parameterization (dashed line).

8.4 Event Selection

In this section an explanation is given of how the events are selected from the data and MC samples. First, an inclusive selection of the events is introduced, after that a diffractive event selection is added.

8.4.1 Inclusive dijet photoproduction

In table 8.2 basic selection criteria and cuts are listed for two jet photoproduction events in the *low* p_T^{jets} and the *high* p_T^{jets} (in brackets) kinematical ranges. No diffractive selection is applied at the moment, that is why it is called the "inclusive" one.

selection	applied to	comment
S83	data	analysis sub-trigger
$Q^2_{gen} < 0.01$ GeV^2	MC	e-tagger acceptance definition range
$0.3 < y_e < 0.65$	data & MC	reasonable e-tagger acceptance
$\lvert X - X_0 \rvert < 6.5$ cm	data	elmg. shower contained in e-tagger
$E_\gamma^{ph.\ det.} < 2$ GeV	data	cut on energy in photon-lumi detector Bremsstrahlung overlap rejection
$p_T^{jet1} > 5$ GeV $p_T^{jet2} > 4$ GeV ($p_T^{jet1} > 7.5$ GeV) ($p_T^{jet2} > 6.5$ GeV)	data & MC	minimum p_T of the jets
$-1 < \eta^{jet1,jet2} < 2$ ($-1.5 < \eta^{jet1,jet2} < 1.5$)	data & MC	pseudorapidity of the jets

Table 8.2: List of inclusive selection criteria applied in data and MC. In brackets are the values for the *high* p_T^{jets} analysis.

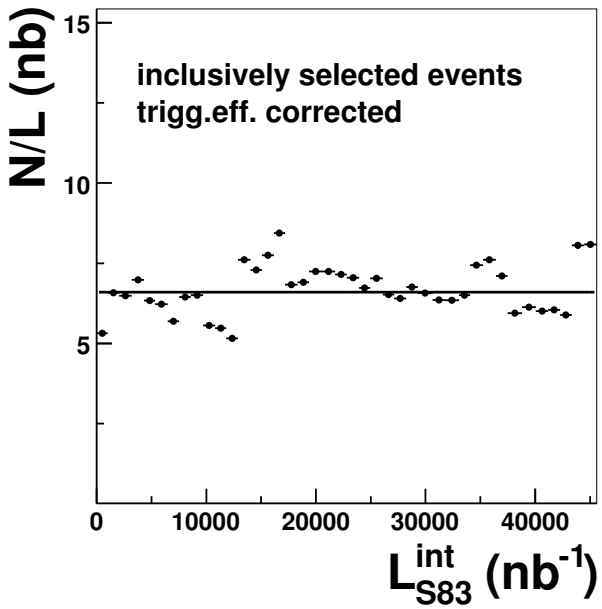

Figure 8.8: The event rate of the inclusive dijet photoproduction sample. Shown is the number of events corrected for S83 trigger efficiency (without e-tagger trigger efficiency) per unit of luminosity.

In figure 8.8 is shown a so called event rate plot. It displays the number of events per a unit of luminosity that pass the inclusive event selection corrected for trigger efficiency (S83 without the e-tagger one) as a function of integrated luminosity. The event rate is not, however, corrected for finite detector acceptance and it is burdened by the varying e-tagger acceptance (see section 8.2), as well, by virtue of which the values are distributed around a constant value of ~ 6.6.

8.4.2 Control plots of inclusive dijet photoproduction

In general, a satisfactory agreement of the data and MC detector level quantities is required. It is not difficult to imagine a that a lacking description of the data by the MC simulations at the detector level must have some consequences, depending on the usage of each particular MC sample - these can be for instance MC samples which are used for; background estimation; correction of the data for the detector effects (correction to the hadron level). It is not exceptional that the agreement is poor at first, which is understandable. In such cases it is a common practice to use reweighting procedures. The aim is merely an additional weighting of events according to the event kinematics in such a way that the MC detector level distributions approach the data distributions.

Since no diffractive selection is applied at this (inclusive) stage, the non-diffractive photoproduction Pythia sample should give a significant contribution

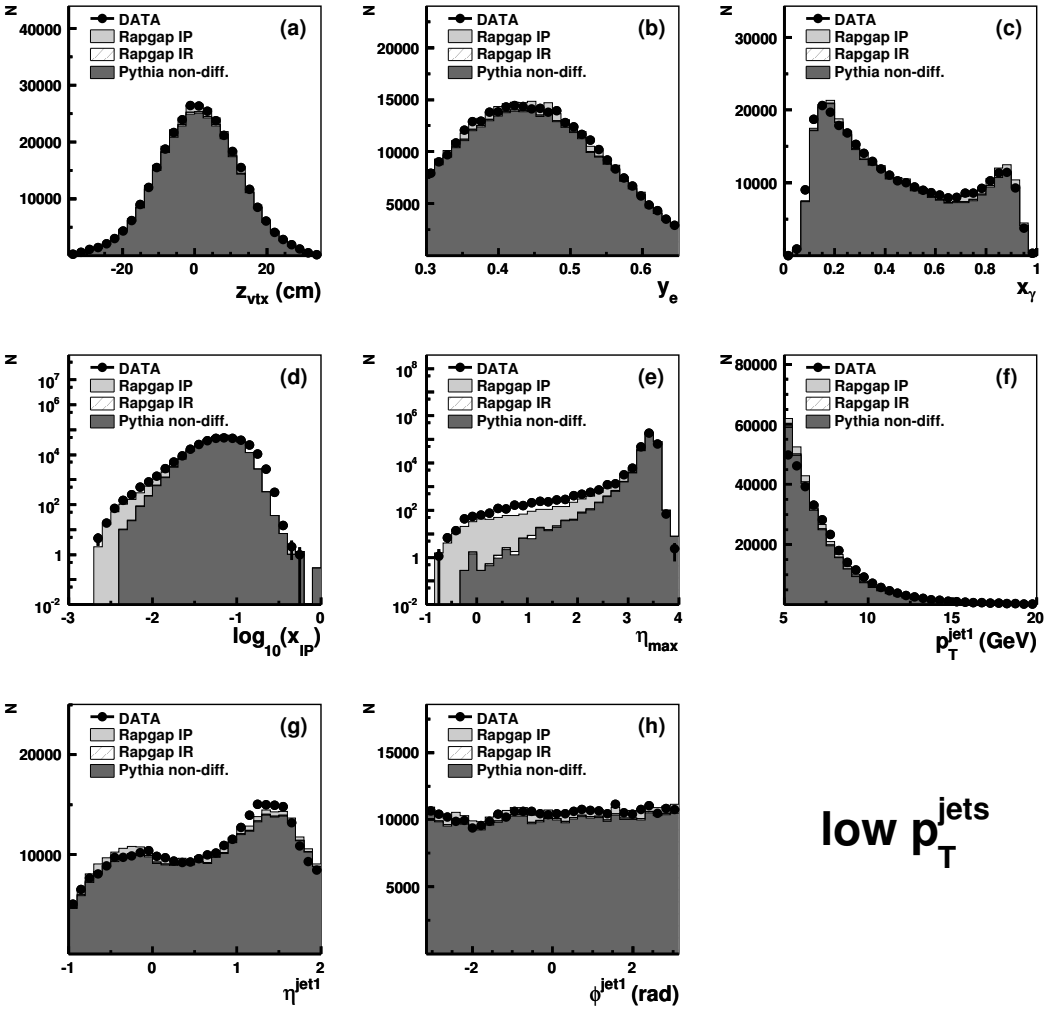

Figure 8.9: Inclusive dijet photoproduction detector level control plots of *low* p_T^{jets} analysis for data (dots), Pythia (dark filled histogram), $I\!P$ exchange Rapgap (light filled histogram) and $I\!R$ exchange Rapgap (hatched histogram) samples. Comparisons are shown for z_{vtx}, y_e, x_γ, $log_{10}(x_{I\!P})$, η_{max}, p_T^{jet1}, η^{jet1} and ϕ^{jet1} in sub-figures (a) - (h), respectively.

if compared with the data. In figure 8.9 the detector level control distributions of the *low* p_T^{jets} analysis for the inclusive event selection and for the basic event variables are shown; z_{vtx} (reconstructed z-coordinate of the vertex), y_e, x_γ, $log_{10}(x_{I\!P})$ (although it is meaningful in diffraction only), η_{max} (the pseudorapidity of the most forward LAr cluster above 400 MeV), p_T^{jet1}, η^{jet1} and ϕ^{jet1}. The control plots compare the data distributions with a sum of Rapgap ($I\!P$ and $I\!R$) and the Pythia sample. Indeed, it is evident that the Pythia MC sample dominates.

The inclusive control plots of the *low* p_T^{jets} analysis in figure 8.9 deserve several comments. The z-coordinate (z_{vtx}) in MC is reweighted in the MC samples in

order to reproduce the shape of the data. A reweighting is also used for the y_e distribution. The reason for these reweightings is in an imperfect distribution of simulated values of z_{vtx} and a slight difference of the shape of the e-tagger acceptance between the parameterization and the data sample. These two variables are independent of the kinematics measured in the central detector, that is why they are reweighted at first. By using the inclusive samples one profits from higher statistics for determination of the reweighting functions. Apart from the slight shape correction of the z_{vtx} and the y_e, there was a more serious x_γ shape disagreement, presumably caused by incorrect settings of multiple interactions (multiparton interactions) [38] in Pythia that occur more likely in the resolved processes due to the non-trivial photon structure. Thus, the Pythia MC sample is reweighted in x_γ. After that, a satisfactory agreement is obtained between the data and the MC samples at the detector level (figure 8.9 (c)). Also a good description is obtained of the $log_{10}(x_{I\!P})$ (figure 8.9 (d)) close to the value of the cut to be applied, cf. (3.7). The tail of low $x_{I\!P}$ values will determine the background fraction in the diffractive sample. In this matter of fact, the x_γ reweighted Pythia sample is fixed as to its normalization in the diffractive analysis (to be introduced). In figure 8.9 (e) the η_{max} distribution nicely illustrates the idea of the large rapidity gap method for the selection of the diffractive events. In figures 8.9 (f), (g) and (h) the jet observables p_T^{jet1}, η^{jet1} and ϕ^{jet1} are shown, respectively. The p_T^{jet1} distribution is not perfectly described, nevertheless, for the purpose of background estimation, the Pythia sample describes the inclusive data rather well. An identical chain of actions is taken to the $high\ p_T^{jets}$ analysis. In figure 8.10 similarly ordered comparisons are shown for this latter kinematic range. The description of the inclusive selected data by the MC is almost perfect.

8.4.3 Diffractive selection

The selection of diffractive events based on the large rapidity gap method employs the cuts on the η_{max} and the $x_{I\!P}$ variables since the diffractive events mostly contribute at a distinct η_{max} range and at low $x_{I\!P}$ values, see figures (d), (e) of 8.9 and 8.10. Therefore, following cuts are applied in the data and MC at the detector level

$$\eta_{max} < 3.2 \quad \text{for both analyses,} \tag{8.4}$$

$$x_{I\!P} < 0.03 \quad \text{for the } low\ p_T^{jets} \text{ analysis,} \tag{8.5}$$

$$x_{I\!P} < 0.025 \quad \text{for the } high\ p_T^{jets} \text{ analysis, inspired by [18].} \tag{8.6}$$

In figure 8.11 detector level control plots of the forward detectors (PRT and FMD) are shown after the cuts (8.4) and (8.5). Shown are the total number of PRT hits and the total number of FMD hit pairs in (a) and (b), respectively. The plots are produced for the $low\ p_T^{jets}$ analysis only, without harm of generality. At a first glance it can be seen that the simulated MC does underestimate the data in

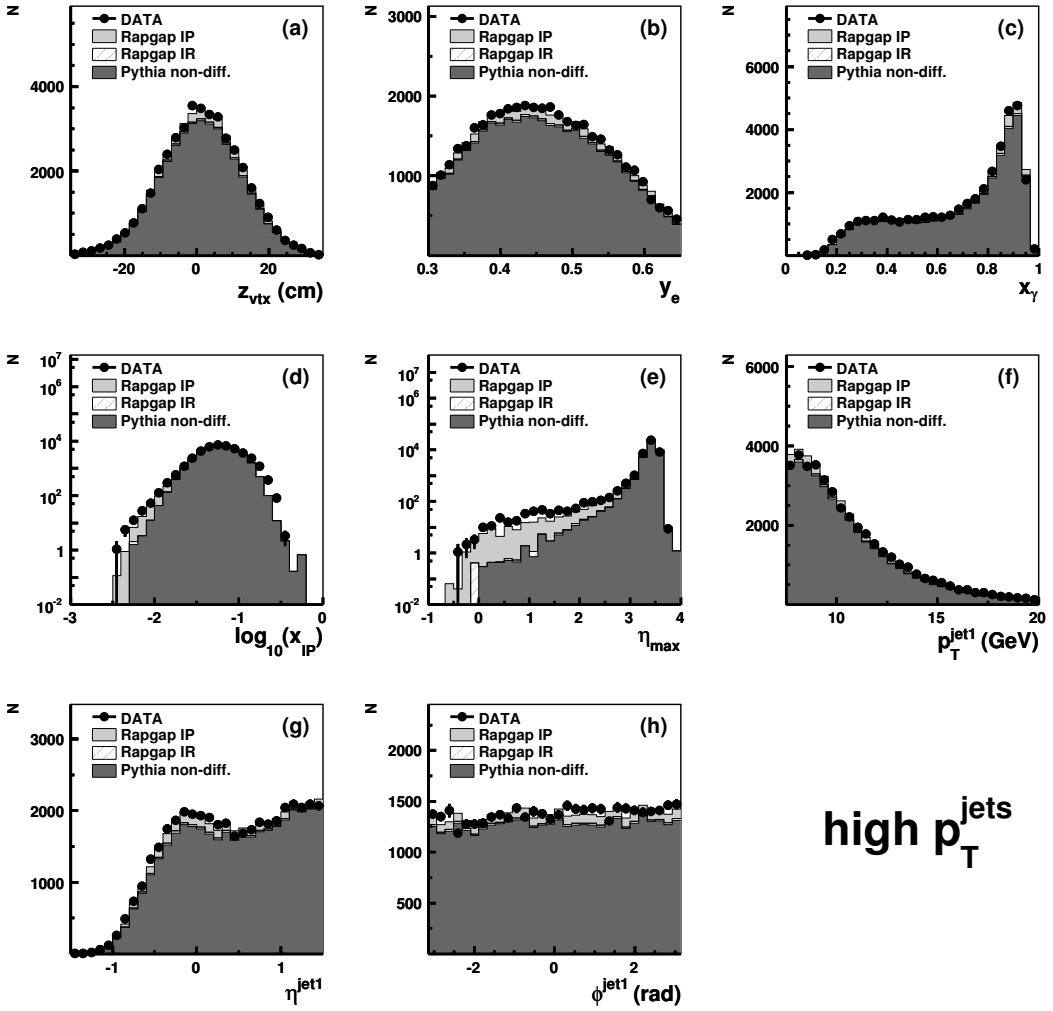

Figure 8.10: Inclusive dijet photoproduction detector level control plots of *high* p_T^{jets} analysis for data (dots), Pythia (dark filled histogram), $I\!P$ exchange Rapgap (light filled histogram) and $I\!R$ exchange Rapgap (hatched histogram) samples. Comparisons are shown for z_{vtx}, y_e, x_γ, $log_{10}(x_{I\!P})$, η_{max}, p_T^{jet1}, η^{jet1} and ϕ^{jet1} in sub-figures (a) - (h), respectively.

these plots. Such a difference can originate both in a fact that the MC contributes only in a LO QCD and in a missing leading proton dissociation contribution - which surely is present in the data. No matter this difference, on can see that a requirement of no activity in the PRT is natural. From the FMD control plot one cannot deduce much as to what would be the best selection, therefore, a cut on the FMD signal is chosen according to previous diffractive analyses made by H1 using the 1999 and 2000 data (for instance [37]) which reads: two hit pairs, at most, allowed in the first three layers of FMD with a possibility of two hit pairs to be in the third layer only (which suffers from higher residual noise rates).

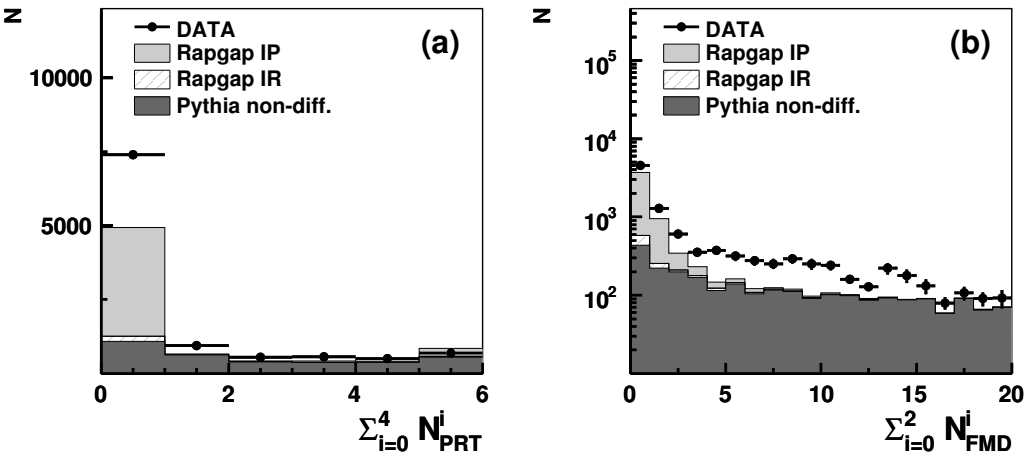

Figure 8.11: The PRT (a) and FMD (b) signals in the inclusive dijet photoproduction sample after the cuts; $\eta_{max} < 3.2$ and $x_{I\!P} < 0.03$ for data (dots), $I\!P$ exchange Rapgap (light filled histogram), $I\!R$ exchange Rapgap (hatched histogram) and Pythia (dark filled histogram). The plots are produced only from the *low* p_T^{jets} data.

Therefore, following PRT and FMD cuts are introduced.

$$\Sigma_{i=1..5} N_i^{PRT} < 1, \quad \Sigma_{i=1..3} N_i^{FMD} < 3 \;\; \&\& \;\; \Sigma_{i=1..2} N_i^{FMD} < 2. \tag{8.7}$$

With all the knowledge gathered, so far, the complete set of cuts for the diffractive dijet photoproduction analysis is summarized in table 8.3. About 4960 and 560 events survive the event selection in the *low* p_T^{jets} and *high* p_T^{jets} analyses, respectively.

8.4.4 Control plots of diffractive *low* p_T^{jets} analysis

In this section the detector level control plots are presented for the diffractive sample in the kinematics of *low* p_T^{jets}. In figure 8.12 (a) - (n) are the shown the comparisons for:

$$z_{vtx}\,, \quad y_e\,, \quad x_\gamma\,, \quad log_{10}(x_{I\!P})\,, \quad \eta_{max}\,, \quad z_{I\!P}\,, \quad p_T^{jet1}\,, \quad \eta^{jet1},$$
$$\phi^{jet1}\,, \quad \langle\eta^{jets}\rangle\,, \quad |\Delta\eta^{jets}|\,, \quad M_{12}\,, \quad M_X\,, \quad \Sigma_{1..3} N_i^{FMD}.$$

Almost a perfect agreement is observed between the data and MC in figure 8.12. The agreement is, however, not so effortless. Another reweighting procedures are applied at this stage to obtain a good description. The contribution of MC in the $z_{I\!P}$ distribution was underestimated in the region of $z_{I\!P}$ about ~ 0.9 (see figure 8.13). Thus, a reweighting was applied, for comparison see figure 8.12 (f) and 8.13. This can be partially due to the fact that the H1 2006

selection	applied to
S83	data
$Q^2_{gen} < 0.01$ GeV^2	MC
$0.3 < y_e < 0.65$	data & MC
$\lvert X - X_0 \rvert < 6.5$ cm	data
$E_\gamma^{ph.\ det.} < 2$ GeV	data
$p_T^{jet1} > 5$ GeV $p_T^{jet2} > 4$ GeV $(p_T^{jet1} > 7.5$ GeV) $(p_T^{jet2} > 6.5$ GeV)	data & MC
$-1 < \eta^{jet1,\,jet2} < 2$ $(-1.5 < \eta^{jet1,\,jet2} < 1.5)$	data & MC
$\eta_{max} < 3.2$	data & MC
$x_{I\!P} < 0.03$ $(x_{I\!P} < 0.025)$	data & MC
$\Sigma_{i=1..5} N_i^{PRT} < 1$	data & MC
$\Sigma_{i=1..3} N_i^{FMD} < 3$ && $\Sigma_{i=1..2} N_i^{FMD} < 2$	data & MC

Table 8.3: The complete selection criteria for diffractive dijet photoproduction analyses. The values in brackets concern the *high* p_T^{jets} analysis.

DPDF Fit B used in the MC generation is valid in the range of $z_{I\!P} \leq 0.8$ only [14] and also because of a large theoretical uncertainty of the DPDF fits at high $z_{I\!P}$.

Another reweighting is applied in the ϕ^{jet1}. There was a period of runs at the end of the 1999 H1 data taking when some broken wires in the central tracker caused a lowered efficiency of measurements. In spite of this problem is known and it is included in the detector simulation, the simulated signal MC samples did not reproduce the problem properly because the simulation of the run numbers (consequently the detector status) omitted, to a large extent, this affected run period. This problem was remedied by reweighting the MC sample as a function of ϕ^{jet1} - not shown here.

After all the reweightings applied there remains a normalization problem if the summed MC samples are compared with the data. This must be caused, again, by the missing proton dissociation contribution and by insufficient cross section predicted by MC at LO QCD. The $I\!P$ and $I\!R$ MC samples are scaled by a factor of 1.3 in the figure 8.12. This multiplicative factor is merely of a cosmetic use in the control plots, it does not affect the procedure of cross section measurement because it cancels during the calculation of acceptance, see section 9.2.1.

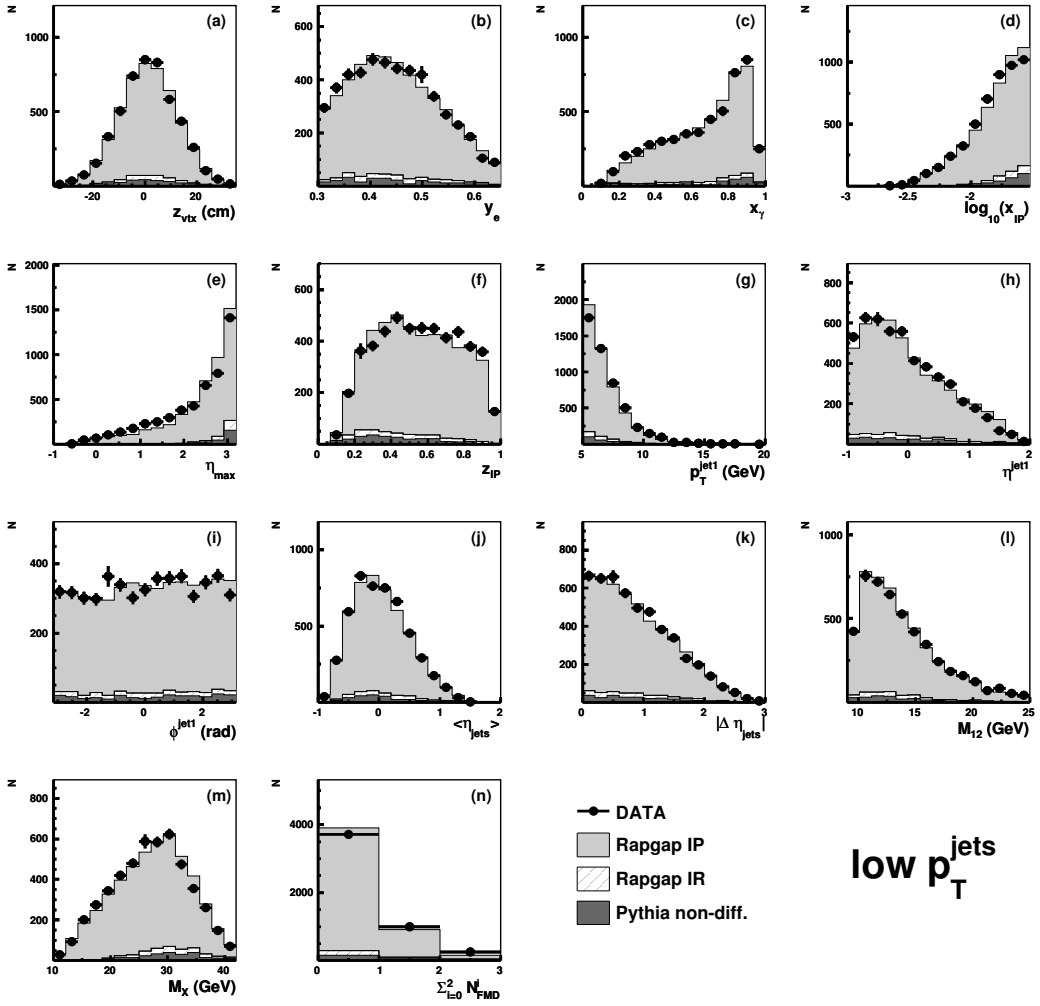

Figure 8.12: Detector level observables in diffractive ***low*** $\boldsymbol{p_T^{jets}}$ analysis; data (dots), $I\!P$ Rapgap (light filled histogram), $I\!R$ Rapgap (hatched histogram) and Pythia (dark filled histogram).

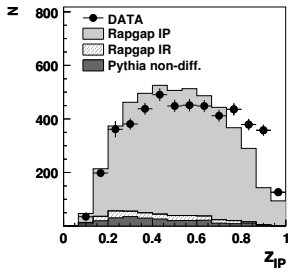

Figure 8.13: Non-reweighted detector level $z_{I\!P}$ distribution in the ***low*** $\boldsymbol{p_T^{jets}}$ analysis; data (dots), $I\!P$ Rapgap (light filled histogram), $I\!R$ Rapgap (hatched histogram) and Pythia (dark filled histogram).

Jet profiles and energy flow in the *low* p_T^{jets} analysis

Another check of a proper simulation of the detector response is a study of energy flows. Either a global energy flow or energy flows around the jets (so called jet profiles) can be studied.

Jet Profiles: One can study how well the energy flow in data is described by MC around the jets. Provided a quantity $p_T^2/d\eta d\phi$ represents a density distribution of transverse momentum of the final state particles in the $\eta - \phi$ plane one can construct the jet profiles as follows

$$\frac{dp_T}{d\eta} = \int \frac{dp_T^2}{d\eta d\phi} d\phi \quad \text{or} \quad \frac{dp_T}{d\phi} = \int \frac{dp_T^2}{d\eta d\phi} d\eta. \tag{8.8}$$

The integration limits are usually set to $|\eta - \eta_0| < 1$ and $|\phi - \phi_0| < \frac{\pi}{2}$, where η_0 and ϕ_0 are the pseudorapidity and azimuthal angle of the jet, respectively. By means of using the full statistics one can make an average of the jet profiles, for example $1/N \cdot dp_T/d\eta$. It tells us what is the average transverse energy flow around the jet axis in data and it can be compared with the simulation. In figure 8.14 the η and ϕ jet profiles (obtained from the Hadroo2 particle candidates, see section 7.2) are compared for the diffractively selected data and simulated MC samples (Rapgap and Pythia samples summed proportionally to their generated cross sections) for forward and backward jet - ordered according to pseudorapidities of the two hardest jets. The jet profiles in data are well described by the MC.

Energy Flow of Particle candidates: In figure 8.15 averaged energy flows of the Hadroo2 particle candidates are shown for the diffractive events as a function of ϕ and θ. The energy flows for the data are compared with MC. The MC simulations provide a satisfactory description of the visible energy flow.

8.4.5 Control plots of diffractive *high* p_T^{jets} analysis

In figure 8.16 (a) - (n) are shown the comparisons for the variables mentioned in section 8.4.4 for the case of the *high* p_T^{jets} kinematics. Within the large statistical errors the agreement between the data and MC is satisfactory. The bad description of $z_{I\!P}$ (see figure 8.17) and ϕ^{jet1} are remedied by means of reweightings. Finally, the $I\!P$ and $I\!R$ MC samples are scaled by a factor of 1.4 in the figure 8.16.

Jet profiles and energy flow in the *high* p_T^{jets} analysis

In figure 8.18 the jet profiles for the *high* p_T^{jets} analysis are presented. The jet profiles in the data are well described by the MC. The energy flows of the Hadroo2 particle candidates as a function of ϕ and θ can be found in figure 8.19. Given the statistical fluctuations the energy flows in the data are satisfactorily described by the MC.

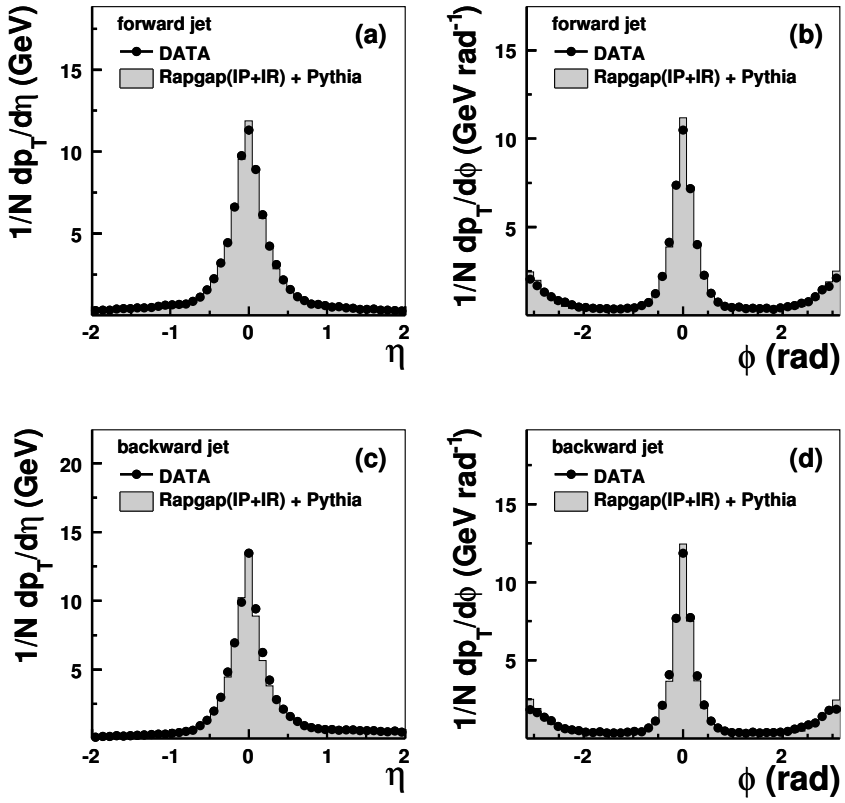

Figure 8.14: Averaged jet p_T profiles for the ***low*** $\boldsymbol{p_T^{jets}}$ analysis; data (dots), Rapgap($I\!P + I\!R$) + Pythia (filled histogram). The η and ϕ profile for forward jets in (a) and (b), respectively. The η and ϕ profile for backward jets jet in (c) and (d), respectively. Forward and backward jet distinction is based on the η of the jets.

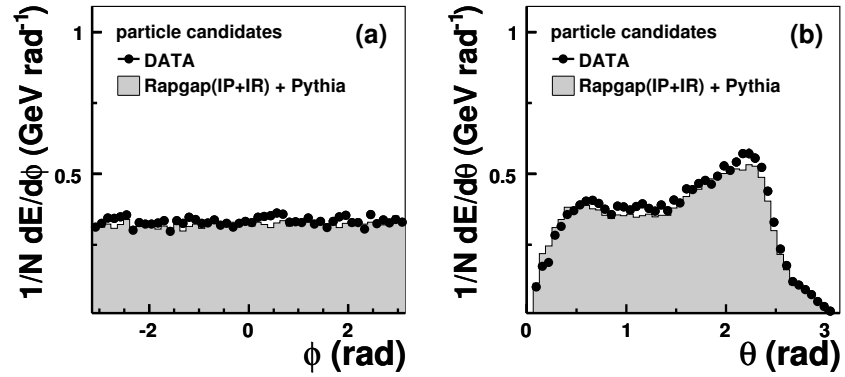

Figure 8.15: Averaged energy flows of the particle candidates for the ***low*** $\boldsymbol{p_T^{jets}}$ analysis; data (dots), Rapgap($I\!P + I\!R$) + Pythia (filled histogram). In (a) and (b) the energy flow as a function if ϕ and θ of the candidates, respectively.

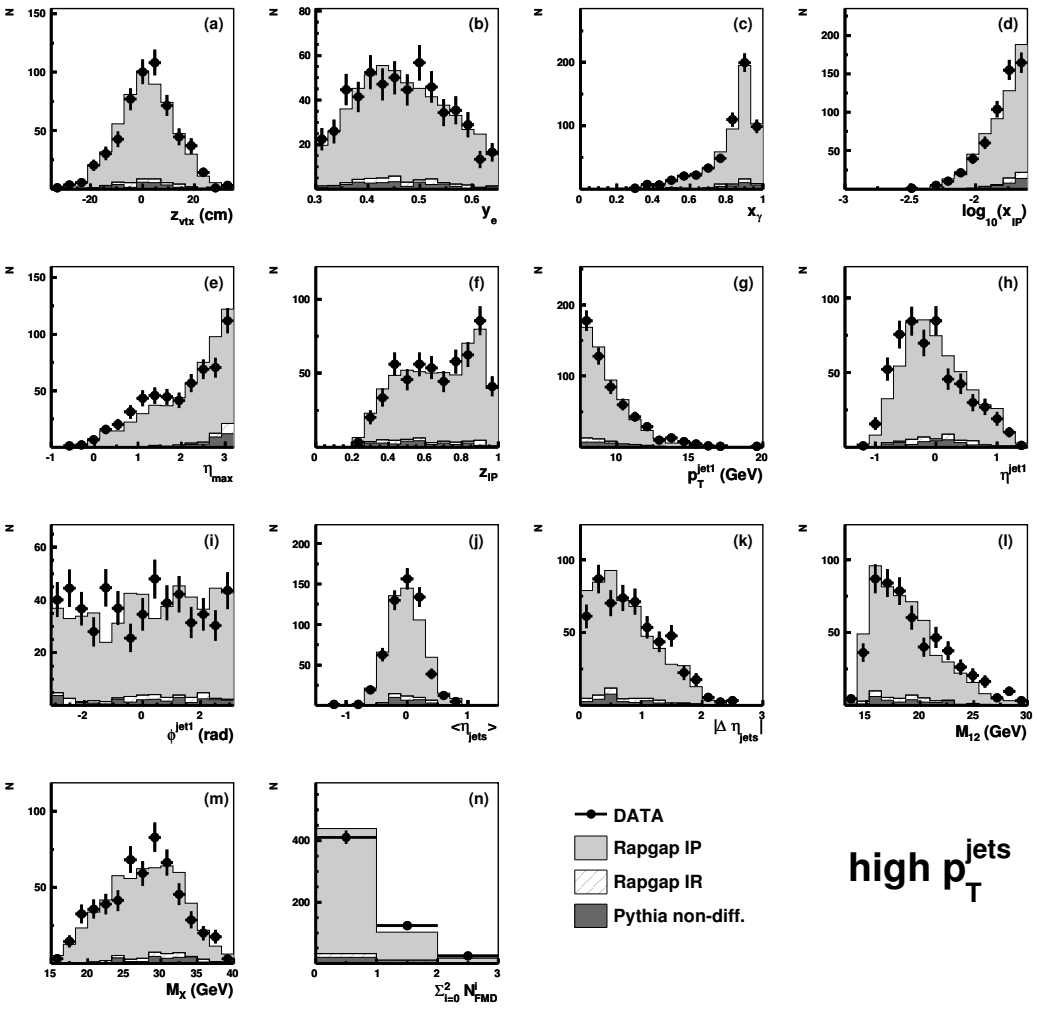

Figure 8.16: Detector level observables in diffractive ***high*** $\boldsymbol{p_T^{jets}}$ analysis; data (dots), $I\!P$ Rapgap (light filled histogram), $I\!R$ Rapgap (hatched histogram) and Pythia (dark filled histogram).

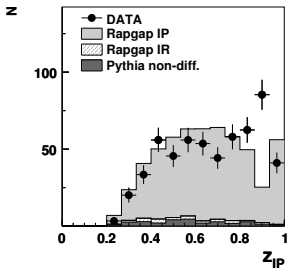

Figure 8.17: Non-reweighted detector level $z_{I\!P}$ distribution in the ***high*** $\boldsymbol{p_T^{jets}}$ analysis; data (dots), $I\!P$ Rapgap (light filled histogram), $I\!R$ Rapgap (hatched histogram) and Pythia (dark filled histogram).

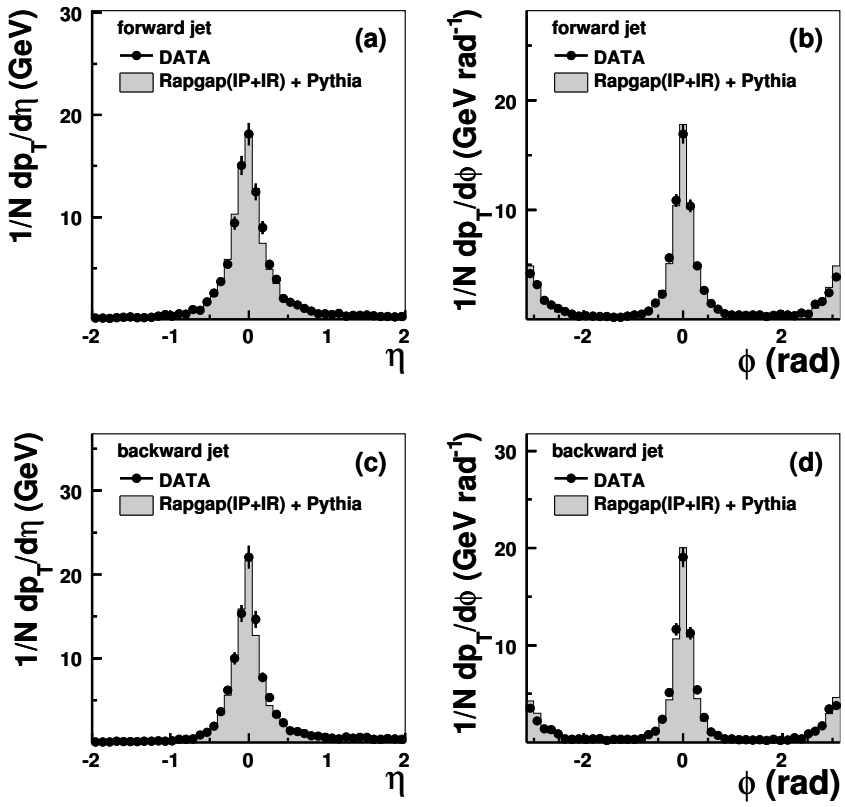

Figure 8.18: Averaged jet p_T profiles for the ***high*** $\boldsymbol{p_T^{jets}}$ analysis; data (dots), Rapgap($I\!P + I\!R$) + Pythia (filled histogram). The η and ϕ profile for forward jets in (a) and (b), respectively. The η and ϕ profile for backward jets jet in (c) and (d), respectively. Forward and backward jet distinction is based on the η of the jets.

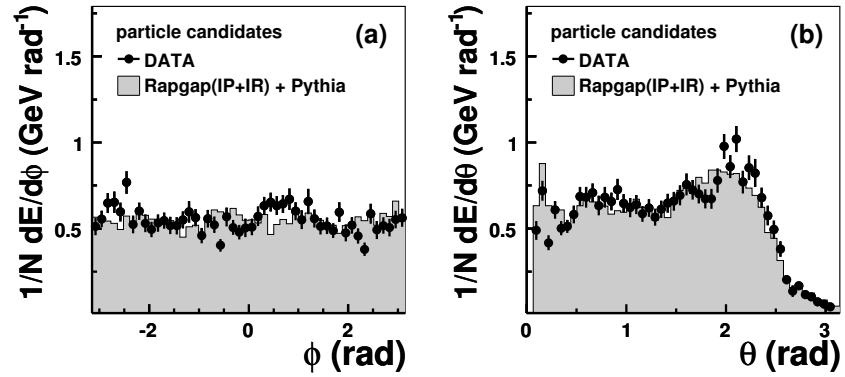

Figure 8.19: Averaged energy flows of the particle candidates for the ***high*** $\boldsymbol{p_T^{jets}}$ analysis; data (dots), Rapgap($I\!P + I\!R$) + Pythia (filled histogram). In (a) and (b) the energy flow as a function if ϕ and θ of the candidates, respectively.

Chapter 9

Cross Section Measurement

The measured data are to be corrected for all the detector effects in order to make them available at the level of stable hadrons. Before doing so, an issue of a choice of a suitable binning must be solved. Also it must be coped with a proton dissociation contribution. Last but not least, an estimation of systematic uncertainties must be done.

9.1 Formula for the Cross Section Measurement

The differential cross sections are measured according to the following formula

$$\left(\frac{d\sigma}{dx}\right)_i = \frac{N_i^{data} - N_i^{MC,bgd.}}{A_i \cdot \varepsilon_i^{trigg.} \cdot \Delta_i^x} \cdot \frac{1}{\mathcal{L}} \cdot C^{p.diss.}. \tag{9.1}$$

The meaning of the quantities in (9.1) is as follows: N_i^{data} is the number of detected events, $N_i^{MC,bgd.}$ is the background fraction obtained from Monte Carlo simulation, A_i is the correction factor to the level of stable hadrons calculated from MC in section 9.2.1, $\varepsilon_i^{trigg.}$ is the trigger efficiency, Δ_i^x is the bin width, $\mathcal{L}$ is the luminosity of the data and finally $C^{p.diss.}$, obtained from MC, accounts for the correction into the range of t and M_Y introduced in (3.8) and (3.9), respectively.

The product of $A_i \cdot \varepsilon_i^{trigg.}$, actually, comprises several effects. The correction factor A (so called acceptance or better smeared acceptance) includes the net geometrical acceptance and smearing but also encompasses the acceptance and trigger efficiency of the e-tagger. The $\varepsilon_i^{trigg.}$ by itself merely accounts on the trigger efficiency of `DCRPh_Tc && zVtx_sig>1 && !CIPB_noSPCLe_T_E1` (studied in section 8.3).

9.2 Choice of Binning

The differential cross sections are measured cumulatively in bins of each variable we are interested in. A so called bin-to-bin correction method is used in this thesis to correct the measured cross sections to the level of stable hadrons. This method requires a good description of the detector level of the data by the MC, as well as, a good correspondence between the hadron and simulated detector level of the MC (see sections 8.4.4, 8.4.5 and also 7.5). Correction factors are calculated for each bin of the measurement. The choice of the binning has to fulfill certain quality requirements, however. One can define following subsets of events. Each event of the analysis belongs to one of the following subsets;

- **H** (hadron): events that are constrained by the hadron level kinematical constraints but do not necessarily have to pass the detector level cuts (cf. table 8.3),
- **D** (detector): events that pass the detector level cuts regardless range of kinematics at the hadron level,
- **B** (both): events that pass both the hadron level and the detector level constraints.

9.2.1 Purity, stability and acceptance of bins

Provided the division of the MC sample into the above classes one can calculate so called bin purity, **P**. It is defined as a fraction of events that pass both hadron and detector level cuts and are reconstructed and generated in the same bin (i) to the number of events reconstructed in that bin no matter where they are generated, i.e.

$$P_i = \frac{N^B(det\ i = had\ i)}{N^D(det\ i)}, \tag{9.2}$$

the meaning is obvious, it tells us how "pure" the detector level bin is - what the true fraction of events generated in the same bin is.

Similarly a so called bin stability, **S**, can be defined. It tells us what the fraction of events is that stay in the same bin in which they were generated, after imposing the detector level cuts on top, i.e.

$$S_i = \frac{N^B(det\ i = had\ i)}{N^H(had\ i)}. \tag{9.3}$$

It is clear that the smaller values of bin purities and stabilities the less reliable is the content as to its origin. If there are large migrations from one bin to another caused by transitions between the hadron and detector level, one can expect lower purities and stabilities. It is desirable to ensure some minimal quality of the bins

by means of requirements on the purity and stability. This usually means a choice of bins that are wide enough in order to cover the hadron to detector level smearing.

Having defined the terms of purity, stability and smearing one can introduce the acceptance, A. What is meant by acceptance in following is not only the geometrical acceptance. The definition of A accounts on the effects of smearing too, caused by reconstruction of the kinematics at the detector level. The acceptance is often called also a smeared acceptance is calculated as follows

$$A_i = \frac{N^D(det\ i)}{N^H(had\ i)}. \tag{9.4}$$

The meaning of (9.4) is very straightforward. It is the ratio of detector level entries in a particular bin (irrespectively where it they are generated) to the number of events generated in that bin (no matter where it is reconstructed). By multiplying the measured (no background and trigger inefficiency corrected) data by $1/A$ one performs the correction of the data to the level of hadrons, often called a bin-to-bin unfolding.

In figure 9.1 the acceptances, purities and stabilities are shown for the analysis in *low* p_T^{jets} kinematics for the following event variables

$$\begin{array}{ccc} x_\gamma & log_{10}(x_{I\!P})\,, & z_{I\!P}, \\ p_T^{jet1}\,, & \langle\eta^{jets}\rangle\,, & |\Delta\eta^{jets}|, \\ M_{12}\,, & M_X\,, & W. \end{array}$$

For the variables x_γ, $\langle\eta^{jets}\rangle$, $|\Delta\eta^{jets}|$ and M_X the P and S are always above 60%. In the other variables the P and S are above 50% except for last bins in $log_{10}(x_{I\!P})$, $z_{I\!P}$ and p_T^{jet1}. The acceptance A may seem low. This is due to the fact that the detector level quantities are influenced by the electron tagger acceptance (multiplied by trigger efficiency) which is on average of order of $\sim 50\%$ in the y range of the analysis.

In figure 9.2 the acceptances, purities and stabilities are shown for the analysis in *high* p_T^{jets} kinematics for the event variables. Neglecting the bins with low statistical significance it can be seen that the P and S are above 60% for $log_{10}(x_{I\!P})$, $\langle\eta^{jets}\rangle$, $|\Delta\eta^{jets}|$ and W. The other variables are usually above and around 50% of P and S except for the stability in all bins of p_T^{jet1} and the last bin of purity of p_T^{jet1}. This is, nevertheless, sort of typical for diffractive analyses in H1 (see [3]). In this matter of fact, the values of purities and stabilities of the bins are satisfactory.

At this stage, the bin boundaries can be reckoned as fixed. The binning was already anticipated in the figures 6.3, 6.4 and 8.4, 8.6.

There is one remark to the calculation of the acceptances etc.. Often pre-selections of MC samples are used in order to reduce the volume of the data to process. One has to be careful applying such pre-selections and make sure that

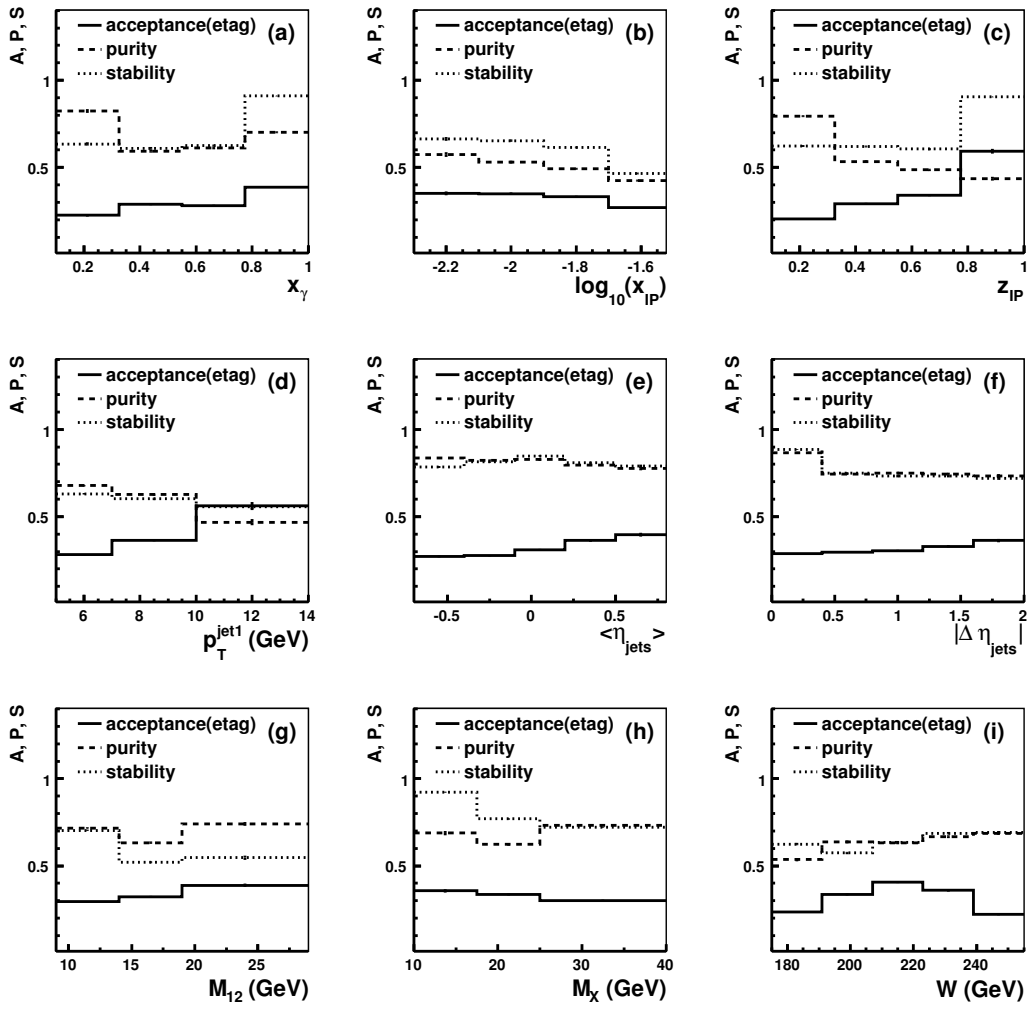

Figure 9.1: The bin quality observables for the *low* p_T^{jets} analysis; acceptance (full line), purity (dashed line), stability (dotted line).

no events, contributing to the calculations of the bin quantities of A, P nd S, are thrown away. Otherwise the calculation of especially the acceptance, A, would be artificially biased and wrong.

9.3 Correction for Proton Dissociation

Sort of historical cuts of (3.8) and (3.9) are used which arise from detection efficiency of the H1 forward detectors (PRT and FMD) for the leading proton elastic (EL) or dissociative (PD) events. The treatment of correction of the proton dissociation contribution is inspired by [39]. Here a modified procedure is used.

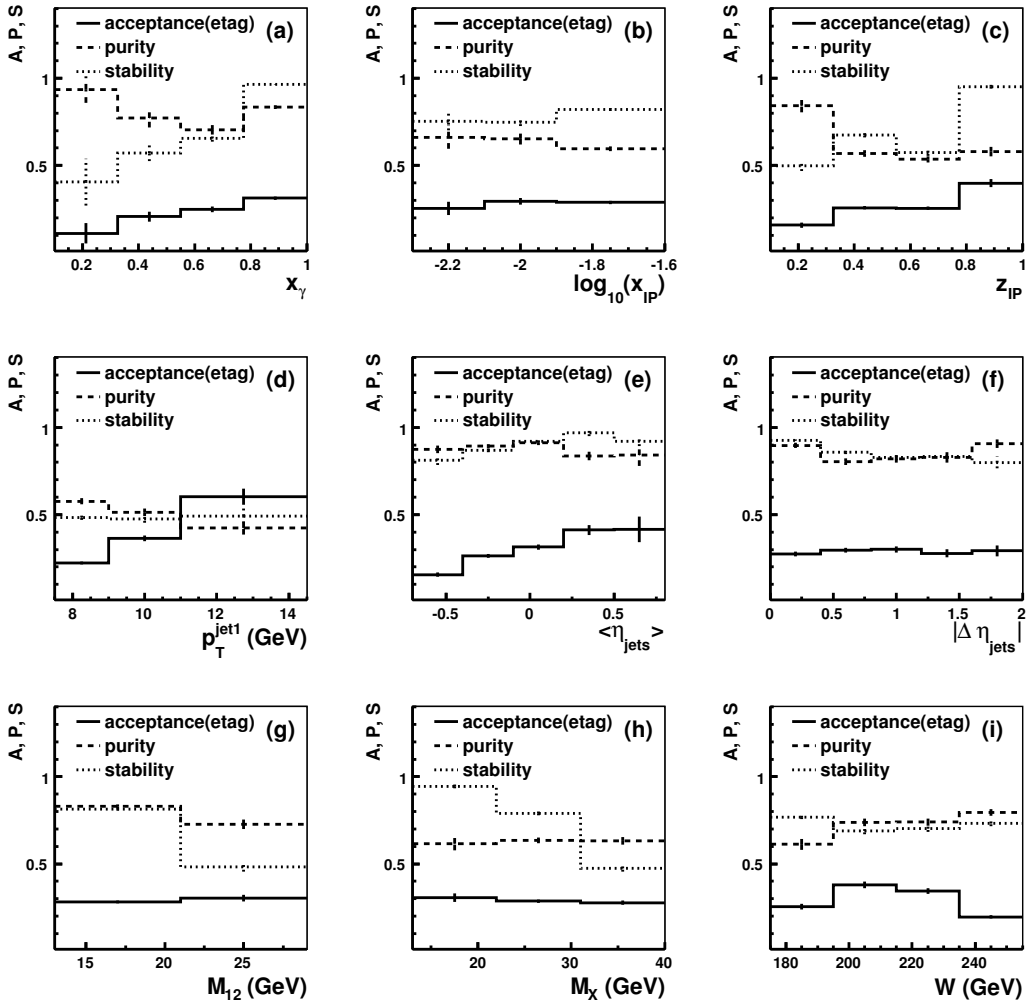

Figure 9.2: The bin quality observables for the *high* p_T^{jets} analysis; acceptance (full line), purity (dashed line), stability (dotted line).

In section 6.1.3 the MC samples used for proton dissociation study are introduced. There are two simulated MC samples used of $J/\psi \rightarrow e^+e^-$ photoproduction events with proton dissociation switched on and off. In figure 9.3 the control plots of invariant mass of the two lepton tracks and the angle of the whole final state, θ^{HFS}, are displayed (made from the EL J/ψ MC sample). A selection of $2.8 < m^{inv} < 3.3$ GeV and $-1.5 < \eta^{HFS} < 0$ (which correspond to $1.57 < \theta^{HFS} < 2.7$ rad) is applied in order to ensure a good reconstruction of J/ψ constrained into a backward region of the H1 detector so that the exclusive final state does not interfere with the forward cuts on η^{max}, PRT and FMD.

In figure 9.4 the detection efficiencies are shown for the PD and EL samples as functions of M_Y and $|t|$. The efficiencies are defined as a number of events that is rejected by the forward cuts (LAr: $\eta_{max} < 3.2$, FMD and PRT or any of

them: ANY) divided by the total number of events in each bin. For the value of M_Y at 1.6 GeV the PD events are detected with a good efficiency of $\sim 70\%$ if all the forward cuts are employed, figure 9.4 (a). For the value of $|t|$ at 1 GeV^2 the PD events are detected with an efficiency of $\sim 90\%$, figure 9.4 (b). The EL events suffer from a rejection too. At the $|t|$ value of 1 GeV^2 the rejection amounts roughly 40%, figure 9.4 (c), which seems on one hand too much, on the other hand, the $|t|$ spectrum falls rapidly as $|t|$ increases.

The correction factor accounting on the proton dissociation migration across the M_Y and $|t|$ cuts is calculated by means of using the above J/ψ samples as follows

$$C_{pdis} = \frac{N^{had}(kin\ OK)}{N^{det}(kin\ any,\ cuts\ OK)}\ , \tag{9.5}$$

where $N^{had}(kin\ OK)$ are the events generated in kinematics constrained to $M_Y <$ 1.6 GeV and $|t| < 1$ GeV^2 and $N^{det}(kin\ any,\ cuts\ OK)$ are the events that pass the η^{max}, PRT and FMD cuts, but generated with unconstrained kinematics. This formula is, actually, similar to the calculation of the acceptances (A) in section 9.2.1.

There is a mixture of EL and PD events in the measurement therefore the formula must be rewritten

$$C_{pdis} = \frac{N^{EL,had}(kin\ OK) + R \cdot N^{PD,had}(kin\ OK)}{N^{EL,det}(kin\ any,\ cuts\ OK) + R \cdot N^{PD,rec}(kin\ any, cuts\ OK)}. \tag{9.6}$$

Where R is the ratio of number of EL events to the number of PD events. However, the above formula is not precisely what is needed. One has to keep in mind that during the calculation of the bin acceptances, A, the $|t|$ cut is employed already. Hence, $N^{EL,det}(kin\ any,\ cuts\ OK)$ must be replaced by $N^{EL,det}(kin\ OK,\ cuts\ OK)$ in order not to double correct the EL events. The ultimate formula reads

$$C_{pdis} = \frac{N^{EL,had}(kin\ OK) + R \cdot N^{PD,had}(kin\ OK)}{N^{EL,det}(kin\ OK,\ cuts\ OK) + R \cdot N^{PD,rec}(kin\ any, cuts\ OK)}. \tag{9.7}$$

With an assumption of the ratio $R = N(EL)/N(PD) = 1$ (in the $M_Y <$ 1.6 GeV and $|t| < 1$ GeV^2 range) the correction factor reads

$$C_{pdis} = 1.06 \pm 7\%(syst.), \tag{9.8}$$

where the systematic uncertainty of 7% is determined from variations of the ratio $R = 1/2$ and $R = 2$. Within the error the value of C_{pdis} is consistent with other diffractive analyses in H1.

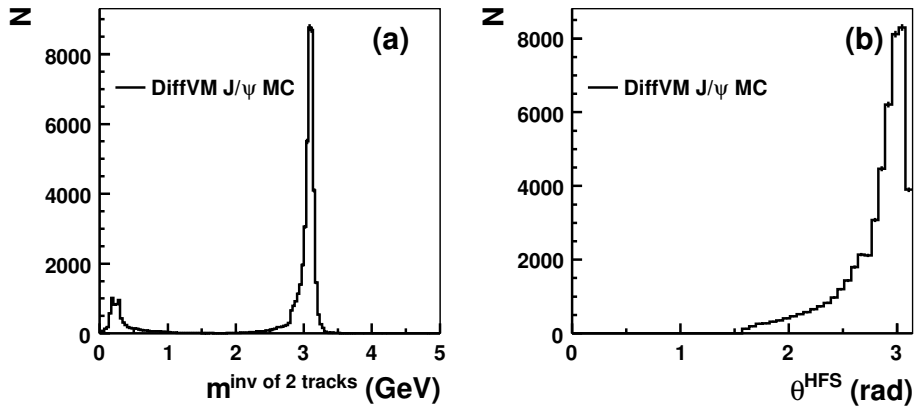

Figure 9.3: The invariant mass distribution of the two tracks in DIFFVM MC $J/\psi \rightarrow e^+e^-$ sample, (a). In (b) the distribution of θ angle of the final state.

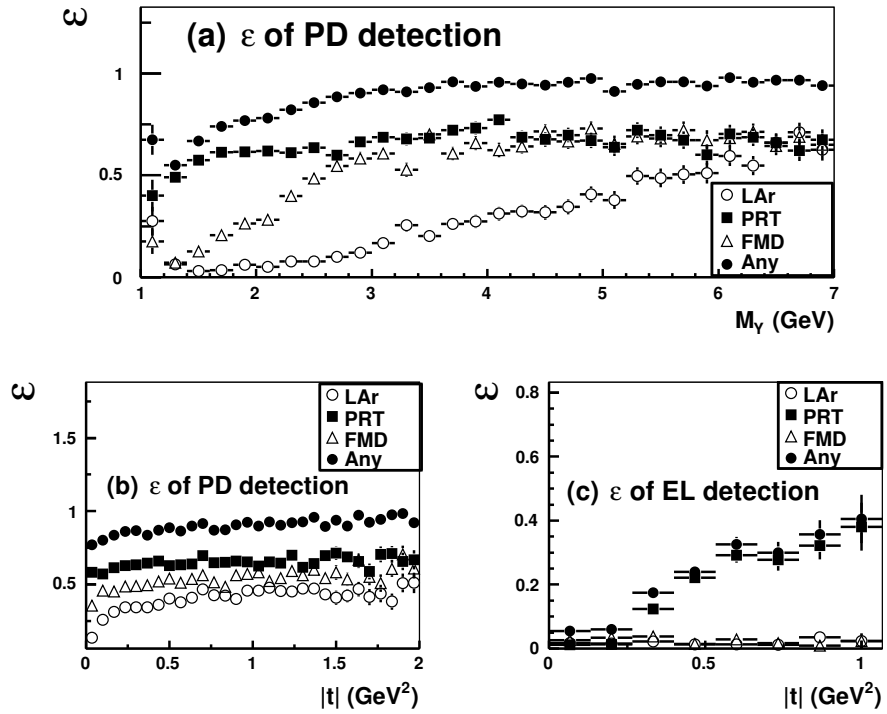

Figure 9.4: Detection efficiencies of the forward cuts in EL and PD $J/\psi \rightarrow e^+e^-$ DIFFVM MC sample; in (a) and (b) efficiencies for PD events as a function of M_Y and $|t|$, respectively; (c) detection efficiency for EL events as a function of $|t|$. The markers represent cuts; $LAr \equiv \eta^{max} < 3.2$ (open circles); PRT (full squares); FMD (open triangles); all cuts combined, ANY, (full circles).

9.4 Systematic Uncertainties

The differential cross section measurements are inherently burdened by statistical errors. There is yet another class of uncertainties present in the measurement,

the systematic uncertainties. The main sources of systematic uncertainties are specified bellow:

- Hadronic final state: an uncertainty on the energy scale of the detector final state objects.
- Trigger efficiency: the uncertainty of 5% is assumed on the trigger efficiency parameterization of the S83 sub-trigger (without the e-tagger part).
- e-tagger acceptance: the acceptance (including the trigger efficiency) of the e-tagger is known with a precision of 5% in the full range of y.
- Luminosity: an uncertainty of 2% is assumed on the total luminosity of the data.
- FMD noise: the procedure of the noise addition to MC samples introduces a systematic uncertainty.
- LRG selection: the LRG diffractive selection relies on an invisible (not measurable by LRG method) energy flow which is provided by the Rapgap MC generator.
- Proton dissociation correction: uncertainty on C^{pdis} is assumed of 7%, see (9.8).
- Background fraction: the fraction of diffractive background given by Pythia MC sample is varied by 50%.
- Hadron level spectra: the uncertainty stemming from the bin-to-bin unfolding procedure is estimated from variations of hadron level spectra of the following variables; y_{gen}, $p_T^{jet1,\ hadr}$, $x_{I\!P}^{hadr}$, $z_{I\!P}^{hadr}$ and t_{gen}.

The uncertainty of each of the elementary sources of systematic error is propagated to every bin of the differential cross sections. The systematic uncertainties are estimated from the Rapgap MC samples because an advantage of a higher statistics of the MC samples if compared with the data samples. For each uncertainty two samples are produced with the systematic error source shifted in a positive and a negative direction using the elementary uncertainty of the source. Then a standard error propagation is used, derivatives are estimated from the shifted samples, the uncertainty is calculated according to the following formula for every variable x in bin i;

$$\sigma_{\alpha_i} = \sqrt{\Sigma_{j=1}^{N_{src}} \left(\frac{d\alpha_i}{ds_j}\right)^2 \cdot \left(\sigma_{s_j}\right)^2}, \tag{9.9}$$

where α_i is an abbreviation for the value of the differential cross section, i.e.

$$\alpha_i = \left(\frac{d\sigma}{dx}\right)_i, \tag{9.10}$$

and the sum in (9.9) runs over the all the sources of the systematic uncertainties. Finally, s_j and σ_{s_j} are the j^{th} source of uncertainty and the error of that source, respectively. Obviously, $d\alpha_i/ds_j$ is the derivative of the differential cross section with respect to the j^{th} source estimated from the shifted samples, i.e

$$\frac{d\alpha_i}{ds_j} = \frac{\alpha_i(s_j^{nominal} + \sigma_{s_j}) - \alpha_i(s_j^{nominal} - \sigma_{s_j})}{2 \cdot \sigma s_j}. \tag{9.11}$$

Finally, the total systematic uncertainty on each data point is formed by adding the individual contributions in quadrature.

9.4.1 Hadronic final state energy scale uncertainty

The final state objects are obtained by means of using the Hadroo2 reconstruction algorithm (see section 7.2). In order to estimate the uncertainty which originates in the unknown energy scale and which translates to the measurement of the HFS it would be needed to propagate the individual uncertainties of the track and calorimetric measurements and to re-run the reconstruction algorithm. This would be a CPU consuming procedure and is, therefore, disfavored. Rather, dedicated neutral current samples (NC) with an electron measured in the SpaCal are used. The measurement of the electron momentum gives a reference for the hadronic final state measurement as there must be a transverse momentum balance in the NC events. The test of calibration of the HFS (done by Calorimeters Analysis Task Force technical working group of the H1 experiment) proceeds as follows; so called p_T balances are calculated in the NC data and MC samples

$$p_T^{bal} = \frac{p_T^{HFS}}{p_T^{e'}}, \tag{9.12}$$

where p_T^{HFS} is the transverse momentum of the total hadronic final state and $p_T^{e'}$ is the transverse momentum of the scattered electron.

These balances are then studied in bins of azimuthal angle of the total HFS, θ_h, or in bins of transverse momentum of the scattered electron, $p_T^{e'}$. The balances are fitted and mean values of the Gaussian fits are plotted as a function of θ_h and $p_T^{e'}$ in figure 9.5 (a) and (b), respectively. They give information on an absolute calibration (provided a precise electron momentum measurement). It can be seen in figure 9.5 (a) that the absolute p_T^{bal} deteriorates at very forward angles θ_h both for data and MC models. This must be caused by leakage of particles in the forward region. Contribution of those particles is then lacking in

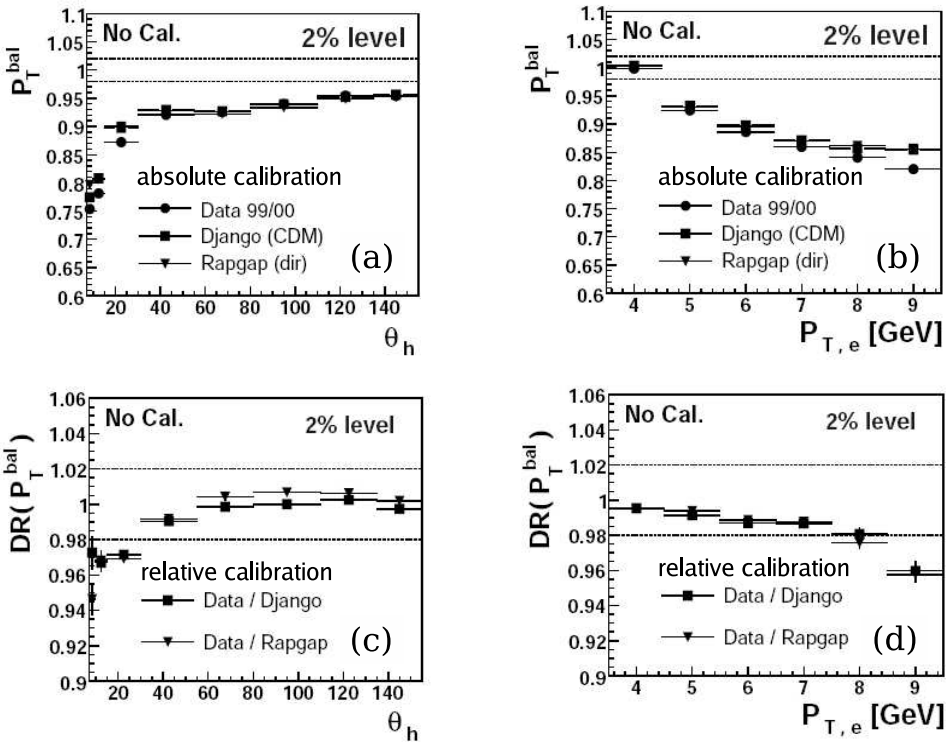

Figure 9.5: Tests of the absolute and relative calibrations using dedicated NC samples. In (a) and (b) are plotted mean values of Gaussian fits of $p_T^{bal} = p_T^{HFS}/p_T^{e'}$ as a function of θ_h and $p_T^{e'}$, respectively, for data (circles) and MC samples Rapgap (triangles) and Django (squares). In (c) and (d) are shown the double ratios $p_T^{bal,\ data}/p_T^{bal,\ MC}$ as a function of θ_h and $p_T^{e'}$, respectively, for both MC models. The binning in θ_h follows an azimuthal segmentation of the LAr calorimeter. (Sakar Osman, talk given at Calorimeter Calibration Meeting, 10^{th} of March 2008)

p_T^{bal} nominator in (9.12). In figure 9.5 (b) the absolute calibration falls away for increasing $p_T^{e'}$ down to 15% for $p_T^{e'} \sim 8$ GeV which does not concern this thesis because the transverse momentum of the electron and consequently of the HFS (due to transverse momentum balance) are constrained to very low values of p_T^{HFS} (< 4 GeV).

In figures 9.5 (c) and (d) double ratios of $p_T^{bal,\ data}/p_T^{bal,\ MC}$ of the values from 9.5 (a) and (b), respectively, are shown. The double ratio is an important observable because it tells what is the level of agreement between data and MC from the point of view of calibration. No matter there is no precise absolute calibration it is the relative calibration which influences the cross section measurement. From the figure 9.5 (c) it can be seen that except for one point in the lowest θ_h bin (for data/Rapgap MC) the relative (data/MC) calibration is consis-

tent at a 3% level and is improving for increasing θ_h. The relative calibration as a function of $p_T^{e'}$ is stable at low values of $p_T^{e'}$ in figure 9.5 (d). Finally, a conservative value of 3% uncertainty on the relative energy scale of the hadronic final state is assumed to contribute to the treatment of the systematic uncertainties.

There are possibilities of an offline calibration improvement of both the absolute but mainly the relative calibration agreement. No such additional calibration procedures are used in this thesis.

9.4.2 FMD noise uncertainty

The residual noise in the FMD is expected to cause an additional rejection of diffractive events. The fraction of events is studied rejected by the FMD cut, cf. (8.7) after the noise addition with respect to the events without noise added to the FMD. In figure 9.6 is the fraction (f^{FMD}) plotted as a function of run number. The FMD noise causes, on average, a constant event rejection of $\sim 2.5\%$ with an error of roughly 0.5% which is used as a systematic error. Without harm of generality the values are obtained from the MC sample in the *low* p_T^{jets} kinematics only.

9.4.3 LRG uncertainty

Since the diffractive events are selected by means of the large rapidity gap method the measurement relies on a correct description of undetected forward energy flow in the MC model (Rapgap). A study was made in [40], where efficiencies of LRG selected samples of H1 data are compared with leading proton measurements (proton measured in the FPS). These efficiencies are compared for data and MC simulations, i.e. ε_{data} and ε_{MC}, respectively. Resulting comparison of the efficiencies for jet events in photoproduction reads;

$$f_\varepsilon = \frac{\varepsilon_{data}}{\varepsilon_{MC}} = 1.11 \pm 0.08_{syst} \pm 0.21_{stat} = 1.11 \pm 0.22. \tag{9.13}$$

Finally, a symmetric uncertainty of 30% is considered for the LRG method, though the asymmetric mean value in (9.13). The events that do not pass the LRG selection are assigned weights of $\pm 30\%$.

9.4.4 Hadron level spectra uncertainties

The correction of the data to the hadron level makes use of one hadronization model only. Usually, to estimate the error induced by the correction procedure another MC model is used. There is no other model suited for this analysis, therefore, in order to estimate the uncertainty of the correction factors ($1/A$) the hadron level spectra are varied for some variables in such a way that they change the detector level distributions by amounts given by statistical errors of

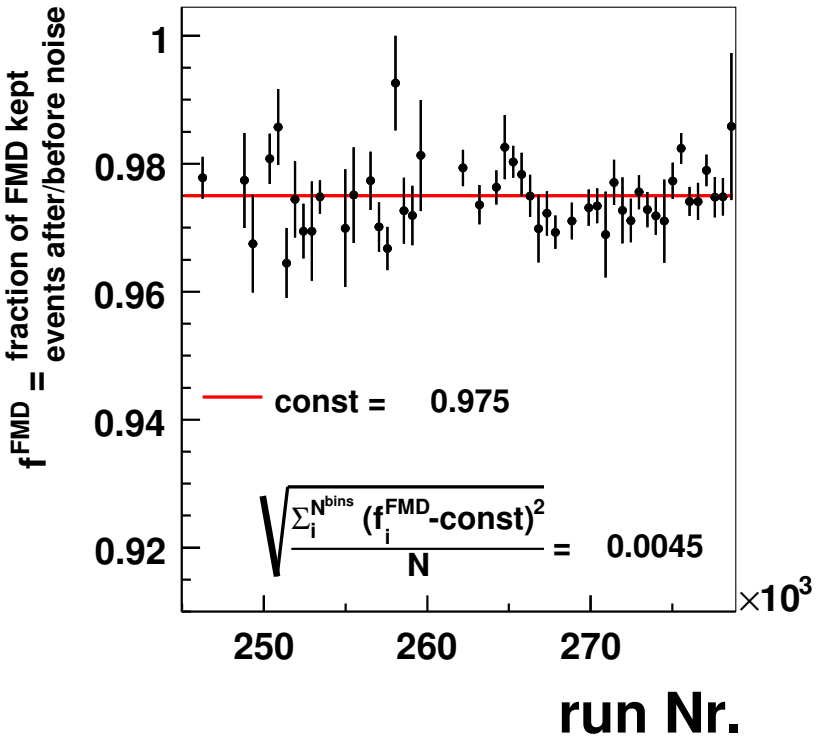

Figure 9.6: Fraction of MC events rejected by the FMD cut in samples with the FMD noise to a sample without the FMD noise applied (dots). Displayed as a function of run number. constant fit (line).

the data or by difference between the data and MC distributions at the detector level. Similar procedure is used also in [3, 15]. In table 9.1 the variables are listed together with corresponding reweighting function and parameter value for the spectra variations.

In figure 9.7 are shown the detector level distributions for the *low* p_T^{jets} analysis for the data and unaltered MC together with detector level MC distributions obtained with samples reweighted according to table 9.1. The distributions are presented for y_e, p_T^{jet1}, $log_{10}(x_{I\!P})$ and $z_{I\!P}$. In each of the distributions in this figure the shape was varied only in the one, respective, variable. Detector level distribution is not presented for reweighted t_{gen} as there is no detector level observable in which the effect is visible. In figure 9.8 are shown the effects of shape reweighting for the *high* p_T^{jets} analysis.

The errors induced by the spectra variations are taken into account by calculation of the acceptances, A, by means of use of these altered Rapgap ($I\!P$ and $I\!R$) MC samples.

variable	function	parameter
y_{gen}	$(y_{gen})^{\pm\alpha}$	$\alpha = 0.3$
$p_T^{jet1,hadr}$	$(p_T^{jet1,hadr})^{\pm\alpha}$	$\alpha = 0.4$ (0.8)
$x_{I\!P}^{hadr}$	$(x_{I\!P}^{hadr})^{\pm\alpha}$	$\alpha = 0.2$ (0.4)
$z_{I\!P}^{hadr}$	$(z_{I\!P}^{hadr})^{\pm\alpha}$	$\alpha = 0.3$
$\lvert t_{gen}\rvert$	$e^{\pm\alpha\cdot\lvert t_{gen}\rvert}$	$\alpha = 2$

Table 9.1: Variables used for hadron level spectra reweighting. The reweighting functions are specified in the second column and the parameters of these functions are shown in the third column for the *low* p_T^{jets} analysis (values of parameters in brackets apply to the *high* p_T^{jets} analysis).

9.4.5 Summary of systematics

In this thesis the systematic uncertainties are divided into two classes; the correlated and the uncorrelated ones. The idea is such that the correlated systematic uncertainties are those which change the normalization of the final cross section by a global factor, thus, the errors are uniformly proportional to the bin content. The uncorrelated systematic uncertainties are those which act non-trivially in some of the event observables. Following sources are considered to represent the uncorrelated systematic uncertainties; HFS energy scale, LRG efficiency, variations of hadron level shapes. The set of correlated systematic uncertainties comprises; luminosity, trigger efficiency, normalization of non-diffractive background, proton dissociation correction, FMD noise, e-tagger acceptance parameterization. In table 9.2 are summarized the sources of systematics together with the uncertainty of each of them and an ultimate effect on the measured total cross sections (presented in chapter 10) in the *low* p_T^{jets} and *high* p_T^{jets} analyses, respectively. Due to a smallness of the non-diffractive background the uncertainty of its normalization is placed among the correlated ones, though it changes the differential cross sections non-trivially.

source	**elem. unc.**	$\Delta\sigma$ *low* p_T^{jets}	$\Delta\sigma$ *high* p_T^{jets}	correl./uncorrel.
HFS en. scale	3%	9.2%	13.6%	U
LRG efficiency	30%	8.1%	6.2%	U
shape y_{gen}	0.3	0.2%	1.2%	U
shape $p_T^{jet1,hadr}$	0.4 (0.8)	0.8%	1.2%	U
shape $x_{I\!P}^{hadr}$	0.3 (0.4)	5.3%	10.2%	U
shape $z_{I\!P}^{hadr}$	0.3	2.9%	4.3%	U
shape $\lvert t_{gen}\rvert$	2	4.2%	3.5%	U
luminosity	2%	2%	2%	C
trigger eff.	5%	5%	5%	C
non-diff. bgd.	50%	2.6%	2.8%	C
C^{pdis}	7%	7%	7%	C
FMD noise	0.5%	0.5%	0.5%	C
e-tagger acc.	5%	5%	5%	C
total		$\sim 14\%$ (U) $\sim 10\%$ (C)	$\sim 18\%$ (U) $\sim 11\%$ (C)	

Table 9.2: Summary of systematic sources. Shown are the sources, the elementary uncertainty of each source, the effect on the total measured cross section for both analyses, *low* p_T^{jets} and *high* p_T^{jets}. The last column indicates whether the uncertainty is correlated (C) or uncorrelated (U).

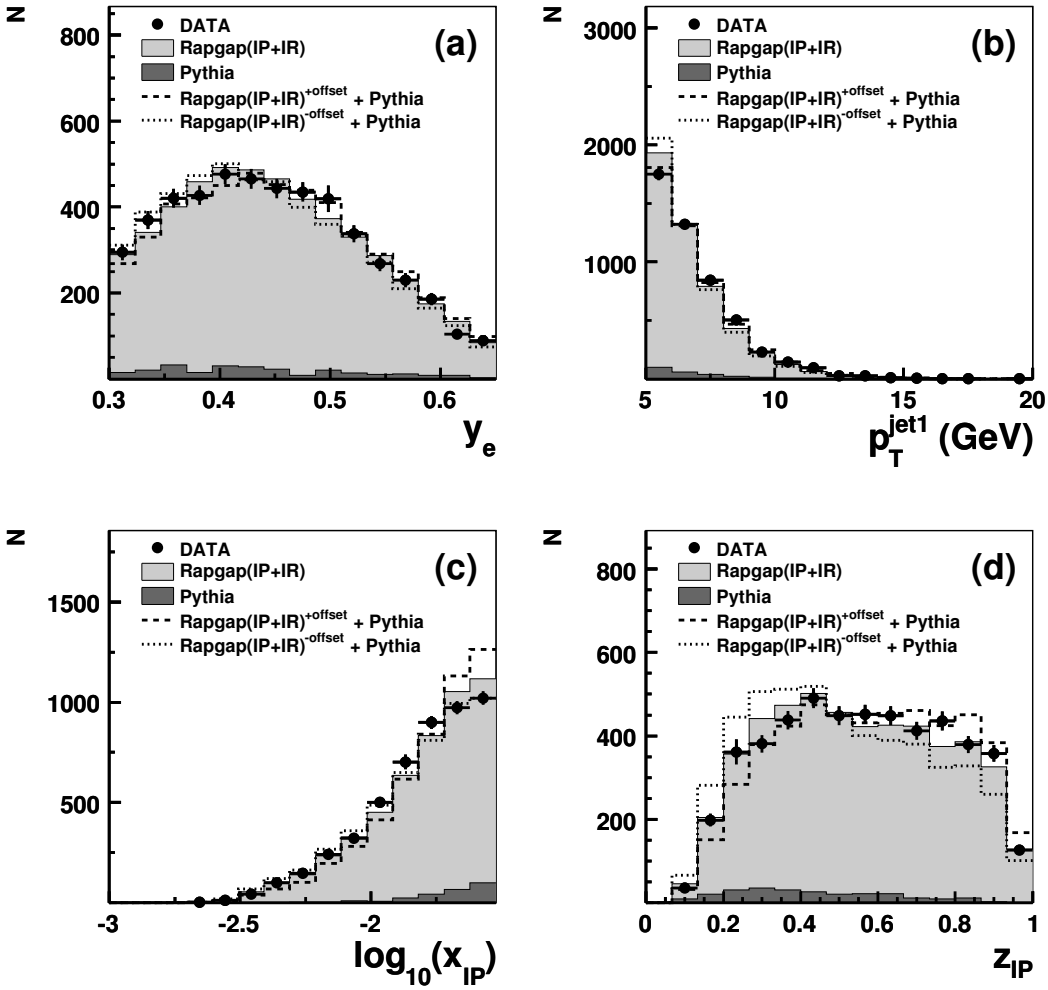

Figure 9.7: Detector level distributions for diffractive *low* p_T^{jets} analysis; data (dots), unaltered Rapgap($I\!P + I\!R$) (light filled histogram), Pythia (dark filled histogram). In (a) the y_e distribution is presented with y_{gen} spectrum reweighted Rapgap($I\!P + I\!R$) (dotted and dashed histograms). Similarly, in (b) p_T^{jet1} with $p_T^{jet1,hadr}$ reweighting, in (c) $log_{10}(x_{I\!P})$ with $log_{10}(x_{I\!P}^{hadr})$ reweighting and in (d) $z_{I\!P}$ with $z_{I\!P}^{hadr}$ reweighting.

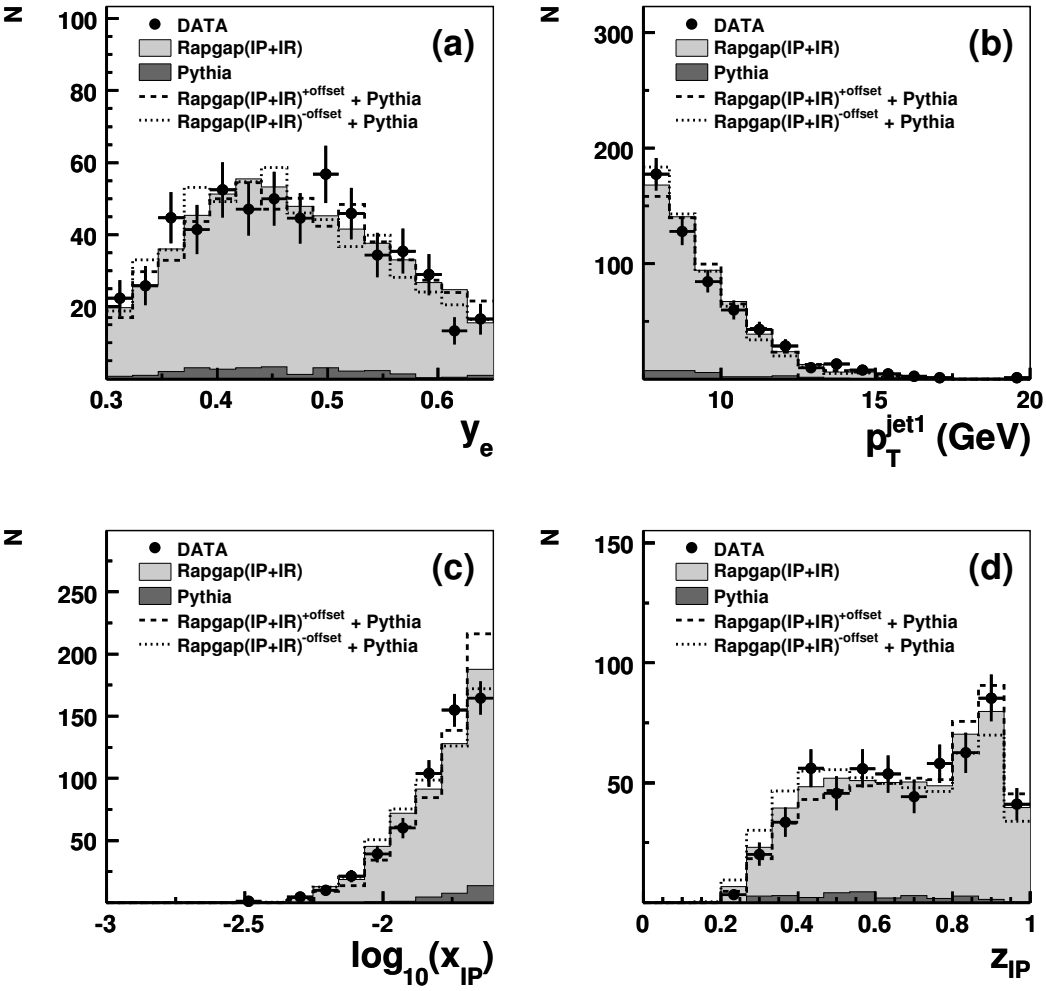

Figure 9.8: Detector level distributions for diffractive *high* p_T^{jets} analysis; data (dots), unaltered Rapgap($I\!P + I\!R$) (light filled histogram), Pythia (dark filled histogram). In (a) the y_e distribution is presented with y_{gen} spectrum reweighted Rapgap($I\!P + I\!R$) (dotted and dashed histograms). Similarly, in (b) p_T^{jet1} with $p_T^{jet1,hadr}$ reweighting, in (c) $log_{10}(x_{I\!P})$ with $log_{10}(x_{I\!P}^{hadr})$ reweighting and in (d) $z_{I\!P}$ with $z_{I\!P}^{hadr}$ reweighting.

Chapter 10

Results

In this chapter the differential cross sections measured in the data are compared with the NLO QCD predictions based on various DPDF fits. The presented results are public H1 preliminary results which were presented at the DIS08 conference (see [41]). The notation is changed for the jet observables p_T^{jet1} and p_T^{jet2}, they are replaced by E_T^{jet1} and E_T^{jet2}, respectively, in the differential cross section plots in order to be consistent with [41].

First is presented the measurement in the cut scheme of *low* p_T^{jets} denoted as $E_T^{jet1} > 5$ GeV and $E_T^{jet2} > 4$ GeV in the figures. Next is presented the analysis restricted to larger transverse momenta *high* p_T^{jets} denoted as $E_T^{jet1} > 7.5$ GeV and $E_T^{jet2} > 6.5$ GeV in the figures.

10.1 Results for *low* E_T^{jets} Analysis

The NLO calculations (FR and KK) predict larger cross sections than the data. The overall suppression factors, S, of the NLO calculations needed to predict the total measured cross section depend mainly on the DPDF set used. There is a very good agreement between FR and KK both for the total and the differential cross sections. The total measured cross section (σ_{tot}^{data}) and the suppression factors ($S = \sigma^{data}/\sigma^{NLO}$) are listed below.

$$\sigma_{tot}^{data} = 305.4 \text{ pb} \pm 5.6(stat.) \pm 54.4(syst.), \tag{10.1}$$
$$S_{fitB}^{FR} = 0.54 \pm 0.01(stat.) \pm 0.10(syst.)^{+0.14}_{-0.13}(scale.), \tag{10.2}$$
$$S_{fitB}^{KK} = 0.51 \pm 0.01(stat.) \pm 0.10(syst.), \tag{10.3}$$
$$S_{fitA}^{FR} = 0.43 \pm 0.01(stat.) \pm 0.10(syst.), \tag{10.4}$$
$$S_{fitJets}^{FR} = 0.65 \pm 0.01(stat.) \pm 0.11(syst.), \tag{10.5}$$

where size of the renormalization scale uncertainty from (10.2) can be expected to be similar in (10.3), (10.4) and (10.5).

In figure 10.1 the measurement is presented of the differential cross section

as a function of E_T^{jet1}. The statistical and uncorrelated systematic uncertainties are added in quadrature and are represented with error bars (inner is statistical only). The correlated uncertainties are shown separately with a dark band. The FR and KK NLO calculations based on Fit B are multiplied by the hadronization correction factors (shown underneath) and are multiplied by a common scale factor of 0.53 (which is a trade-off value between (10.2) and (10.3)). The NLO calculations are always shown for the central renormalization scale ($\mu_r^2 = E_T^{2,\ jet1}$). Predictions are also presented for FR Fit B with renormalization scale variations ($\mu_r/2$ and $2.\mu_r$) depicted as a band around the central FR Fit B values. In the lower part of figure 10.1 ratios of the measured differential cross sections in the data to the predictions is presented (data/theory). No scaling factors are applied to the NLO predictions in this case, only the hadronization corrections are applied. The ratio is shown for the FR Fit B calculation with correspondingly propagated uncertainties stemming from the data. Also the renormalization scale variations of the ratio are presented for FR Fit B. Ratios with respect to the FR Fit A and FR Fit Jets calculations are also shown in order to illustrate the approximative DPDF uncertainty. In a similar way the results are presented for $z_{I\!P}$, x_γ and $\log_{10}(x_{I\!P})$ in figures 10.2, 10.3 and 10.4, respectively.

In figure 10.1 a somewhat harder $d\sigma/dE_T^{jet1}$ slope is measured in data than is predicted by both NLO calculations. Consequently the ratio (data/theory) in the same figure shows a suggestion of a weaker suppression as E_T^{jet1} increases. Taking into account all uncertainties considered the value of the ratio for $E_T^{jet1} < 7$ GeV is roughly within a range of $0.3 - 0.7$. In contrast for $E_T > 7$ GeV the ratio lies in the range $0.4 - 1$.

In figure 10.2 a good description of shape of the measured $d\sigma/dz_{I\!P}$ is provided by Fit B. Therefore, the ratio of data to theory is flat for FR Fit B. It is also almost independent of DPDF at low $z_{I\!P}$. However, for larger $z_{I\!P}$ the DPDF uncertainty increases dramatically. The hatched area in the last $z_{I\!P}$ bin in the figure 10.2 indicates that the results are presented beyond the range of validity of the DPDF fits ($z_{I\!P} \leq 0.8$ for H1 2006 Fit A or B and $z_{I\!P} \leq 0.9$ for H1 2007 Fit Jets, [14, 15]).

In figure 10.3 a very good description is obtained of the measured $d\sigma/dx_\gamma$ shape by Fit B. From the data to theory ratio in figure 10.3 it can be deduced that there is no significant x_γ dependence of the suppression in contrast to expectations [1] but in agreement with previous results [3, 18]. The resolved region is often identified with a range of $x_\gamma < 0.75$ where the resolved component is expected to prevail the direct one, see [3, 18].

In figure 10.4 a very good description of the $d\sigma/dlog_{10}(x_{I\!P})$ shape is provided by Fit B. The measured ratio in figure 10.4 is consistent with independence of $x_{I\!P}$.

The variations due the DPDF uncertainties are of similar size to the scale variations of FR Fit B in the $d\sigma/dE_T^{jet1}$, $d\sigma/dx_\gamma$ and $d\sigma/dlog_{10}(x_{I\!P})$ plots. As the DPDF uncertainty depends strongly on $z_{I\!P}$, it could be reduced by means of use

of a limited range in $z_{I\!P}$ where the DPDF fits give similar predictions. However, no such cut is applied in this thesis.

10.2 Results for *high* E_T^{jets} Analysis

In the analysis with higher transverse energy range of the jets, the NLO calculations (FR and KK) predict larger cross sections than the data again. The total measured cross section and the factors by which the NLO calculations exceed the data are listed below.

$$\sigma_{tot}^{data} = 37 \text{ pb} \pm 2(stat.) \pm 8(syst.), \tag{10.6}$$
$$S_{fitB}^{FR} = 0.61 \pm 0.03(stat.) \pm 0.13(syst.)^{+0.16}_{-0.14}(scale.), \tag{10.7}$$
$$S_{fitB}^{KK} = 0.62 \pm 0.03(stat.) \pm 0.14(syst.), \tag{10.8}$$
$$S_{fitA}^{FR} = 0.44 \pm 0.02(stat.) \pm 0.09(syst.), \tag{10.9}$$
$$S_{fitJets}^{FR} = 0.79 \pm 0.04(stat.) \pm 0.16(syst.). \tag{10.10}$$

In general the suppression factors have weakened with respect to the lower E_T range analysis (previous section). The FR Fit B and KK Fit B calculations are presented with a common suppression factor of 0.61 applied to the differential cross section comparisons in figures 10.5 - 10.13.

In figure 10.5 the $d\sigma/dE_T^{jet1}$ shape is in a reasonable agreement with the FR and KK Fit B calculations. This is reflected in the ratio in figure 10.5 where the E_T^{jet1} dependence cannot be independently verified but is not excluded. The variations of the ratio allowed within the uncertainties show that the suppression is in the range off to 0.9 in the first two E_T^{jet1} bins.

In figure 10.6 FR and KK predictions based on Fit B are able to describe the measured $d\sigma/dz_{I\!P}$ shape taking into account the large uncertainties. In the ratio plot again a large DPDF uncertainty is observed at high $z_{I\!P}$ values. The hatching in the last $z_{I\!P}$ bin indicates that the fits are used beyond their validity range.

In figure 10.7 both Fit B NLO predictions manage to reproduce the shape of the $d\sigma/dx_\gamma$. Within the precision of the analysis the ratio is independent of x_γ. It is also interesting to note different shapes of the $d\sigma/dx_\gamma$ in figures 10.3 and 10.7. The resolved contribution becomes less significant in the kinematics with jets in the higher E_T range.

In figures 10.8 - 10.13 the results are presented for $x_{I\!P}$, W, $|\eta^{jets}|$, $\langle\eta^{jets}\rangle$, M_X and M_{12}, respectively. Given the large uncertainties the shapes are described by the FR and KK Fit B predictions rather well. Fluctuations due to low statistics in some bins are observed in the ratios.

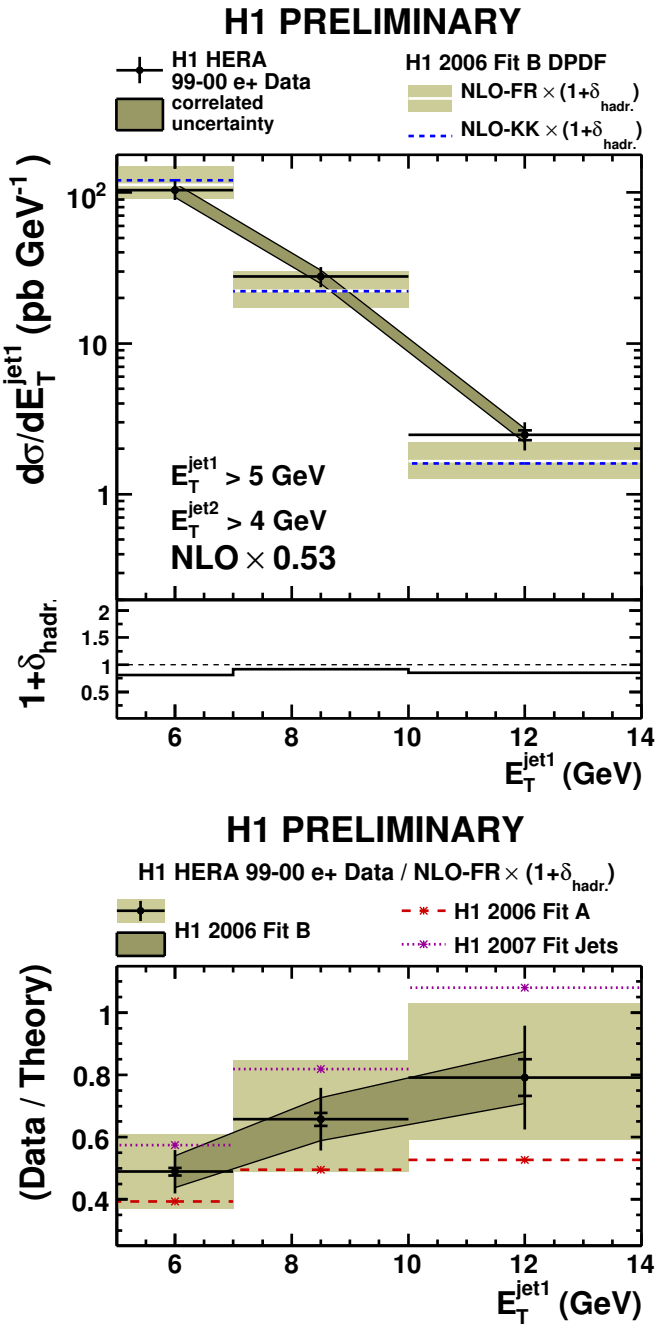

Figure 10.1: Upper plot: measurement of the differential cross section $\mathrm{d}\sigma/\mathrm{d}E_T^{jet1}$. The points show the data, the inner error bars on the points are statistical and the outer error bars show statistical and uncorrelated uncertainties added in quadrature. The correlated systematic errors are indicated by the dark band. The data are compared with predictions based on the H1 2006 Fit B DPDFs, scaled by a constant factor of 0.53, obtained using the FR (white line) and KK (dashed line) calculations. Both predictions are corrected for hadronization effects using the factor $(1+\delta_{hadr})$ shown below the main figure. The effect on the FR calculation of varying μ_r by factors of 0.5 and 2.0 is shown in the light band. Lower plot: ratio of the measured differential cross section to the FR calculation based on the H1 2006 Fit B DPDF set and corrected for hadronization effects. The experimental and theory scale uncertainties are indicated as for the cross section plot. Also indicated are the central values obtained when the H1 2006 Fit A or H1 2007 Fit Jets DPDFs are used in place of H1 2006 Fit B.

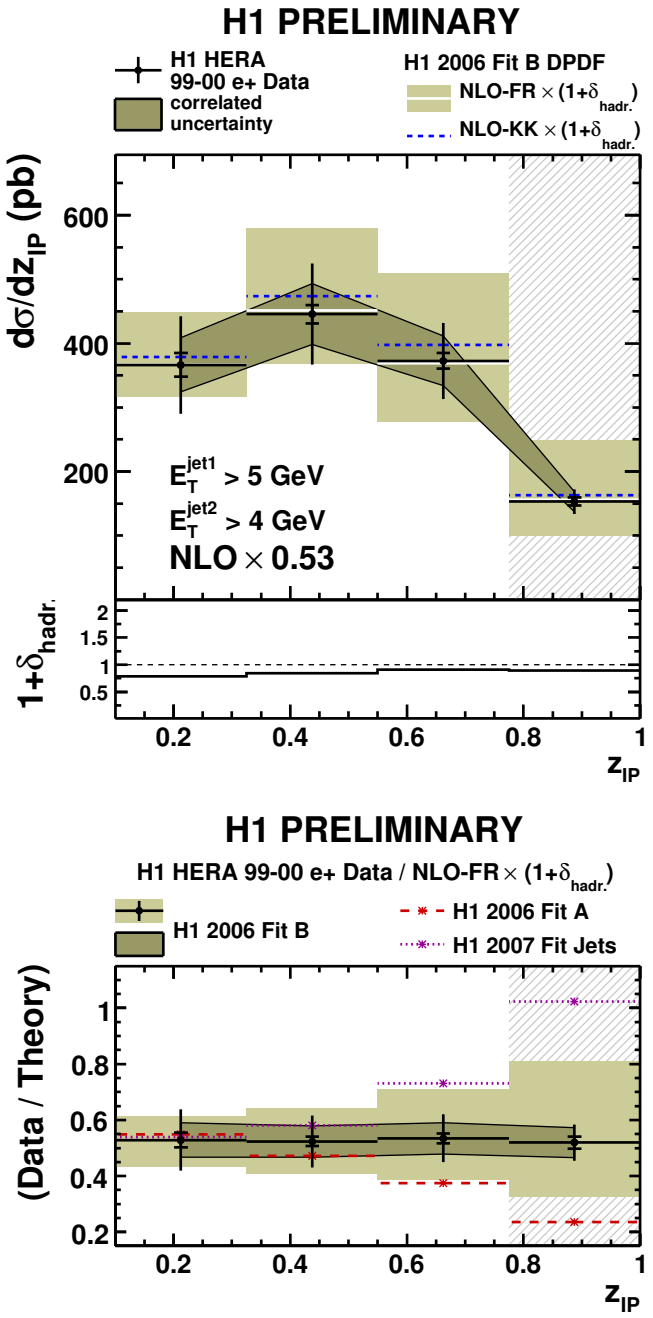

Figure 10.2: Upper plot: measurement of the differential cross section $\mathrm{d}\sigma/\mathrm{d}z_{I\!P}$. The points show the data, the inner error bars on the points are statistical and the outer error bars show statistical and uncorrelated uncertainties added in quadrature. The correlated systematic errors are indicated by the dark band. The data are compared with predictions based on the H1 2006 Fit B DPDFs, scaled by a constant factor of 0.53, obtained using the FR (white line) and KK (dashed line) calculations. Both predictions are corrected for hadronization effects using the factor $(1+\delta_{hadr})$ shown below the main figure. The effect on the FR calculation of varying μ_r by factors of 0.5 and 2.0 is shown in the light band. Lower plot: ratio of the measured differential cross section to the FR calculation based on the H1 2006 Fit B DPDF set and corrected for hadronization effects. The experimental and theory scale uncertainties are indicated as for the cross section plot. Also indicated are the central values obtained when the H1 2006 Fit A or H1 2007 Fit Jets DPDFs are used in place of H1 2006 Fit B.

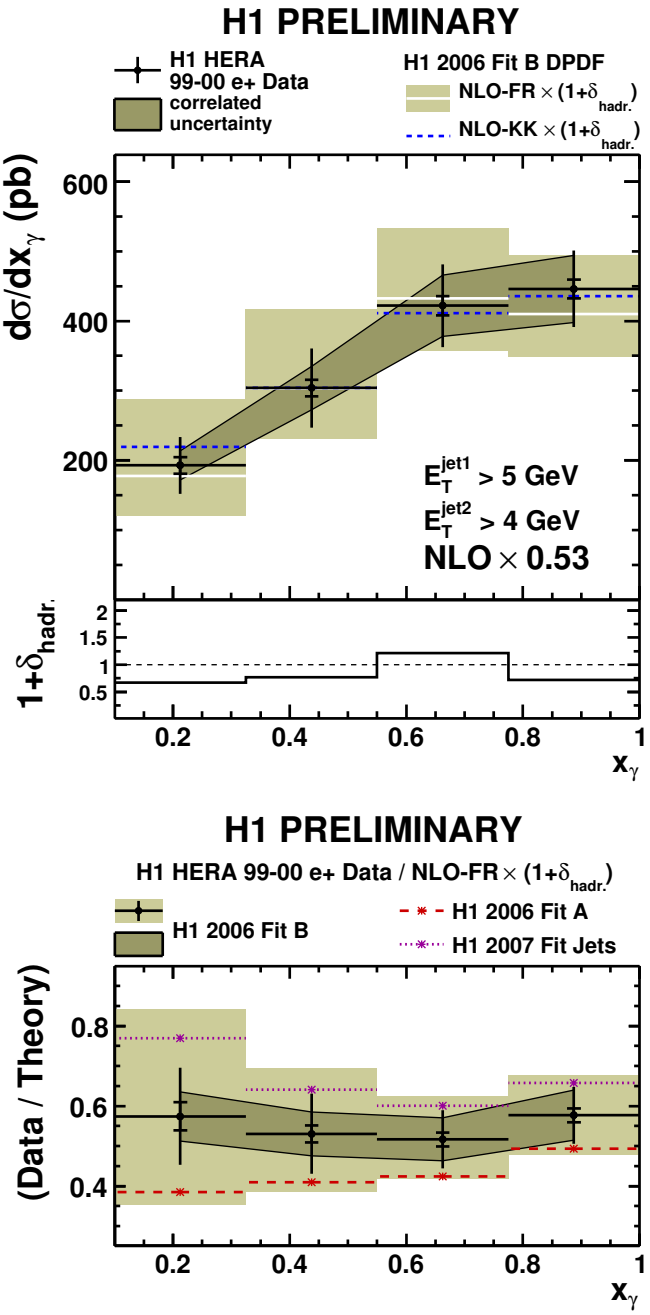

Figure 10.3: Upper plot: measurement of the differential cross section $\mathrm{d}\sigma/\mathrm{d}x_\gamma$. The points show the data, the inner error bars on the points are statistical and the outer error bars show statistical and uncorrelated uncertainties added in quadrature. The correlated systematic errors are indicated by the dark band. The data are compared with predictions based on the H1 2006 Fit B DPDFs, scaled by a constant factor of 0.53, obtained using the FR (white line) and KK (dashed line) calculations. Both predictions are corrected for hadronization effects using the factor $(1+\delta_{hadr})$ shown below the main figure. The effect on the FR calculation of varying μ_r by factors of 0.5 and 2.0 is shown in the light band. Lower plot: ratio of the measured differential cross section to the FR calculation based on the H1 2006 Fit B DPDF set and corrected for hadronization effects. The experimental and theory scale uncertainties are indicated as for the cross section plot. Also indicated are the central values obtained when the H1 2006 Fit A or H1 2007 Fit Jets DPDFs are used in place of H1 2006 Fit B.

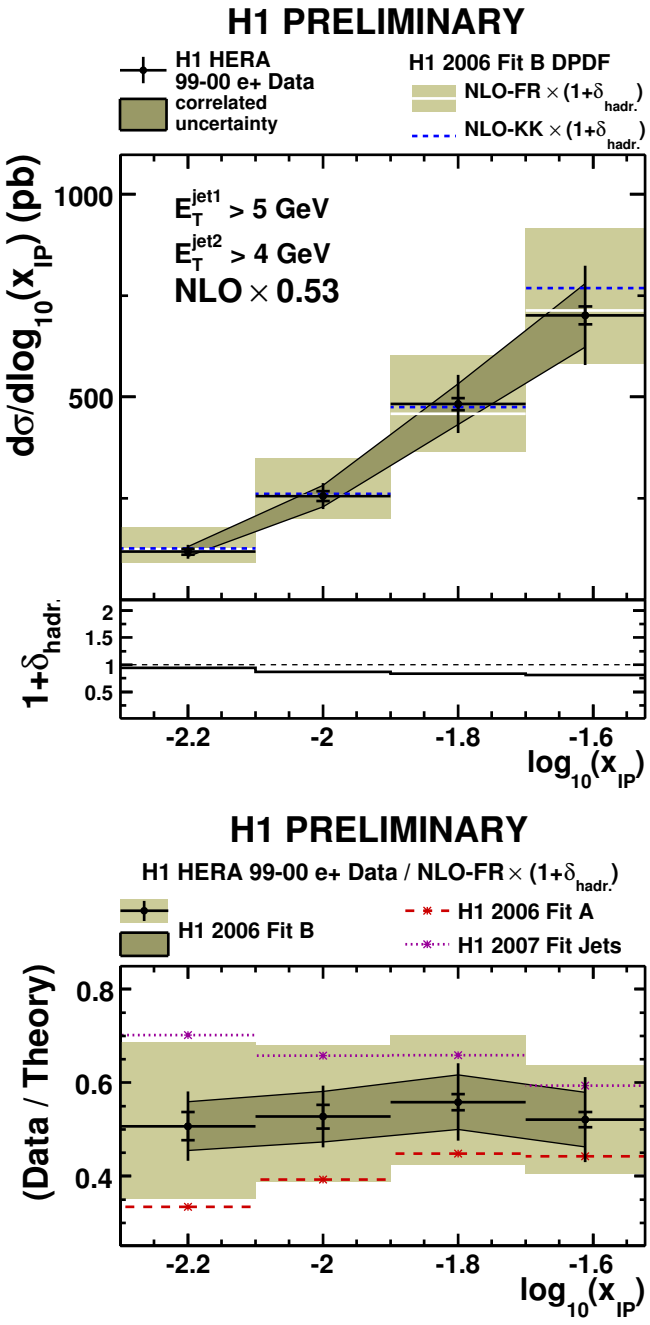

Figure 10.4: Upper plot: measurement of the differential cross section $\mathrm{d}\sigma/\mathrm{d}log_{10}(x_{I\!P})$. The points show the data, the inner error bars on the points are statistical and the outer error bars show statistical and uncorrelated uncertainties added in quadrature. The correlated systematic errors are indicated by the dark band. The data are compared with predictions based on the H1 2006 Fit B DPDFs, scaled by a constant factor of 0.53, obtained using the FR (white line) and KK (dashed line) calculations. Both predictions are corrected for hadronization effects using the factor $(1 + \delta_{hadr})$ shown below the main figure. The effect on the FR calculation of varying μ_r by factors of 0.5 and 2.0 is shown in the light band. Lower plot: ratio of the measured differential cross section to the FR calculation based on the H1 2006 Fit B DPDF set and corrected for hadronization effects. The experimental and theory scale uncertainties are indicated as for the cross section plot. Also indicated are the central values obtained when the H1 2006 Fit A or H1 2007 Fit Jets DPDFs are used in place of H1 2006 Fit B.

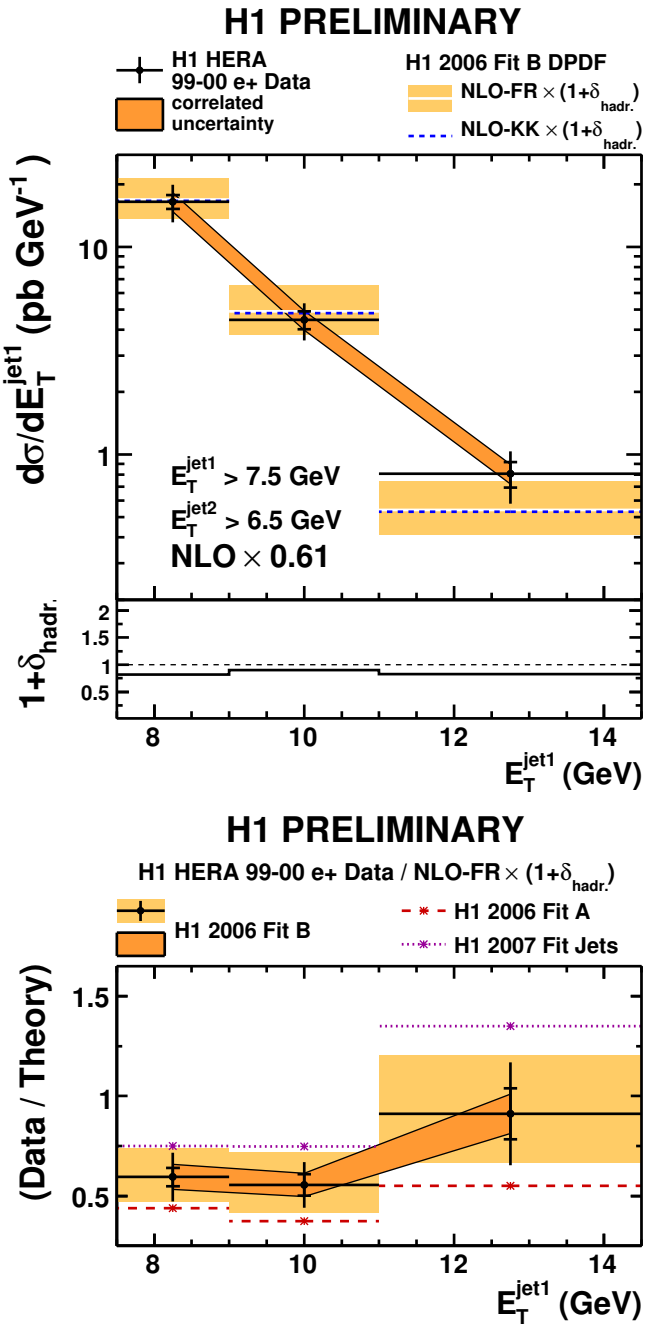

Figure 10.5: Upper plot: measurement of the differential cross section $\mathrm{d}\sigma/\mathrm{d}E_T^{jet1}$. The points show the data, the inner error bars on the points are statistical and the outer error bars show statistical and uncorrelated uncertainties added in quadrature. The correlated systematic errors are indicated by the dark band. The data are compared with predictions based on the H1 2006 Fit B DPDFs, scaled by a constant factor of 0.61, obtained using the FR (white line) and KK (dashed line) calculations. Both predictions are corrected for hadronization effects using the factor $(1+\delta_{hadr})$ shown below the main figure. The effect on the FR calculation of varying μ_r by factors of 0.5 and 2.0 is shown in the light band. Lower plot: ratio of the measured differential cross section to the FR calculation based on the H1 2006 Fit B DPDF set and corrected for hadronization effects. The experimental and theory scale uncertainties are indicated as for the cross section plot. Also indicated are the central values obtained when the H1 2006 Fit A or H1 2007 Fit Jets DPDFs are used in place of H1 2006 Fit B.

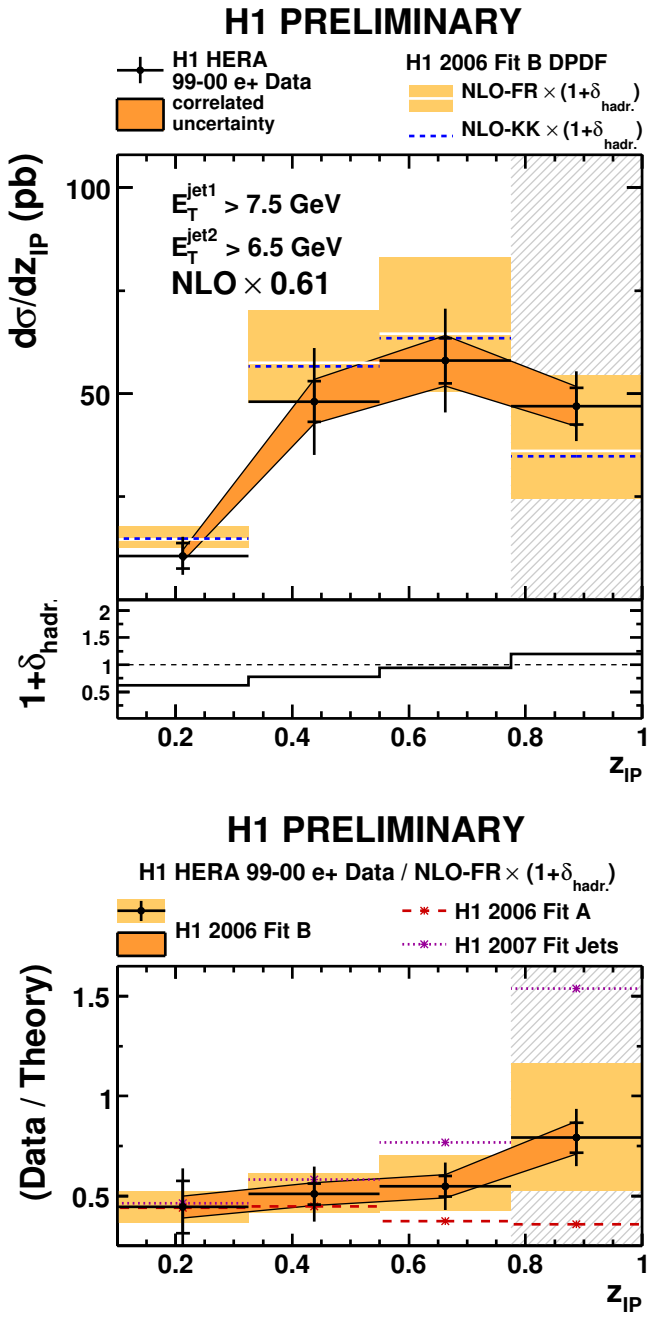

Figure 10.6: Upper plot: measurement of the differential cross section $\mathrm{d}\sigma/\mathrm{d}z_{I\!P}$. The points show the data, the inner error bars on the points are statistical and the outer error bars show statistical and uncorrelated uncertainties added in quadrature. The correlated systematic errors are indicated by the dark band. The data are compared with predictions based on the H1 2006 Fit B DPDFs, scaled by a constant factor of 0.61, obtained using the FR (white line) and KK (dashed line) calculations. Both predictions are corrected for hadronization effects using the factor $(1+\delta_{hadr})$ shown below the main figure. The effect on the FR calculation of varying μ_r by factors of 0.5 and 2.0 is shown in the light band. Lower plot: ratio of the measured differential cross section to the FR calculation based on the H1 2006 Fit B DPDF set and corrected for hadronization effects. The experimental and theory scale uncertainties are indicated as for the cross section plot. Also indicated are the central values obtained when the H1 2006 Fit A or H1 2007 Fit Jets DPDFs are used in place of H1 2006 Fit B.

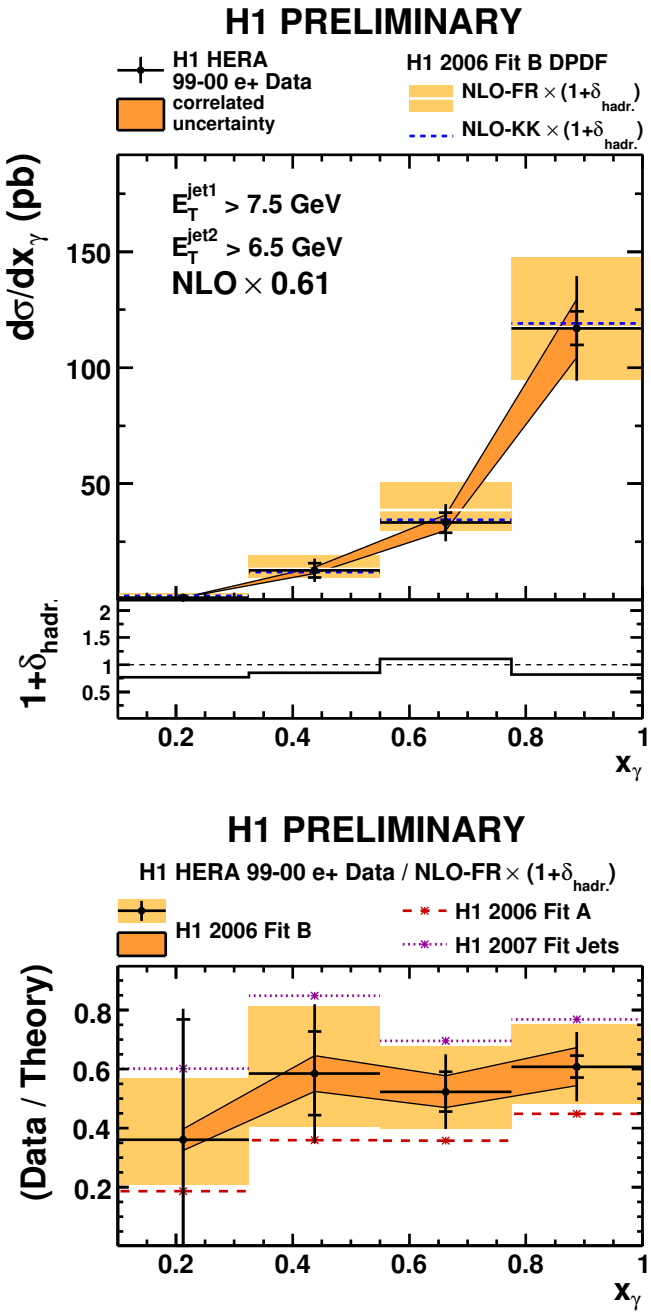

Figure 10.7: Upper plot: measurement of the differential cross section $\mathrm{d}\sigma/\mathrm{d}x_\gamma$. The points show the data, the inner error bars on the points are statistical and the outer error bars show statistical and uncorrelated uncertainties added in quadrature. The correlated systematic errors are indicated by the dark band. The data are compared with predictions based on the H1 2006 Fit B DPDFs, scaled by a constant factor of 0.61, obtained using the FR (white line) and KK (dashed line) calculations. Both predictions are corrected for hadronization effects using the factor $(1+\delta_{hadr})$ shown below the main figure. The effect on the FR calculation of varying μ_r by factors of 0.5 and 2.0 is shown in the light band. Lower plot: ratio of the measured differential cross section to the FR calculation based on the H1 2006 Fit B DPDF set and corrected for hadronization effects. The experimental and theory scale uncertainties are indicated as for the cross section plot. Also indicated are the central values obtained when the H1 2006 Fit A or H1 2007 Fit Jets DPDFs are used in place of H1 2006 Fit B.

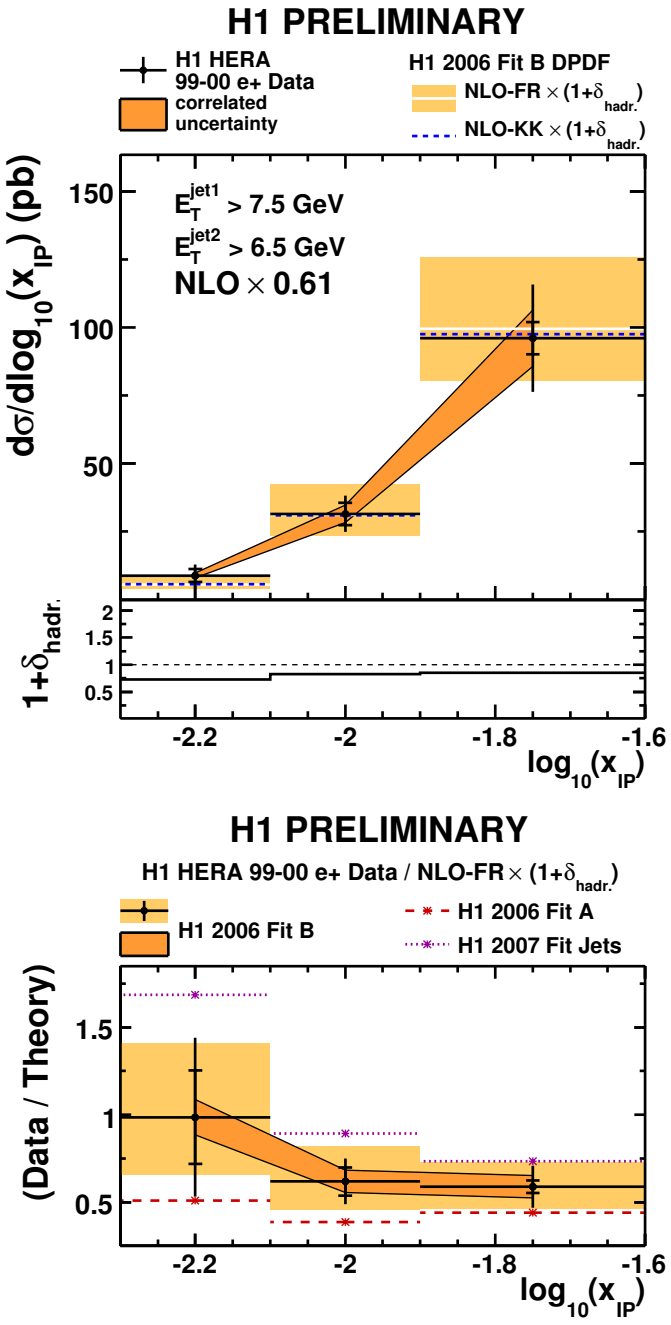

Figure 10.8: Upper plot: measurement of the differential cross section $\mathrm{d}\sigma/\mathrm{d}log_{10}(x_{I\!P})$. The points show the data, the inner error bars on the points are statistical and the outer error bars show statistical and uncorrelated uncertainties added in quadrature. The correlated systematic errors are indicated by the dark band. The data are compared with predictions based on the H1 2006 Fit B DPDFs, scaled by a constant factor of 0.61, obtained using the FR (white line) and KK (dashed line) calculations. Both predictions are corrected for hadronization effects using the factor $(1 + \delta_{hadr})$ shown below the main figure. The effect on the FR calculation of varying μ_r by factors of 0.5 and 2.0 is shown in the light band. Lower plot: ratio of the measured differential cross section to the FR calculation based on the H1 2006 Fit B DPDF set and corrected for hadronization effects. The experimental and theory scale uncertainties are indicated as for the cross section plot. Also indicated are the central values obtained when the H1 2006 Fit A or H1 2007 Fit Jets DPDFs are used in place of H1 2006 Fit B.

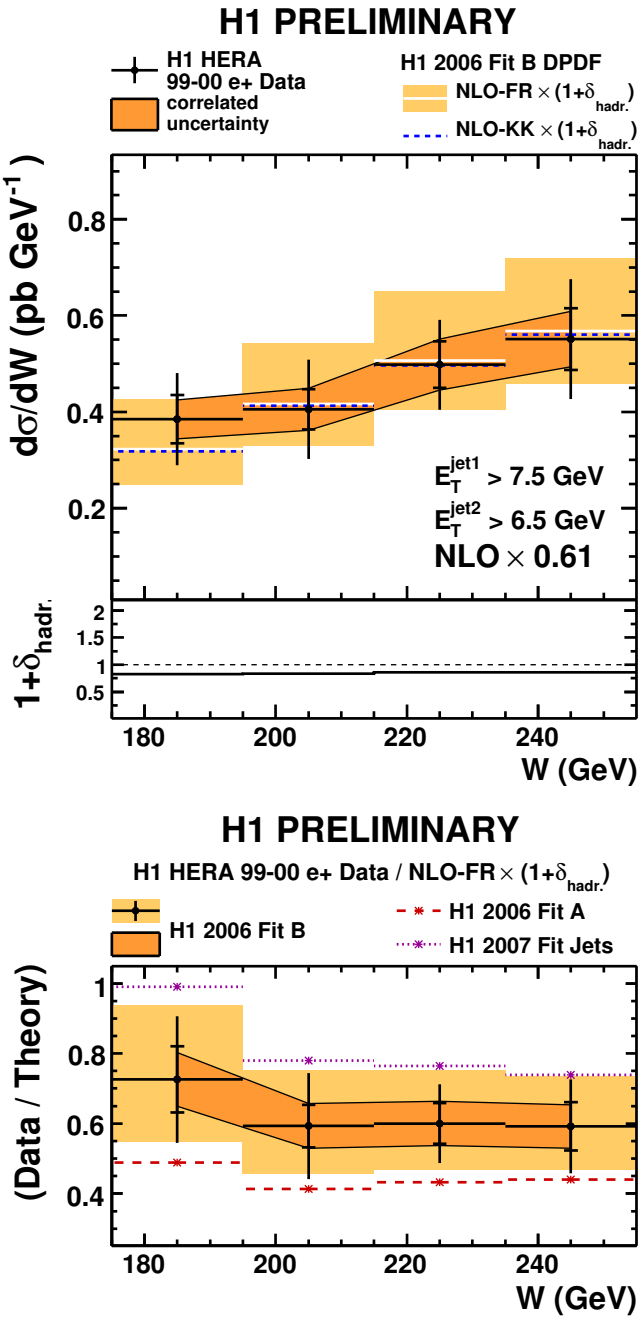

Figure 10.9: Upper plot: measurement of the differential cross section $\mathrm{d}\sigma/\mathrm{d}W$. The points show the data, the inner error bars on the points are statistical and the outer error bars show statistical and uncorrelated uncertainties added in quadrature. The correlated systematic errors are indicated by the dark band. The data are compared with predictions based on the H1 2006 Fit B DPDFs, scaled by a constant factor of 0.61, obtained using the FR (white line) and KK (dashed line) calculations. Both predictions are corrected for hadronization effects using the factor $(1+\delta_{hadr})$ shown below the main figure. The effect on the FR calculation of varying μ_r by factors of 0.5 and 2.0 is shown in the light band. Lower plot: ratio of the measured differential cross section to the FR calculation based on the H1 2006 Fit B DPDF set and corrected for hadronization effects. The experimental and theory scale uncertainties are indicated as for the cross section plot. Also indicated are the central values obtained when the H1 2006 Fit A or H1 2007 Fit Jets DPDFs are used in place of H1 2006 Fit B.

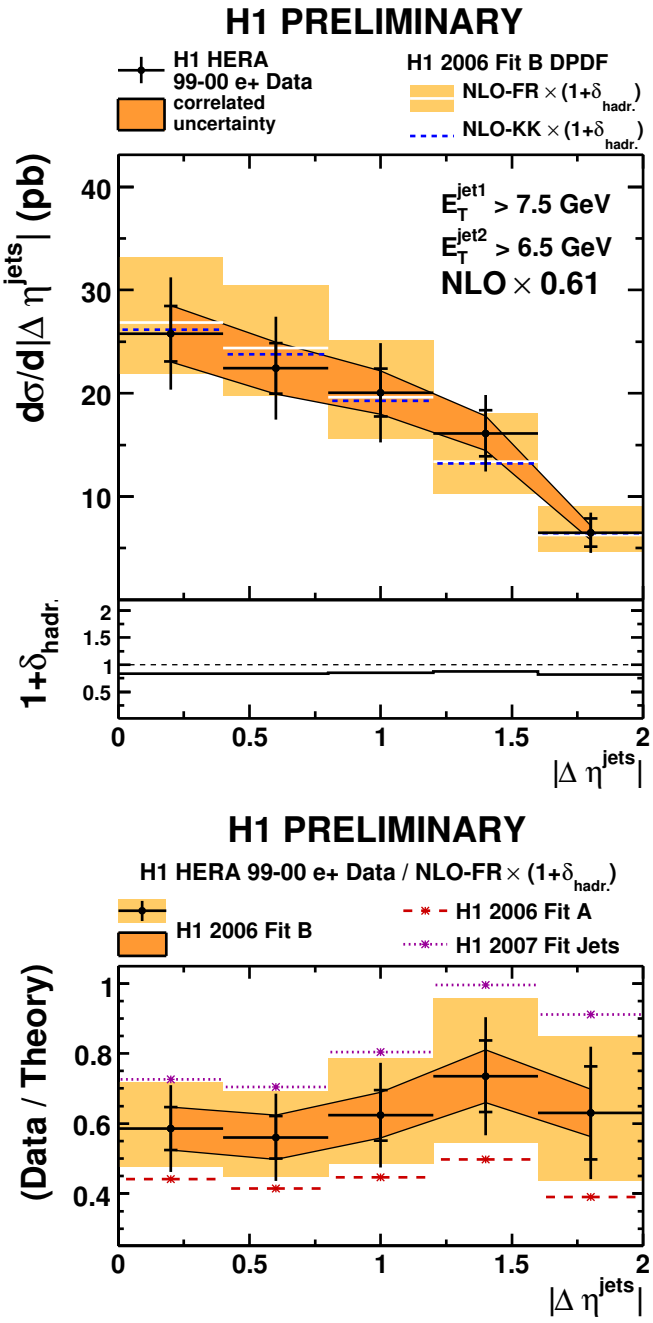

Figure 10.10: Upper plot: measurement of the differential cross section $\mathrm{d}\sigma/\mathrm{d}\,|\Delta\eta^{jets}|$. The points show the data, the inner error bars on the points are statistical and the outer error bars show statistical and uncorrelated uncertainties added in quadrature. The correlated systematic errors are indicated by the dark band. The data are compared with predictions based on the H1 2006 Fit B DPDFs, scaled by a constant factor of 0.61, obtained using the FR (white line) and KK (dashed line) calculations. Both predictions are corrected for hadronization effects using the factor $(1 + \delta_{hadr})$ shown below the main figure. The effect on the FR calculation of varying μ_r by factors of 0.5 and 2.0 is shown in the light band. Lower plot: ratio of the measured differential cross section to the FR calculation based on the H1 2006 Fit B DPDF set and corrected for hadronization effects. The experimental and theory scale uncertainties are indicated as for the cross section plot. Also indicated are the central values obtained when the H1 2006 Fit A or H1 2007 Fit Jets DPDFs are used in place of H1 2006 Fit B.

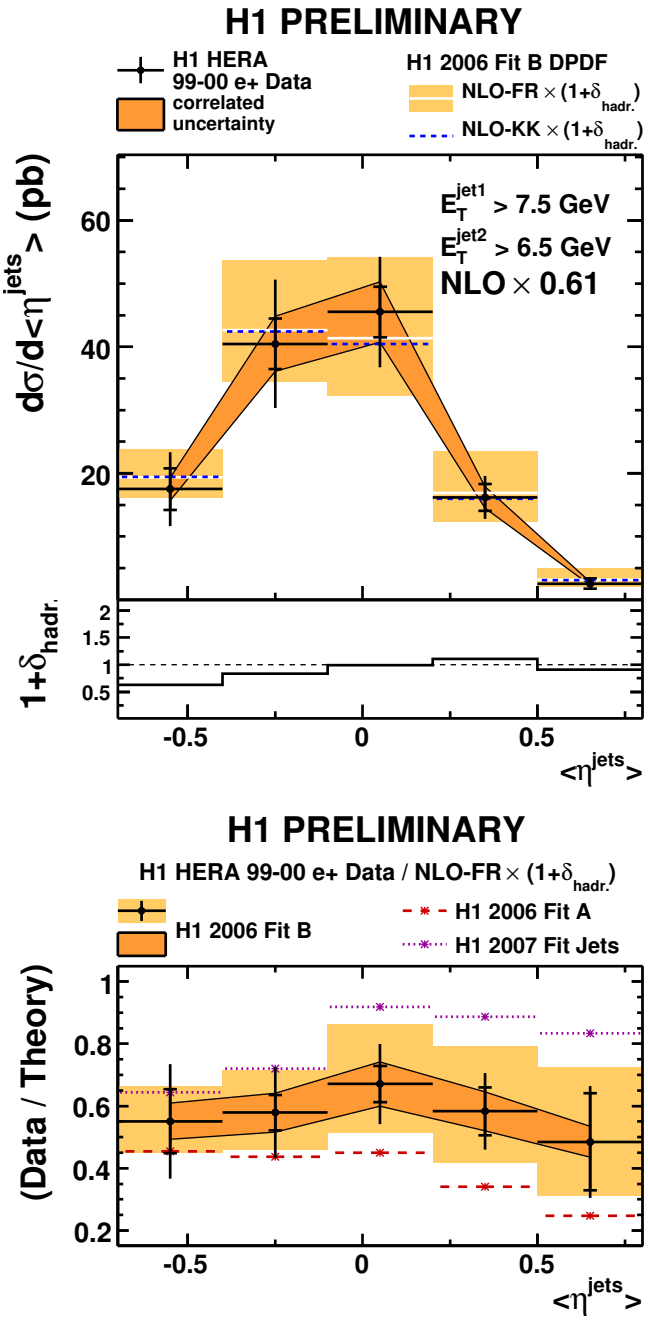

Figure 10.11: Upper plot: measurement of the differential cross section $\mathrm{d}\sigma/\mathrm{d}\,\langle\Delta\eta^{jets}\rangle$. The points show the data, the inner error bars on the points are statistical and the outer error bars show statistical and uncorrelated uncertainties added in quadrature. The correlated systematic errors are indicated by the dark band. The data are compared with predictions based on the H1 2006 Fit B DPDFs, scaled by a constant factor of 0.61, obtained using the FR (white line) and KK (dashed line) calculations. Both predictions are corrected for hadronization effects using the factor $(1 + \delta_{hadr})$ shown below the main figure. The effect on the FR calculation of varying μ_r by factors of 0.5 and 2.0 is shown in the light band. Lower plot: ratio of the measured differential cross section to the FR calculation based on the H1 2006 Fit B DPDF set and corrected for hadronization effects. The experimental and theory scale uncertainties are indicated as for the cross section plot. Also indicated are the central values obtained when the H1 2006 Fit A or H1 2007 Fit Jets DPDFs are used in place of H1 2006 Fit B.

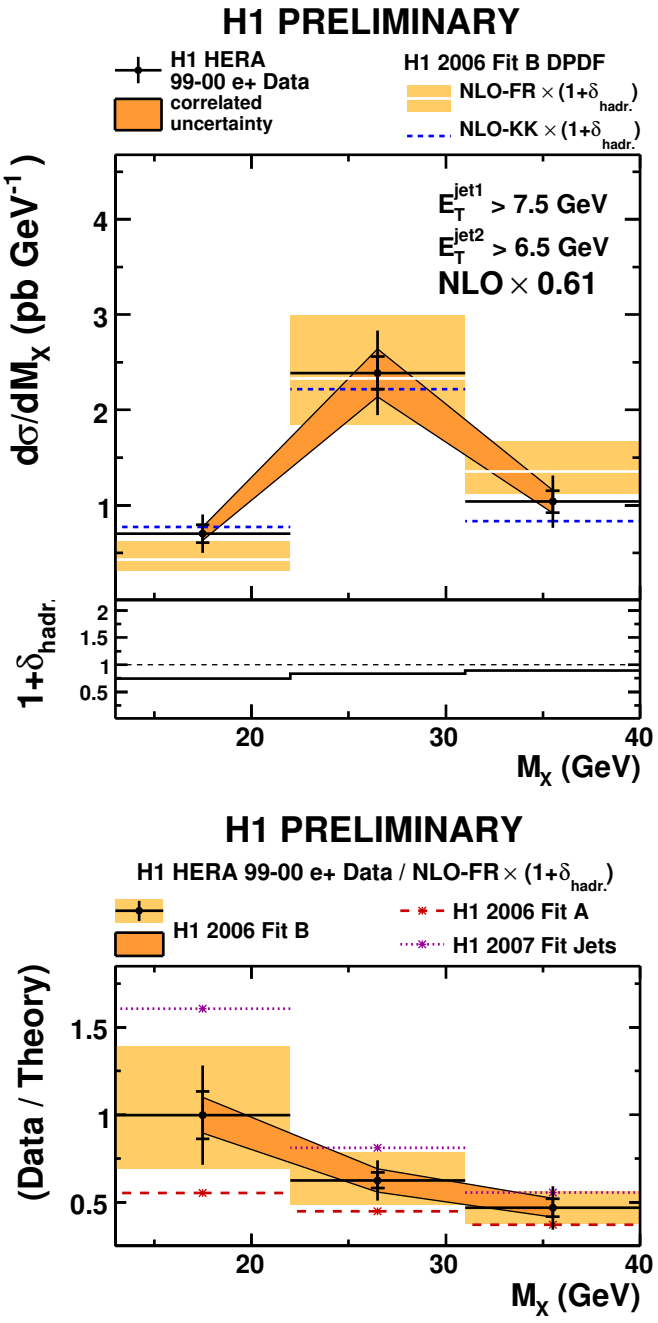

Figure 10.12: Upper plot: measurement of the differential cross section $\mathrm{d}\sigma/\mathrm{d}M_X$. The points show the data, the inner error bars on the points are statistical and the outer error bars show statistical and uncorrelated uncertainties added in quadrature. The correlated systematic errors are indicated by the dark band. The data are compared with predictions based on the H1 2006 Fit B DPDFs, scaled by a constant factor of 0.61, obtained using the FR (white line) and KK (dashed line) calculations. Both predictions are corrected for hadronization effects using the factor $(1+\delta_{hadr})$ shown below the main figure. The effect on the FR calculation of varying μ_r by factors of 0.5 and 2.0 is shown in the light band. Lower plot: ratio of the measured differential cross section to the FR calculation based on the H1 2006 Fit B DPDF set and corrected for hadronization effects. The experimental and theory scale uncertainties are indicated as for the cross section plot. Also indicated are the central values obtained when the H1 2006 Fit A or H1 2007 Fit Jets DPDFs are used in place of H1 2006 Fit B.

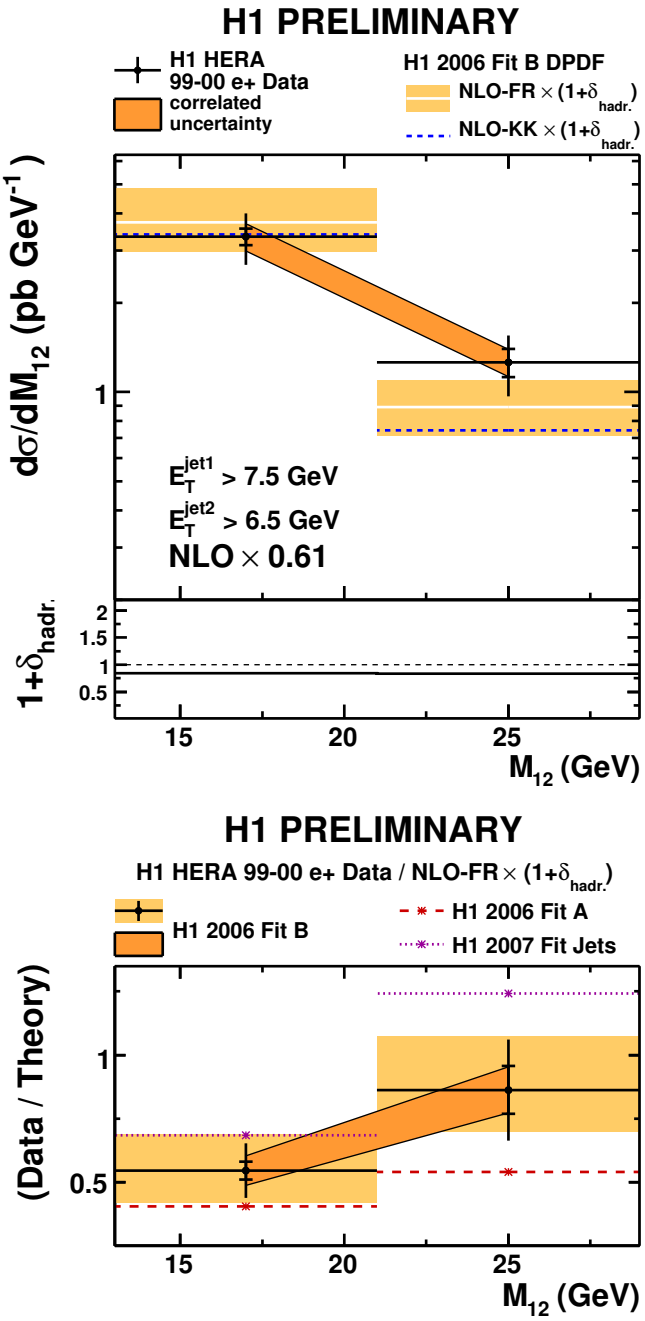

Figure 10.13: Upper plot: measurement of the differential cross section $\mathrm{d}\sigma/\mathrm{d}M_{12}$. The points show the data, the inner error bars on the points are statistical and the outer error bars show statistical and uncorrelated uncertainties added in quadrature. The correlated systematic errors are indicated by the dark band. The data are compared with predictions based on the H1 2006 Fit B DPDFs, scaled by a constant factor of 0.61, obtained using the FR (white line) and KK (dashed line) calculations. Both predictions are corrected for hadronization effects using the factor $(1+\delta_{hadr})$ shown below the main figure. The effect on the FR calculation of varying μ_r by factors of 0.5 and 2.0 is shown in the light band. Lower plot: ratio of the measured differential cross section to the FR calculation based on the H1 2006 Fit B DPDF set and corrected for hadronization effects. The experimental and theory scale uncertainties are indicated as for the cross section plot. Also indicated are the central values obtained when the H1 2006 Fit A or H1 2007 Fit Jets DPDFs are used in place of H1 2006 Fit B.

Chapter 11

Summary and Conclusions

A neural network method was proposed and developed for reconstruction of the proton momentum form the measured impact coordinates and slopes in the VFPS detector. Reasonable resolution of the method was achieved. Also a quality criterion was developed which can be used for background suppression in the VFPS. The work is summarized in [26].

Differential cross sections were measured for diffractive dijet photoproduction in two phase space regions with H1 data which differ mainly in the transverse energy range required on the jets. The results were presented in [41]. The measured cross sections were corrected for the influence of the detector effects by means of the Monte Carlo simulations. The corrected cross sections were compared with next-to-leading order QCD predictions using two independent NLO programs; FR [32] and KK [33]. The NLO QCD predictions are based on three sets of diffractive parton distribution functions measured by the H1 collaboration in [14, 15].

The main observations from analyses in both kinematical ranges are following

1. In both analyses (with lower and higher E_T range of the jets) the NLO calculations (FR and KK) based on the DPDF sets H1 2006 Fit A and B and H1 2007 Jets overestimate the data.

2. A global suppression factor of $0.54 \pm 0.01(\text{stat.}) \pm 0.10(\text{syst.})^{+0.14}_{-0.13}$ (scale.) is measured in the analysis with lower E_T range of the jets using FR NLO Fit B calculation. In the analysis with the higher E_T range of the jets a weaker suppression factor of $0.61 \pm 0.03(\text{stat.}) \pm 0.13(\text{syst.})^{+0.16}_{-0.14}$ (scale.) is measured for the FR NLO calculation based on Fit B.

3. NLO calculations obtained by means of FR program are consistent with KK calculations.

4. In general, Fit B provides the best description of shapes of the differential cross sections in both analyses.

5. Although it was predicted that the cross section of the resolved processes should be suppressed more than the direct processes, the lack of any significant x_γ dependence of the data/theory ratio is observed in both kinematical ranges. This observation is, nevertheless, consistent with the previous results in [3, 18].

6. In the analysis in the lower E_T range of the jets there is a suggestion of a dependence of the suppression factor on the E_T^{jet1}. It is observed that in the region of $E_T^{jet1} < 7$ GeV the suppression is consistent with previous H1 measurement [3], i.e. factor of ~ 0.5. Within the errors a weakening suppression is suggested for the range of $E_T^{jet1} > 7$ GeV which leads to factors which are consistent with the previous result of the ZEUS collaboration [18], i.e. 0.6 to 0.9. This observation is supported by the weaker global suppression factor measured in the analysis with jets of higher E_T, cf. point 2.

7. A large sensitivity of the results to the diffractive parton distribution functions is observed in all variables through comparisons with the H1 2006 Fit A and H1 2007 Fit Jets DPDFs in both analyses. The sensitivity is dominantly driven by differences in the region of high values of $z_{I\!P}$.

The results presented in this thesis helped to illuminate the contradictory conclusions made by the H1 and ZEUS collaborations in [3] and [18] as to the magnitude of factorization breaking in diffractive photoproduction of dijets.

Bibliography

[1] A.Kaidalov *et al.*, Factorization breaking in diffractive dijet production, *Phys.Lett.* **B559** 235-238 (2003).

[2] T. Affolder *et al.* [CDF Collaboration], Diffractive dijets with a leading antiproton in $\bar{p}p$ collisions at $\sqrt{s} = 1800$ GeV, *Phys. Rev. Lett.* **84** 5043 (2000).

[3] A. Aktas *et al.* [H1 Collaboration], Tests of QCD factorization in the diffractive production of dijets in deep-inelastic scattering and photoproduction at HERA, *Eur.Phys.J.* **C51** 549-568 (2007).

[4] R.P. Feynman, Photon-hadron interactions, *Frontiers in Physics, Benjamin* (1972).

[5] M. Gell-Mann, *Phys. Lett.* **B8** 214 (1964); G. Zweig, *CERN preprint* 8419/TH.412.

[6] S. Eidelman,*et al.*, Review of particle physics, Particle Data Group, *Phys. Lett.* **B592** 1 (2004).

[7] G. Altarelli, G. Parisi, Asymptotic freedom in parton language, *Nucl. Phys.* **B126** 298 (1977);
V.N. Gribov, L.N. Lipatov, *Sov. J. Nucl. Phys.* 438 (1972), *Sov. J. Nucl. Phys.* 675 (1972);
Yu.L. Dokshitzer. *Sov. Phys. JETP* **46** 641 (1977).

[8] R.P. Feynman, R.D. Field, A parameterization of the properties of quark jets, *Nucl. Phys.* **136** (1977).

[9] P.D.B. Collins, An Introduction to Regge Theory and High-Energy Physics, Cambridge, England: *Cambridge University Press* (1977), ISBN 0-521-21245-6.

[10] G. Ingelman and P.E. Schlein, Jet structure in high mass diffractive scattering, *Phys. Lett.* **B152** 256 (1985).

[11] V. Barone, E. Predazzi, Monograph: High-energy particle diffraction, *Springer-Verlag Berlin Heidelberg* (2002).

[12] T. Ahmed *et al.* [H1 Collaboration], Hard Scattering in gamma-p interactions, *Phys.Lett.* **B297** 205 (1992).

[13] J. Chýla, Quarks, Partons and Quantum Chromodynamics, lecture text, available at `http://www-hep2.fzu.cz/~chyla/lectures/text.pdf`.

[14] A. Aktas *et al.* [H1 Collaboration], Measurement and QCD analysis of the diffractive deep-inelastic scattering cross section at HERA, *Eur. Phys. J.* **C48** 715-748 (2006).

[15] A. Aktas *et al.* [H1 Collaboration], Dijet cross sections and parton densities in diffractive DIS at HERA, *JHEP* 0710:042 (2007).

[16] J.C. Collins, Proof of factorization for diffractive hard scattering, *Phys.Rev.*, **D57** 3051-3056 (1998).

[17] A. Aktas *et. al* [H1 Collaboration], Diffractive open charm production in deep-inelastic scattering and photoproduction at HERA. *Eur.Phys.J.* **C50** 1-20 (2007).

[18] S. Chekanov *et al.* [ZEUS Collaboration], Diffractive photoproduction of dijets in ep collisions at HERA, (2007) submitted to *Europ. Phys. Journal C.*

[19] T. Ahmed *et. al* [H1 Collaboration], First measurement of the deep inelastic structure of proton diffraction., *Phys. Lett.* **B348** 681-696 (1995).

[20] V.A. Khoze et al., On the role of hard rescattering in exclusive diffractive Higgs production, *JHEP05* 036 (2006).

[21] L. Lönnblad, M. Sjödahl, Uncertainties on central exclusive scalar luminosities from the unintegrated gluon distributions, *JHEP05* 038 (2005).

[22] I. Abt *et al.* [H1 Collaboration], The H1 detector at HERA, *Nucl. Instrum. Methods* **A386** 310-347 (1997).

[23] T. Ahmed *et al.* [H1 Collaboration], Deep inelastic scattering events with a large rapidity gap at HERA, *Nuclear Physics B* **429** 477 (1994).

[24] [H1 Collaboration], paper submitted to the 28^{th} International Conference on High Energy Physics, ICHEP'96, Warsaw, Poland, July (1996).

[25] H1 VFPS group [H1 Collaboration], Proposal for Installation of a Very Forward Proton Spectrometer in H1 after 2000, internal H1 document H1-IN-582 (2000).

[26] K. Černý, P. Van Mechelen, E.A. De Wolf, VFPS momentum reconstruction using a neural net method, internal H1 document H1-IN-619 (2005).

[27] H. Jung, Hard diffractive scattering in high-energy collisions and the Monte Carlo generator RAPGAP, *Comp. Phys. Comm.* **86** 147 (1995).

[28] M. Glück, E. Reya and A. Vogt, Parton structure of the photon beyond the leading order, *Phys. Rev.* **D 45** 3986 (1992);
M. Glück, E. Reya and A. Vogt, Photonic parton distributions, *Phys. Rev.* **D 46** 1973 (1992).

[29] T. Sjöstrand, *Comp. Phys. Comm.* **82** 74 (1994);
T. Sjöstrand, High energy physics event generation with PYTHIA 5.7 and JETSET 7.4, *CERN TH/7111-93* (1993, rev. 1994).

[30] H.L. Lai *et al.* [CTEQ Collaboration], Global QCD analysis of parton structure of the nucleon: CTEQ5 parton distributions, *Eur.Phys.J.* **C12** 375-392 (2000).

[31] B. List, A. Mastroberardino, "DIFFVM: A Monte Carlo generator for diffractive processes in *ep* scattering" in A. Doyle *et al.* (eds.), Proceedings of the Workshop on Monte Carlo Generators for HERA Physics, DESY-PROC-1992-02 396 (1999).

[32] S.Frixione, Z.Kunzst and A.Signer, Three-jet cross sections to next-to-leading order, Nucl. Phys. **B467** (1996) 399 [hep-ph/9512328];
S.Frixione, Jet photoproduction at HERA, *Nucl. Phys.* **B507** (1997) 295 [hep-ph/9706545];
see also `http://www.ge.infn.it/~ridolfi/`.

[33] M. Klasen and G. Kramer, Factorization breaking in diffractive dijet photoproduction, *Eur. Phys. J.* **C38** 93 (2004).

[34] M. Peez, B. Portheault, E. Sauvan, Energy Flow Algorithm for Hadronic Reconstruction In OO: Hadroo2, *internal H1 document* H1-IN-616 (2005).

[35] S.Catani, Yu.L. Dokshitzer, B.R. Webber, The k_T-clustering algorithm for jets in deep inelastic scattering and hadron collisions, *Phys. Lett.* **B285** 291 (1992).

[36] S. D. Ellis and D. E. Soper, Successive combination jet algorithm for hadron collisions, *Phys. Rev.* **D48** 3160-3166 (1993).

[37] X. Janssen, Electroproduction diffractive de mésons ρ à HERA, *Universite Libre de Bruxelles*, Dissertation DESY-THESIS-2003-004.

[38] J. M. Butterworth, J. R. Forshaw, M. H. Seymour, Multiparton Interactions in Photoproduction at HERA, *Z.Phys.*, **C72** 637-646 (1996).

[39] P. Thompson, Open Charm Production in Inclusive and Diffractive Deep-Inelastic Scattering, *University Birmingham*, Dissertation, (1999).

[40] S. Schenk, Energy Flow in Hard Diffractive Deep-Inelastic Scattering and Photoproduction with a Leading Proton, *University of Heidelberg*, Diploma thesis, (2003).

[41] K. Černý on behalf of the H1 Collaboration, Dijets in Diffractive Photoproduction, preliminary H1 result presented at the 16^{th} International Workshop on Deep-Inelastic Scattering and Related Subjects, DIS 2008, London, April (2008), document accesible also at: `http://www-h1.desy.de/psfiles/confpap/DIS2008/H1prelim-08-012.ps`.